# Realization of a Low-NOx Combustion System using a Small Cylindrical Furnace

**January, 2014**

## DOCTOR OF ENGINEERING

**KAPURUGE DON KUNKUMA AMILA SOMARATHNE**

**TOYOHASHI UNIVERSITY OF TECHNOLOGY**

# TABLE OF CONTENTS

# LIST OF FIGURES

# LIST OF TABLES

# ACKNOWLEDGMENTS

I have so enjoyed and profited from my studies at the Environmental and Energy Conversion Engineering Laboratory of Toyohashi University of Technology, Japan. For that, I am, above all, indebted to my supervisor, Prof. Susumu Noda, whose guidance has shaped both my life and career for the better. His encouragement, wide-knowledge, and enormous support were paved the way to fulfill this goal. In addition, I would like to express my sincere gratitude to my co-supervisors of Prof. Kenzo Kitamura and Prof. Akiyoshi Iida.

All these works would not have been possible without the massive support of contemporary and past academic staff members of the laboratory. I am deeply grateful to Prof. Yuzuru Nada, Prof. Takahiro Ito, and Prof. Tsuneyoshi Matsuoka for their valuable support on computer programming and constructive comments, and they made a wonderful environment in the laboratory for the depth research works. At the same time I wish to express my sincere thanks to all professors who conducted the lessons in my doctoral studies. The lessons gave essential theoretical backgrounds on this study.

I warmly thank all current and past colleagues of the laboratory for their immense support to my works during the last three years.

I owe my loving thanks to my wife Asangi. She has lost a lot because of my research activities even in late nights and weekends. Without her encouragement and understanding it would have been impossible for me to complete this work. Finally I wish to thank my dearest mother, father, mother-in-law, sister, brother, and brother-in-law for all they have done for me.

# ABSTRACT

The control of nitrogen oxides (NOx) is currently a major issue in designing an effective combustion system because NOx has several detrimental effects on the environment and human health. Non-premixed combustion, which is used in numerous industrial applications, is suffered from a major problem on the control of the NOx emission. Because the chemical reaction proceeds at the stoichiometric condition, the flame temperature may exceed 1800 K, at which the thermal NOx reaction is activated. Therefore, several combustion techniques have been proposed to reduce the NOx emission. Mild (moderate or intense low-oxygen dilution), or called as flameless, or high temperature air, combustion has currently attracted a lot of attention because of its unique ability to increase the thermal efficiency, and simultaneously achieve ultra-low NOx emission. These features make mild combustion an exceptional combustion technique because most of other NOx reduction methods reduce the thermal efficiency. The main practical approach in this technique is the entrainment of the burnt gases into the combustion reactants. The entrained bunt gases dilute the reactants and decrease the flame temperature, because the burnt and inert gases, such as $CO_2$, $H_2O$, and $N_2$, increase the heat capacity of combustion mixture, and thereby, decrease NOx emission. To achieve an efficient NOx control, in the mild combustion of industrial furnaces, an intense dilution of reactants is generally required. In such a case, flame instabilities, such as flame extinction or flame blow-out, may often happen because of low availability of oxidizer or fuel. Such instabilities are mainly avoided by supplying much enthalpy externally, and consequently, the auto-ignition temperature is reached via internal recirculation of burnt gases. Among several mild combustion configurations in previous studies, two of them seem to be widely used. The first method is characterized by a central jet of fuel, and a number of air jets, which are located circumferentially around the central fuel jet, supplying the preheated combustion air. In this configuration, the air jets entrain large quantities of the recirculated burnt gases, before mixing with the fuel jet. However, the starting procedure of this burner configuration has become much complex. To achieve the flameless combustion mode, initially, turbulent premixed flames are used through the air-jet nozzles, and then, the furnace is heated up, and consequently, it makes the preheated-combustion air to maintain stable turbulent non-premixed flameless combustion. In the second method, the combustion air is provided by a central high-momentum air jet, and that is surrounded by a number of low-momentum fuel jets. These weak fuel jets are injected into recirculated burnt gases, and consequently, the fuel is

diluted before it mixes with the combustion air. However, in this configuration, overall furnace efficiency may go down because fuel jets are not surrounded by air-streams, and hence, un-burnt fuel particles may be contained in the exhaust gases. Depending on the position of air and fuel injectors, different dilution cases, in which the burnt gases entrain into fuel, air or both streams, can be considered. Moreover, in these cases, dilution and preheating processes are coupled together, and their values depend on the amount of entrained burnt gases. Therefore, the designing of a simple burner configuration, which can achieve a low-NOx combustion system, is still increasingly important objective.

In the meantime, a comprehensive experimental investigation of EINOx characteristics, which gives NOx emission in terms of the emission index, of turbulent non-premixed flames in Pyrex-glass cylindrical furnaces was conducted by Noda et al., and showed that the EINOx significantly decreases by the increasing in the inner diameter of the furnace ($D$), air inlet velocity difference, ($\Delta U_a$), and global equivalence ratio, ($\phi$). The decrease in the EINOx is possibly related to the dilution of combustion mixture by burnt gases and flame stretch. The EINOx of confined non-premixed flame was scaled by the parameter $DU_F \Delta U_a$, which is proportional to $Re_{,c} Da^{-1}$, and the increase in the parameter, $DU_F \Delta U_a$, leads to linear reduction of EINOx. Here, $U_F$ is the fuel velocity, $Re_{,c}$ is the furnace Reynolds number, which reflects the turbulence in the furnace, and $Da$ is the Damkohler number, which represents the flame stretch through the air velocity difference. Moreover, flame photographs show that, in the case of larger cylindrical furnace, higher global equivalence ratio, and larger air velocity difference, the flame completely transfers to the flameless stage, and these observations provide the evidence that the increase in above three factors leads to the low-NOx combustion system.

In addition to the Pyrex glass wall furnaces, stainless steel cylindrical furnaces were also used to evaluate the effect of radiation on NOx emission under the same experimental conditions of Pyrex glass furnaces. In this study, it is found that the radiation effect on $EINO_X$ is small and almost constant with respect to above three parameters.

In confined jet flames, an inadequate supply of surrounding fluids induces the formation of the recirculation structure between the jet and furnace wall. Unlike open flames, confined jet flows undergo the entrainment of recirculated fluid at jet boundaries. The recirculation transports high-

temperature burnt gases upstream, and induces a mixing process that is related to flame stabilization and dilution. Consequently, a small cylindrical furnace, which is proposed to place in a large industrial furnace room, paves the way to combine the dilution and pre-heating phenomena because of the self-recirculation characteristics. Therefore, the enhancement of the self-dilution in confined flames should lead to the peak temperature reduction in the furnace, and thereby, considerable NOx abatement.

Hence, this study makes a numerical evaluation to characterize the effect of self-dilution in confined flames, in terms of the furnace geometry, the global equivalence ratio, and the air velocity difference, on NOx emission properties. In this study, the flow calculation software OpenFOAM, which is a high-fidelity open source code, is employed as a finite-volume solver for Reynolds-Averaged Navier Stokes (RANS) equations on an unstructured mesh of cylindrical coordinate system. The RANS equations include the conservation of mass of species, momentum, and sensible enthalpy. Either $k$-$\varepsilon$ or $k$-$\omega$ SST (shear stress transport) model was used to model the turbulence flux terms in the RANS equations. The turbulent-chemistry interaction was accounted with a partially-stirred-reactor (PaSR) turbulent combustion model. This study considers an augmented reduced kinetic mechanism for propane-air combustion, which includes 28-species and 69-elementary steps, because the dilution of reactants with recirculation fluids slows down the chemistry; thereby fast chemistry assumption is no longer valid. However, the use of detailed chemistry model has become a burden in terms of computational cost. An *in-situ* adaptive tabulation (ISAT) algorithm library is used to calculate the composition change through the chemical reaction, and thereby to reduce the computational burden.

There have been several studies on NOx formation. In hydrocarbon flames, thermal and prompt mechanisms are the main routes for NOx formation. Previous studies showed that when the peak temperature is reduced, nitric-oxide production is minimized, and then the prompt mechanism becomes the dominant route for the formation of NOx. In addition, a study illustrated that NOx reburning chemistry is significant in flames, and the neglect of the prompt and reburning NOx chemistries leads to the under-prediction of NOx emission for short-residence time and over-prediction for long- residence time, respectively. Another study demonstrated that the prompt and thermal mechanisms are strongly coupled, and the decoupled mechanisms considerably over-predict the thermal NO and under-predicts the prompt NO. Therefore, this study employs the

detailed NOx formation mechanism, which is extracted from GRI 2.11, with the propane-air reduced mechanism.

In this study, the total flame dilution quantitatively evaluated through the integration of local dilution factors along the axial direction. The local dilution factor is defined as the burnt and inert gases mass quantity entrained into the flame at each axial cross section with respect to total jet zone mass flow rate. The study found that the increase in inner diameter increases the flame dilution, and the enhancement of the self-dilution in confined combustion system lead to the peak temperature reduction in the flame, and thereby considerable thermal NOx-abatement. The EINOx characteristics of confined flames show the liner reduction with the increase in flame self-dilution. Moreover, this study found that the increase in dilution ratio as a dominant parameter, which controls the characteristics of confined flames, is very important for NOx abatement.

A confined combustion system with the internal self-recirculation can be referred to as an unsteady combustion process. In a confined combustion system, two main exemplificative asymptotic conditions can be considered. In the first case; air, which issued from the annular nozzles, starts to mix with the high-temperature burnt gas, including residual oxygen, which is transported upstream in the furnace, and this yields hot diluted oxidant, which mixes and reacts with the fuel issued from the central nozzle at the room temperature. In the second case; both the fuel and the air can mix with the high-temperature burnt gases, including residual oxygen, because of strong turbulence, and this yields hot diluted fuel/oxidant stream. Consequently, in confined flame, the internal recirculation should generate the variable composition fuel and air streams along the axial direction, and this should lead to the flame structure variation long the axial direction. Thus, in this study, the confined flame-structures, in terms of the axial distance, in the mixture fraction domain, are examined using a counter diffusion configuration to emphasis the effect of self-dilution on NOx abatement.

Eventually, this study heads to present a low-NOx combustion system in a small cylindrical furnace, and to provide a better alternative for the traditional mild combustion systems.

# CHAPTER 1

# INTRODUCTION

Turbulent non-premixed flames are encountered in a large number of industrial systems such as industrial furnaces, gas turbines, and combustion engines because of two main reasons [1]. First, when compared to premixed flames, non-premixed flames are simpler to design and build because perfect reactant mixing in specific proportion is not required. Second, these flames are also safer as they do not propagate, and thereby do not flash back, or auto-ignite in undesired locations. There are current concerns regarding pollutant emissions such as NOx, CO, and unburnt hydrocarbons. Hence, the above mentioned advantages become liabilities because the combustion of low emissions in non-premixed flames can be controlled to a lesser extent [2]. Because the chemical reactions proceed at the stoichiometric condition in the non-premixed flames, and thereby the flame temperature may exceed 1800 K, at which the thermal NO reactions are activated. NOx has several detrimental effects on the environment and human health, such as ground-level ozone formation, acid aerosol and acid rain formation, water quality deterioration, toxic chemical formation, and global forming. These harmful effects lead to the enforcement of firm legislations and regulations on air quality to develop low-emission combustion systems. Consequently, it is increasingly important to design highly-efficient combustion systems with minimum pollutant emissions.

## 1.1    Motivation for the dissertation

Several combustion techniques have been proposed to reduce the NOx emission, including multistage combustion [3], and mild (moderate and intense low-oxygen-dilution) combustion [4]. Among these, mild combustion has currently attracted a great deal of attention because of its unique ability to increase thermal efficiency, whereas simultaneously achieving ultra-low NOx emission. These features make mild combustion an exceptional combustion technique because most other NOx reduction methods reduce the thermal efficiency. The main practical approach in this technique is entrainment of the burnt gases into the combustion reactants mixture. The burnt gases dilute the reactants and decrease the flame temperature, because the burnt and inert gases, such as $CO_2$, $H_2O$, and $N_2$, increase the heat capacity of the combustion mixture, and thereby

decrease the NOx emission. In order to achieve an efficient NOx control, in the mild combustion of the industrial furnaces, an intense dilution of reactants is generally required. In such a case, flame instabilities, such as flame extinction or flame blow-out, may often happen because of the low availability of an oxidizer or fuel. Such instabilities are mainly avoided by supplying much enthalpy externally, and consequently, the auto-ignition temperature is reached via internal or external recirculation of burnt gases.

When considered the importance on achievement of sufficiently high levels of flame dilution using the burnt gas, in order to obtain the desired NOx reduction, the combustion chamber geometry is noticeably important. In the last two-decades, multiple studies have been made with different geometries and various burner configurations with this goal in mind. Pioneering research works were simultaneously carried out in Japan, Germany, Australia, and at the International Flame Research Foundation (IFRF), in the Netherland.
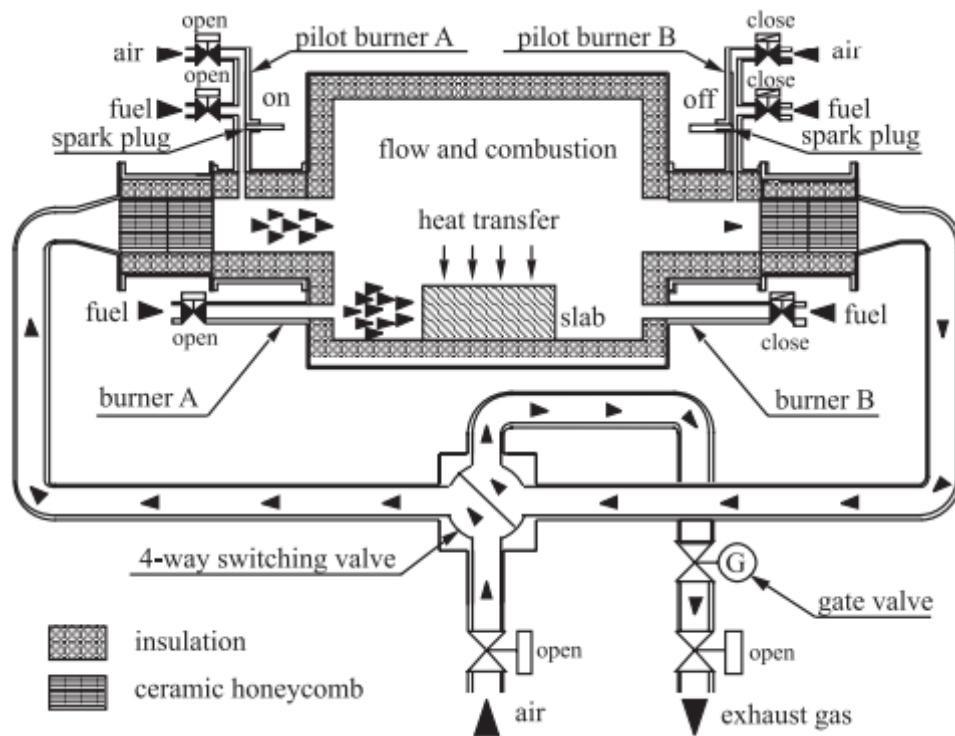


**Fig. 1.1 Schematic structure of heat recirculating furnace operated with high frequency alternating flow regenerators [4, 5]**

The Japanese design [4, 5] was distinct from the other designs such that high temperature air combustion (HiTAC), or can be referred to as a mild or flameless combustion, was carried out in a high frequency alternating flow type regenerative furnaces using highly preheated air flow, as shown in Fig. 1.1. The system consists of two-sets of a ceramic honeycomb regenerator and a burner. Since they are operated alternately every minute or so, an extremely high heat exchange coefficient is achieved by the effect of unsteady heat transfer in the honeycomb regenerator, in which the flow direction of the burnt gas and fresh air alternates against each other. The design received much attention for its accomplishment not only in energy saving, but also low NOx emission. In the study [5], the characteristics of combustion with highly preheated air were extensively studied to understand the change of combustion regime and the reason for the compatibility between high performance and low nitric oxide emission. The study found that combustion was sustained even in an extremely low concentration of oxygen, if the combustion air was preheated higher than the auto-ignition temperature of the fuel, as shown in Fig. 1.2. As an application of the principle, nitric oxide emission was reduced by the dilution of combustion air with plenty of recirculated burnt gas in the furnace, and dilution makes the oxygen content of the oxidizer low, which decreases temperature fluctuations in the flame as well as the mean temperature, and hence, achieves low nitric oxide emission.
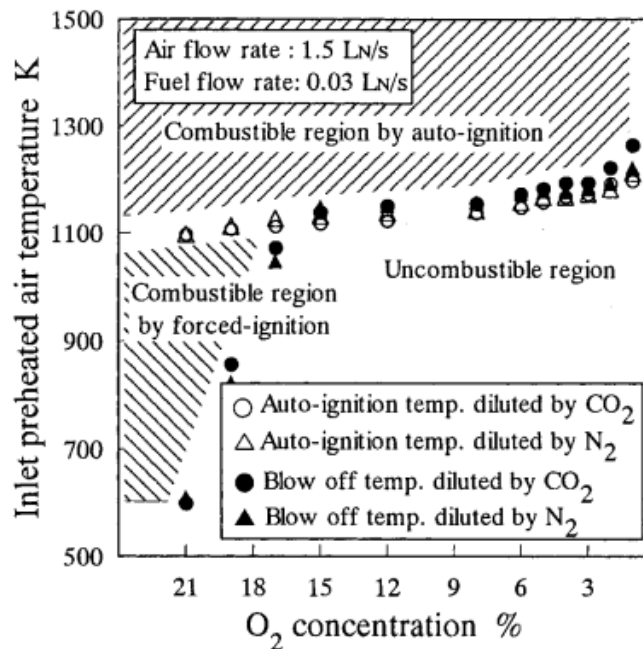


**Fig. 1.2 Auto-ignition limits and blow-off limits for natural gas in a preheated air or a diluted air with CO$_2$ or N$_2$ [5]**

3

However, major draw-back of this combustion system is its complexity. The combustion system needs large floor area for the installation and operation.

In the German path [6, 7], flameless combustion system is characterized by a central jet of fuel, and a number of air jets, which are located circumferentially around the central fuel jet, supplying the preheated combustion air. In this configuration, the air jets entrain large quantities of the recirculated burnt gases, before mixing with the fuel jet, as shown in Fig. 1.3.
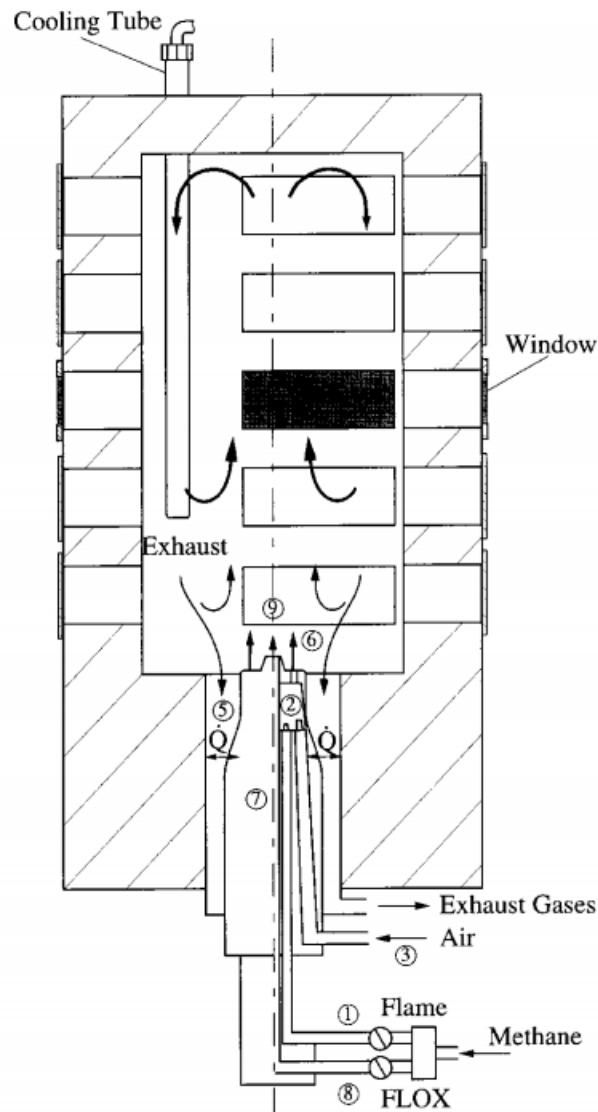


**Fig. 1.3 Principle of a burner and combustion chamber used for flameless oxidation [7]**

4

However, in this combustion system, the furnace is only able to run flameless combustion at temperature above 800 $^0$C. To heat up the combustion chamber, a starting burner is needed. During the process of heating up the furnace, fuel ①, as shown in Fig. 1.3, is led into a combustion volume within the burner ②, and mixed with air ③. The mixture is electronically ignited, and six burner-stabilized flames are formed to heat up the furnace. Because of furnace geometry, the burnt gas stream, in reversed flow, is directed outward of the furnace long the heat exchanger fins of the burner ⑤. The burnt gas heats up the air, and accelerates its flow velocity. Once the combustion chamber temperature has reached above 800 $^0$C, flameless combustion mode is possible, and the control valve ⑧ switches the fuel flow to the center nozzle ⑨. Consequently, the premixed flames, which are used as pilot flames, are extinguished, and preheated air, through the burner ②, is diluted by the recirculated burnt gas. Then, a mixture of fuel, preheated air, and burnt gas is formed, and heated up continuously by recirculating burnt gases. The reaction takes place in the downstream of the furnace. At this point, the NOx emission suddenly decreased, as shown in Fig. 1.4, owing to the flame dilution.
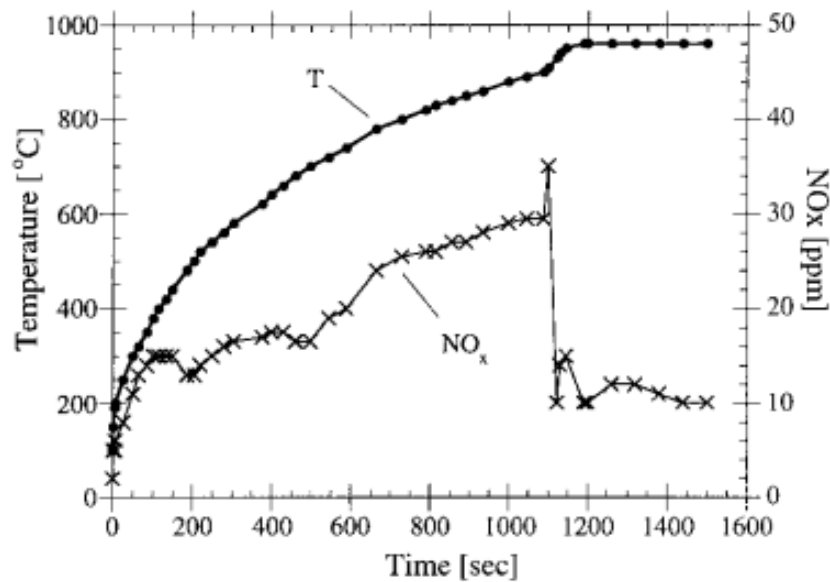


**Fig. 1.4 Starting behavior of a flameless combustion in the furnace [7]**

5
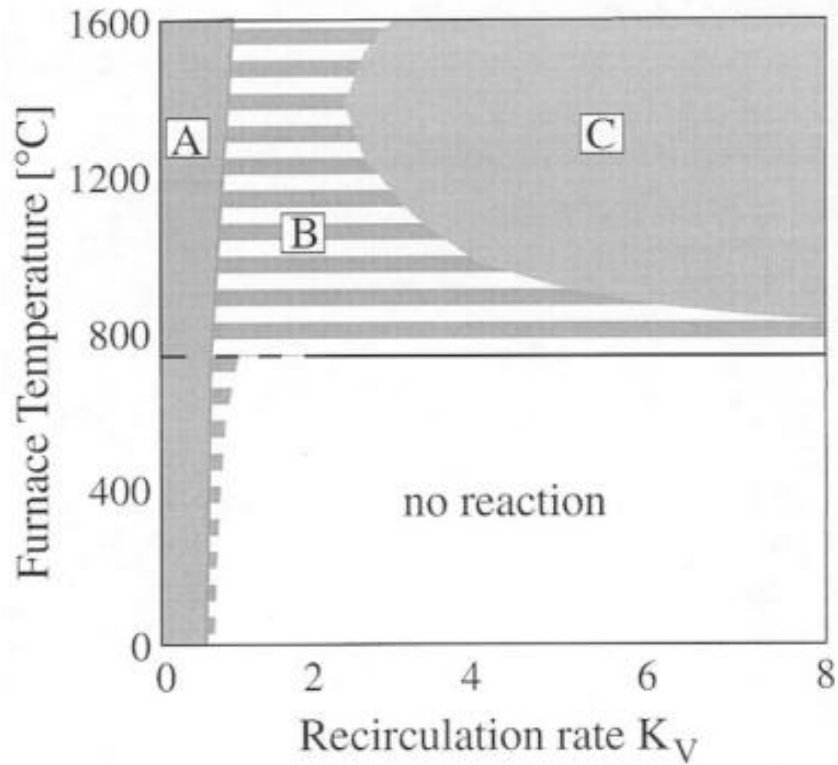
**Fig. 1.5 Definition of Stability limits of flameless combustion by means of the furnace temperature and recirculation rate [7]**

In these studies [6, 7], three combustion regimes (stable flames-A, unstable flames-B, and flameless combustion-C) were identified based on the furnace temperature and the relative recirculation rate, $K_v$, which is defined in Eq. (1.1), and the stability limits of the flameless combustion for methane and air are reported by means of the furnace temperature and $K_v$, as shown in Fig. 1.5.

$$K_v = \frac{M_r}{(M_o + M_f)} \tag{1.1}$$

Here, $M_r$ and $(M_o+M_f)$ denote the total mass flux of recirculated burnt gas and the injecting reactants (fuel and oxidant), respectively. However, the authors of [6, 7] have pointed that only the burnt gas recirculated into the combustion air/fuel stream before the reaction is considered to be recirculated burnt gas ($M_r$). Thus, the recirculation of burnt gas into the flame, which leads the flame stability and dilution, is not considered here as recirculated burnt gas. As shown in Fig. 1.5, stable flame A is possible over the whole range of combustion chamber temperature with only very low recirculation rates. For higher recirculation rates, the flame becomes unstable (the

region B in Fig. 1.5), and then lift off and finally blow-out, if furnace temperature is below the self-ignition value. However, if the furnace temperature and burnt gas recirculation rate are sufficiently high, a steady and stable form of combustion (the region C) is possible. As can be seen from the Fig. 1.5, it would be not possible to achieve the flameless stage with a cold combustion chamber. Hence, the combustion chamber must be heated up with flames, and then, switched to flameless oxidation regime.

In addition, these studies [6, 7] have showed a comparison of temperature and OH concentration between a highly turbulent premixed flame and the flameless combustion, as shown in Fig. 1.6. The upper measurements were taken from the premixed flame, whereas the bottoms belong to the flameless combustion mode. The left and right sides represent the temperature and OH radicals, respectively, by means of colored bar. It is obvious that there are no steep temperature gradients for the flameless combustion. The high temperature areas in the premixed flame front are usually the spots, in which large amount of thermal NO are formed. In the flameless combustion, high local temperature spots are almost eliminated, and its leads to the low-thermal NO formation.
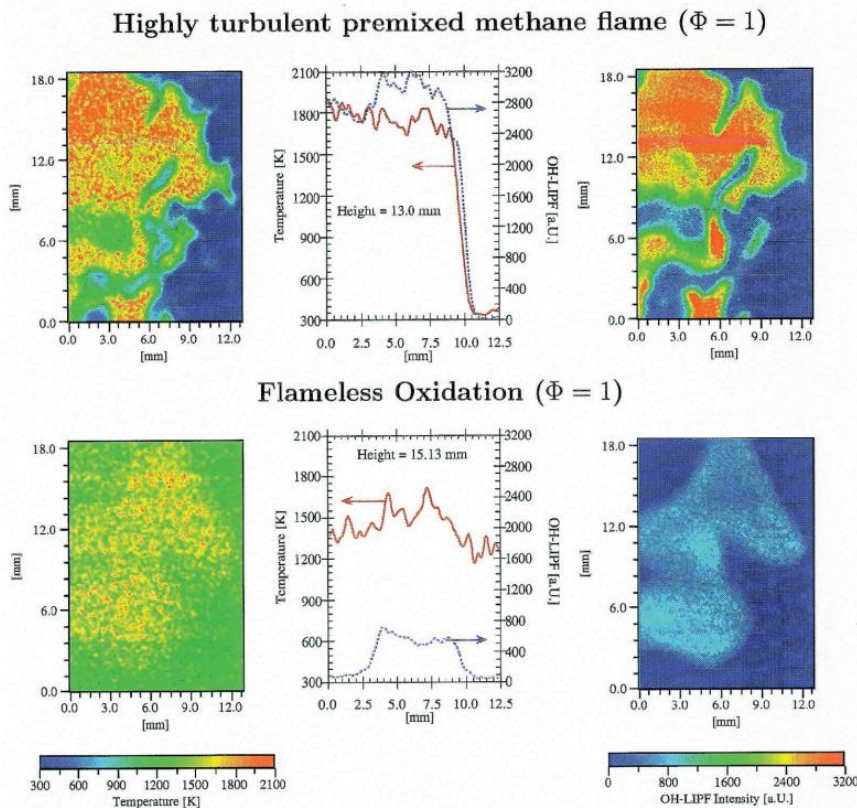


**Fig. 1.6 Comparison of simultaneously taken temperature and OH-LIPF images between premixed flames under highly turbulent condition and flameless oxidation [7]**

However, the starting procedure of this burner system has become much complex. As discussed above, to achieve the flameless combustion mode, initially, turbulent premixed flames are used through the air-jet nozzles, and then, the furnace is heated up, and consequently, it makes the pre-heated combustion air to maintain stable turbulent non-premixed mild combustion flame.

In the Australian path [8, 9], the combustion air is provided by a central high-momentum air jet, and that is surrounded by a number of low-momentum fuel jets, as shown in Fig. 1.7, and the system is called as a parallel jet burner system. In this system, weak fuel jets are injected into internal recirculated burnt gases, and consequently, the fuel is heated and diluted before it mixes with the combustion air. In this configuration, the flame stability highly depends on the momentum ratio of the fuel and air.
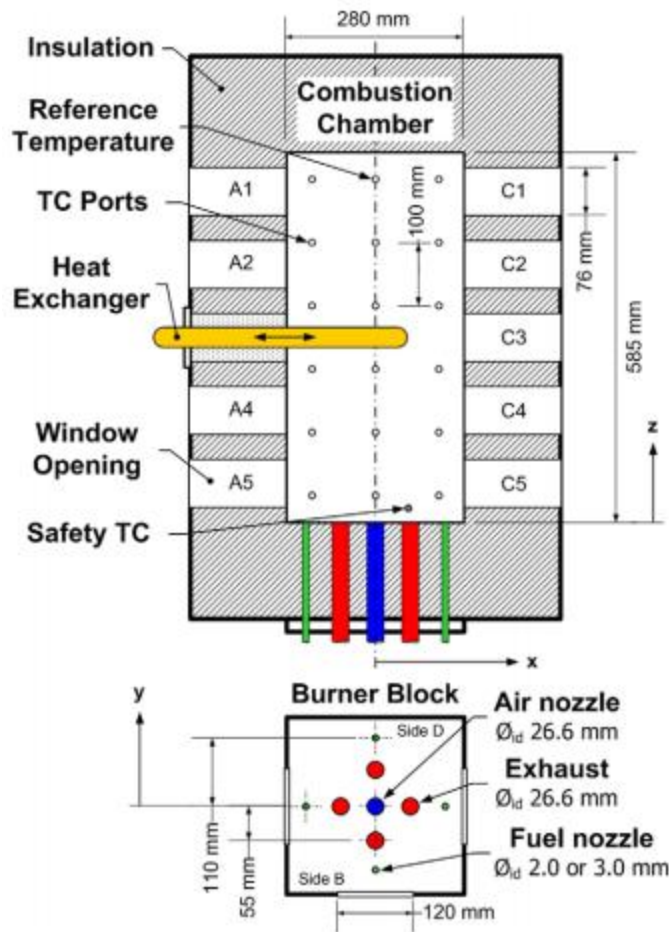


**Fig. 1.7 Schematic diagram of mild combustion furnace and parallel jet burner system [8]**

The study [8] described the performance and stability characteristics of the parallel jet mild combustion burner system in a laboratory–scale furnace, in which the reactants and burnt gas ports are all mounted on the same wall. Thermal field measurements have been presented for cases with and without combustion preheat, in addition to the global temperature and emission measurements for a range of equivalence ratio, heat extraction, air preheat, and fuel dilution levels. The burner configuration of [8] has proved to operate without the need for external air preheating, and achieved the high degree of temperature uniformity. In addition, based on an analysis of the temperature distribution and emissions, the CO formation was found to be related to the mixing patterns and furnace temperature, rather than reaction quenching by the heat exchanger. The critical equivalence ratio, or excess air level, which maintains the low CO emission, is reported for different heat exchanger positions such that critical equivalence ratio, $\phi_{critical}$ = 0.89, and an optimum operating condition is identified. Results of CO and NOx emissions, together with visual observations and simplified two-dimensional analysis of the furnace aerodynamics, demonstrate that fuel jet momentum controls the stability of this multiple jet system.

Therefore, in this configuration, overall furnace efficiency may go down at above the critical equivalence ratio because of incomplete combustion. The fuel jets, which are not surrounded by air-streams, lead to incomplete combustion at higher global equivalence ratios.

In addition to the major furnace configurations as discussed above, Dally et al. [10] reported a jet in hot co-flow (JHC) burner which consists of an insulated and cooled central fuel jet and an annulus with a secondary burner, as shown in Fig. 1.8. The secondary burner provides hot combustion products, which are mixed with air and nitrogen using two side inlets upstream of the annulus exit, to control the oxygen level in the mixture. The cold mixture of air and nitrogen also assists in cooling of the secondary burner. The study [10] reported detailed measurement of temperature and concentration of major and minor species, which have been conducted on three flames of methane and hydrogen mixture, which stabilized on the JHC burner at three different oxygen concentrations. The co-flow contained hot products at 1300 K in the immediate vicinity of the jet and the burner was mounted in a wind tunnel running air at atmospheric conditions. The data have been shown that reducing the oxygen mass fraction from 9% to 3% in the hot oxidant stream results in substantial changes to the flame structure. These changes include a peak
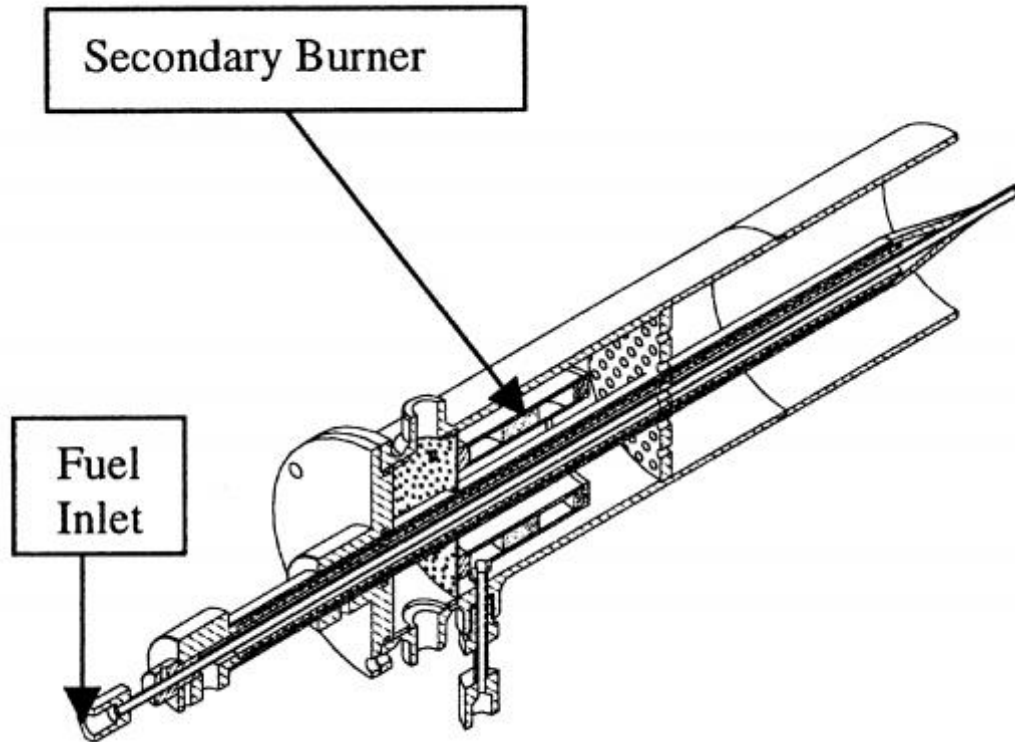
**Fig. 1.8 Cross-Section of Jet in hot co-flow burner [10]**

Temperature drops of up to 400 K, a threefold drop in OH and CO level, and significant NOx reduction.

Moreover, Oldenhof et al. reported [11, 12] on the Delft jet-in-hot co-flow (DJHC) burner which is based on Dally et al. [10]. The main difference is that Dally et al. uses addition of $N_2$ to cool down the co-flow, whereas the DJHC burner uses cooling of the co-flow through radiative and convective heat losses along the burner pipe. In this study [11], by analyzing high-speed recordings of luminescence in the visible and near UV-part of the spectrum, the lift-off behavior of flames, at which burning in a hot and diluted co-flow, was studied. Analysis of luminous image shows that, the physical mechanisms governing the lift-off process in jet-in-hot-co-flow flames and conventional lifted flames are very different. This difference is reflected in the trends for lift-off height as a function of jet Reynolds number, which are completely dissimilar. Instead of flame propagation, ignition kernel generation by auto-ignition followed by convection and growth are responsible for flame stabilization.

From the Netherlands research group, Weber et al. [13, 14] performed a series of experimental studies on the mild combustion of gaseous, liquid, and solid fuels. Their measurements were conducted inside a furnace operating with highly preheated air regime (1300 $^0$C). Their data for natural gas showed that a substantial improvement in net flux of thermal radiation can be achieved under the mild combustion. Both mixing pattern and intensity have significant effects on the overall performance of the furnace firing with natural gas, specifically, on the thermal efficiency part. The combustion process of light oil is very similar to that of natural gas, with invisible flames. However, combustion of heavy fuel oil and coal is significantly different, and the flames are always visible in their test. Weber et al. [13] pointed out that further research is still needed to optimize the burner designs for maximizing the recirculation and mixing inside the furnace. Note that their test furnace of square cross section is characterized by a burner with a central air nozzle and two small off-axis fuel injectors, and an exhaust outlet opposite to the burner inlets.

Experimental investigations of the MILD combustion, using the burner configuration of Weber et al. [13], have been performed by Rottier et al. (a France research group) [15-17].



**Fig. 1.9 The optimized burner configuration of [18]**

Kumar et.al. [18] reported a another new burner configuration with a mild combustion concept, as shown in Fig. 1.9. The principal features of configurations are (a) a burner with forward exit for burnt gas (b) injection of gaseous fuel and air as multiple, alternative, peripheral high speed jets at the bottom of the ambient temperature, thus creating high enough recirculation rates of the hot combustion products into fresh incoming reactants, and (c) use of a suitable geometric artifice- a frustum of a cone help recirculation. The system, operated at the heat release rates of 2 to 10 MW/m$^3$, shows a 10-15 dB reduction in noise in the mild combustion mode compared to a simple open burner, and NOx emission below 10 ppm for a 3 kW burner with 10% excess air. The peak temperature shows about 300 K reductions compare to a conventional burner.

Accordingly, depending on the position of air and fuel injectors, different dilution cases, in which the burnt gases entrain into fuel, air or both-streams, can be considered. Moreover in these cases, as discussed above, dilution and preheating process are coupled together, and their values depend on the amount of entrained burnt gases. Hence, the designing of a simple burner configuration, which paves the way to combine a high degree of preheating with a high degree of dilution and thereby leads to the low-NOx emission combustion system, is still increasingly important objective.

## 1.2    Objectives of the dissertation

However, the self-recirculation of burnt gases naturally takes place in a confined combustion system because of the wall confinement. In confined jet flames, an inadequate supply of surrounding fluids induces the formation of the recirculation structure between the jet and furnace wall. Unlike open flames, confined jet flows undergo the entrainment of recirculated fluid at jet boundaries. The recirculation transports high-temperature burnt gases into upstream, and induces a mixing process that is related to flame stabilization and dilution [19]. Consequently, a small cylindrical furnace, which is proposed to place in a large industrial furnace room, paves the way to combine the dilution and pre-heating phenomena because of the self-recirculation characteristics. In the meantime, a comprehensive experimental investigation of EINOx characteristics, which is defined as the ratio of the total grams of NOx produced to 1 kg of fuel burnt, of turbulent non-premixed flames in Pyrex-glass cylindrical furnaces was conducted by Noda et al.[20], and showed that the EINOx significantly decreases by the

increasing the inner diameter of the furnace ($D$), air inlet velocity difference ($\Delta U_a$), and global equivalence ratio ($\phi$).The EINOx of confined non-premixed flames was scaled by the parameter $DU_F\Delta U_a$, which is proportional to $Re_{,c}\,Da^{-1}$, and the increase in the parameter, $DU_F\Delta U_a$, leads to the linear reduction of EINOx. Here, the furnace Reynolds number $Re_{,c} = DU_F/v$, is based on the furnace inner diameter, which reflects the turbulence in the furnace, i.e. the dilution., $U_F$ and $v$ are fuel velocity and kinematic viscosity, respectively. The Damkohler number, $Da$, related to the air velocity difference; the number which is inversely proportional to the stretch rate $S = \Delta U_a/\Delta L$, where $\Delta L$ is the distance between the two air nozzles. Hence, the decrease in the EINOx, in the extensive experimental study of Noda et al. [20], is possibly related to the dilution of combustion mixture by burnt gases and flame stretch. Accordingly, the study of Noda et al., make an impressive starting point to develop a low-NOx combustion system using a small cylindrical furnace.

However, Pyrex glass makes penetration of thermal radiation in the range of wave length between 0.3 and 4.0 µm. Thus, in addition to the Pyrex glass wall furnaces, in this study, stainless steel cylindrical furnaces are used to evaluate the effect of radiation, which is predominant in the Pyrex glass wall furnaces, on NOx emission under the same experimental conditions of Pyrex glass furnaces. Consequently, EINOx characteristics are repeatedly evaluated on the parameter $DU_F\Delta U_a$ using well-insulated stainless steel furnaces.

The several physical phenomena in a confined configuration because of combustion, such as recirculation, entrainment, and dilution, can be calculated by numerical simulation on the basis of mathematical models. Thus, these models should be able to design the optimum combustion operation and predict the pollutant emission. The computational evaluation of the pollutant emission characteristics leads to the building of a scaling law for predicting the NOx emissions in the designing of industrial furnaces. Thus, in this study, confined turbulent non-premixed flames are numerically investigated, and the computational predictions of flow and scalar fields are extensively compared with experimental measurements.

Moreover, the enhancement of the self-dilution in confined flames should leads to the reduction of peak temperature in the furnace, and thereby, considerable NOx abatement. Hence, this study

directs to make a numerical evaluation to characterize the effect of self-dilution in confined flames on NOx emission properties. In this study, the total flame dilution quantitatively evaluated, and it is needed to evaluate the effect of the increase in dilution ratio, as a dominant parameter, in confined flames on NOx abatement.

A confined combustion system with the internal self-recirculation can be referred to as an unsteady combustion process. In a confined combustion system, two main exemplificative asymptotic conditions can be considered. In the first case; the air starts to mix with high-temperature burnt gases, including residual oxygen, which are transported upstream in the furnace, and this yields hot diluted oxidant, which mixes and reacts with the fuel issued at room temperature. In the second case; both the fuel and the air streams can mix with high-temperature burnt gas, including residual oxygen, because of strong turbulence, and this yields hot diluted fuel/oxidant stream. Consequently, in confined flames, the internal recirculation should generate the variable composition and temperature streams along the axial direction, and this should lead to the flame structure variation long the axial direction. Therefore, in this study, the confined flame-structures, in terms of axial distance, in the mixture fraction domain, are examined by using the counter diffusion configuration. The study desires to verify the self-dilution characteristics in confined flames using the flame structures in mixture fraction domain.

## 1.3    Outline of the dissertation

The dissertation is presented in following order. Chapter 1 describes the general motivation and objectives in this research. This chapter includes the brief summary on currently existing NOx reduction techniques, and primary requirements for a simple low-NOx combustion system. Chapter 2 describes the experimental investigation of the effect of radiation on EINOx emission in the confined flames.  As a starting point, chapter 3 illustrates the numerical evaluation methodology for confined turbulent non-premixed flames.  The numerical simulation leads to the characterization of main features of turbulent non-premixed confined flames. In addition, numerical codes are verified for the future studies. Chapter 4 discusses the self-dilution characteristics of confined flames in terms of the furnace geometry, the global equivalence ratio, and the air velocity difference. Moreover, this chapter presents the variation of the EINOx characteristics of confined flames in the flame self-dilution characteristics. Chapter 5 is used to

authenticate the self-dilution characteristics in confined flames by using the counter diffusion configuration. Chapter 6 gives concluding remarks and recommendations for future studies.

# CHAPTER 2

# EXPERIMENTAL INVESTIGATION OF THE EFFECT OF RADIATION ON EINO$_X$ IN CONFINED TURBULENT NON-PREMIXED FLAMES

## 2.1    Introduction

In several practical applications, combustion is performed in a confined configuration with gaseous fuel and oxidizer, which are introduced as jets. An important characteristic of confined jet flows is the existence of recirculation vortex. Thus, the confined combustion is strongly affected by high-temperature burnt gas, which is transported by recirculation. This leads the dilution of fuel and oxidizer, and then, dilution leads to the decrease in the maximum flame temperature. In addition, the entrainment of burnt gases into the flame leads to high efficiency combustion, through the recovery of heat. An investigation of the EINOx characteristics of confined flames, by using Pyrex glass wall furnaces, was conducted by Noda et al. [20], and showed that the EINOx significantly decreases by increasing the inner diameter of the furnace ($D$), the air inlet velocity difference ($\Delta U_a$), and the global equivalence ratio ($\phi$).The EINOx of confined non-premixed flames was scaled by the parameter $DU_F \Delta U_a$, which is proportional to $Re_{,c} \, Da^{-1}$, and the increase in the parameter, $DU_F \Delta U_a$, leads to the linear reduction of EINOx. Here, the furnace Reynolds number $Re_{,c} = DU_F / v$, is based on the furnace inner diameter, which reflects the turbulence in the furnace, i.e. the dilution., $U_F$ and $v$ are fuel velocity and kinematic viscosity, respectively. The furnace Reynolds number is an analogue to the back ward-step flows, of which flow structures are dominated by the step-height and the main flow velocity [21]. The Damkohler number, $Da$, related to the air velocity difference; the number which is inversely proportional to the stretch rate $S = \Delta U_a / \Delta L$, where $\Delta L$ is the distance between the two air nozzles. Hence, the decrease in the EINOx, in the extensive experimental study of Noda et al., is possibly related to the dilution of combustion mixture by burnt gases and flame stretch. On the other hand, Pyrex glass makes penetration of thermal radiation in the range of wave length between 0.3 and 4.0 µm. This range is a part of the wave length of thermal radiation, but the main part in terms of the emissive power. Thus, the experimental study of Noda et al [20] was carried in another

time, using the insulated stainless steel cylindrical furnaces, to evaluate the effect of radiation on EINOx characteristics in confined flames. Then, the radiation effect is deeply discussed by comparison of the flame characteristics in both furnaces.

## 2.2    Experimental apparatus

The experimental apparatus is basically the same as that reported by Noda et al [20], as shown in Fig. 2.1. Furnaces consist of cylindrical combustion chambers, either Pyrex glass or stainless steel, which are installed vertically, and a burner is installed at the center of the bottom of the combustion chamber. The stainless steel cylinders were completely covered by insulators. In addition, the stainless steel walls were used to measure laser Doppler velocity. Each of them has a pair of quartz windows of $600 \times 55$ mm$^2$, which has thickness of 2 mm, on the front and back sides. The cylindrical furnaces, having the inner diameter (i.d) of 95, 143, and 182 mm, were used to investigate the effect of the furnace geometry, and each furnace is 840 mm in height. The fuel nozzle is constructed of a stainless pipe of 2 mm i.d with a rim thickness of 0.205 mm and a pilot nozzle of 3.19 mm i.d with a rim thickness of 0.28 mm. The fuel nozzle projects 27 mm into the furnace and two air nozzles surround the fuel nozzle at the bottom of the furnace.
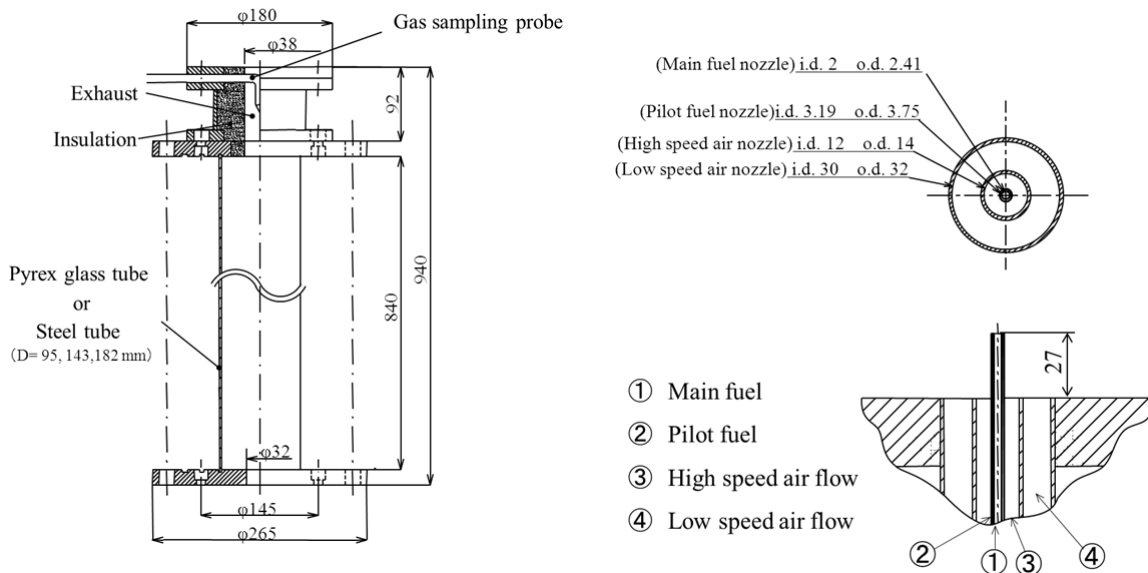


**Fig. 2.1 Schematic of experimental apparatus (left) and burner configuration (right) [20] (dimensions in mm)**

17

The inner and outer nozzles are of higher and lower air velocity, respectively. The higher-velocity nozzle is of 12 mm i.d with a rim thickness of 1 mm, and the lower-velocity nozzle is of 30 mm i.d with a rim thickness of 1 mm. The furnace exit is contrasted to 38 mm in diameter to facilitate the uniform flow and scalar fields. The coordinates $z$ and $r$ used, henceforth, are of the axial and radial directions, respectively.

## 2.3     Experimental conditions

Propane was used as the main-fuel, whereas hydrogen was used as the pilot-fuel. The volumetric ratio of the hydrogen flow rate to the total-fuel flow rate was fixed at 0.3; nonetheless the ratio of the heat-release of hydrogen flow rate to total-heat-release rate is approximately 4.8%. The air-velocity difference, $\Delta U_a$, which is based on the difference between high and low air velocities, is interpreted as the turbulent intensity at the flame boundary. The total airflow rate was fixed to 0.002 m$^3$/s, and thus, the increase in the fuel velocity, $U_F$, increases the global equivalence ratio, $\phi$. The experimental conditions are summarized in Tables 2.1 and 2.2.

**Table 2.1 Experimental conditions for fuel**

| Global equivalence ratio $\phi$ | | 0.4 | 0.6 | 0.8 | 0.9 |
|---|---|---|---|---|---|
| Propane | $U_{C3H8}$ [m/s] | 10.4 | 15.5 | 20.7 | 23.3 |
| Pilot flame (H$_2$) | $U_{H2}$ [m/s] | 4 | 6 | 8 | 9.1 |
| Reynolds number | $Re$ | 4500 | 6800 | 9100 | 10200 |

**Table 2.2 Experimental conditions for air flows**

| Total air flow rate $Q_a$ [l/min] | 120 | | | | | | | |
|---|---|---|---|---|---|---|---|---|
| Velocity difference $\Delta U_a$ [m/s] | 2 | 4 | 6 | 8 | 10 | 12 | 14 | 16 |
| High air velocity $U_H$ [m/s] | 4.7 | 6.4 | 8.1 | 9.8 | 11.5 | 13.2 | 14.9 | 16.6 |
| Low air velocity $U_L$ [m/s] | 2.7 | 2.4 | 2.1 | 1.8 | 1.5 | 1.2 | 0.9 | 0.6 |

## 2.4     Measurement methods

### 2.4.1   Laser Doppler velocimetry

Velocity measurements were implemented using a laser Doppler velocimetry (LDV) system (TSI, IFA 755) with the equipment error of 0.1%. Magnesium oxide powder of 1 μm in mean diameter was used as the particle tracker. The fluctuation of gas density refracts the laser beams to shift the

measurement point and change the measurement data. Based on Yanagi [22], in the evaluation, the velocity measurement errors were less than 2%.

### 2.4.2   Thermocouples

The temperature was measured by a Pt/Pt-13%Rh thermocouple of 0.1 mm coated with $Y_2O_3$-BeO in order to avoid catalysis. The thermocouple support, except for the measuring part, was cooled by water to protect against heat damage. Radial distributions of temperature were measured at the locations of $z = 50, 150, 250, 350, 450,$ and 550 mm from the fuel nozzle exit.

### 2.4.3   Gas analyzer

Concentration measurements were performed using a NOx-$O_2$ gas analyzer (SHIMAZU, NOA-7000) for NOx (NO and $NO_2$), and an infrared gas analyzer (SHIMAZU, CGT-7000) for CO, $CH_4$, and $O_2$. Moreover, a preprocessing unit, referred to as a gas sampling unit (SHIMAZU, CFP-8000), was used to remove particles such as water and soot. A sampling probe of 2 mm i.d was cooled by water in order to freeze the reaction and withstand the high temperatures. The sampling line between the probe and the analyzer however was heated to over $100^0$C in order to avoid condensation of $H_2O$. NOx data is discussed only for the flame condition, in which the CO concentration is lower than 300 ppm.

### 2.4.4   Digital camera

Flame photographs were taken with a digital camera (OLYMPUS, C-5050ZOOM) with an exposure of 1/5s and F2.3.

## 2.5   Results and discussion

Initially, in order to facilitate the discussion of the effect of radiation on EINOx characteristics in confined flames and of numerical investigation of the effect of self-dilution characteristics in confined flames on NOx abatement in next the chapters, the confined flame characteristics, using the experimental measurements [23], are briefly reported here from Section 2.5.1 to Section 2.5.3.

### 2.5.1 Flame appearance

Figure 2.2 shows flames in Pyrex wall furnaces with respect to the furnace inner diameter, $D$, and the global equivalence ratio, $\phi$, for the air velocity difference, $\Delta U_a$ of 8 m/s. An increase in $D$ leads to the contraction of the luminous flame region and the expansion of the blue flame region. This tendency is enhanced by the increase in $\Delta U_a$, as shown in Fig. 2.3, which shows flames in Pyrex wall furnaces with respect to the $D$ and $\Delta U_a$, for $\phi = 0.8$. In the case of $D = 182$ mm and $\phi = 0.8$, the flame completely enters the flameless stage at $\Delta U_a = 12$ m/s and 14 m/s. Moreover, the increase in the $\Delta U_a$ decreases the flame length, with a linear decrease in the luminous region and a linear increase in the blue flame region. In addition, in Fig. 2.2, in the case of $D = 95$ mm, the flame volume has been linearly increased by the increase in $\phi$. However, in $D = 182$ mm, the increase in the flame volume is not linear with respect to the increase in $\phi$, and the increase rate is decreased. Thus, the flame appearance with respect to $D$, $\phi$, and $\Delta U_a$ should be related to the entrainment of burnt gases at the flame boundaries and flame stretch.
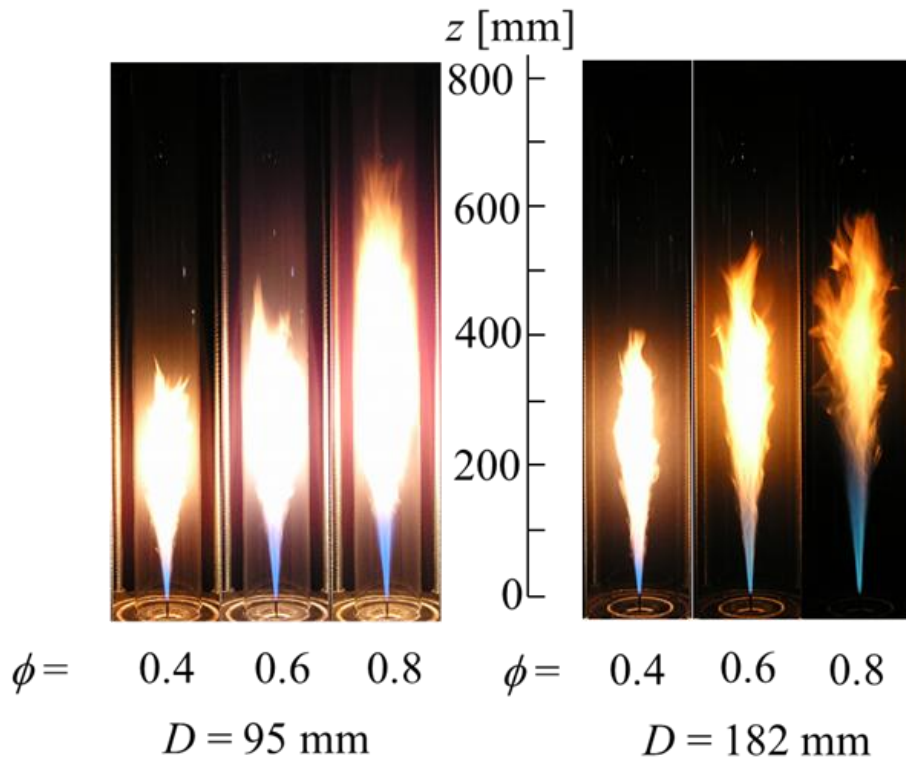


**Fig. 2.2 Flame photographs for $\Delta U_a = 8$ m/s**
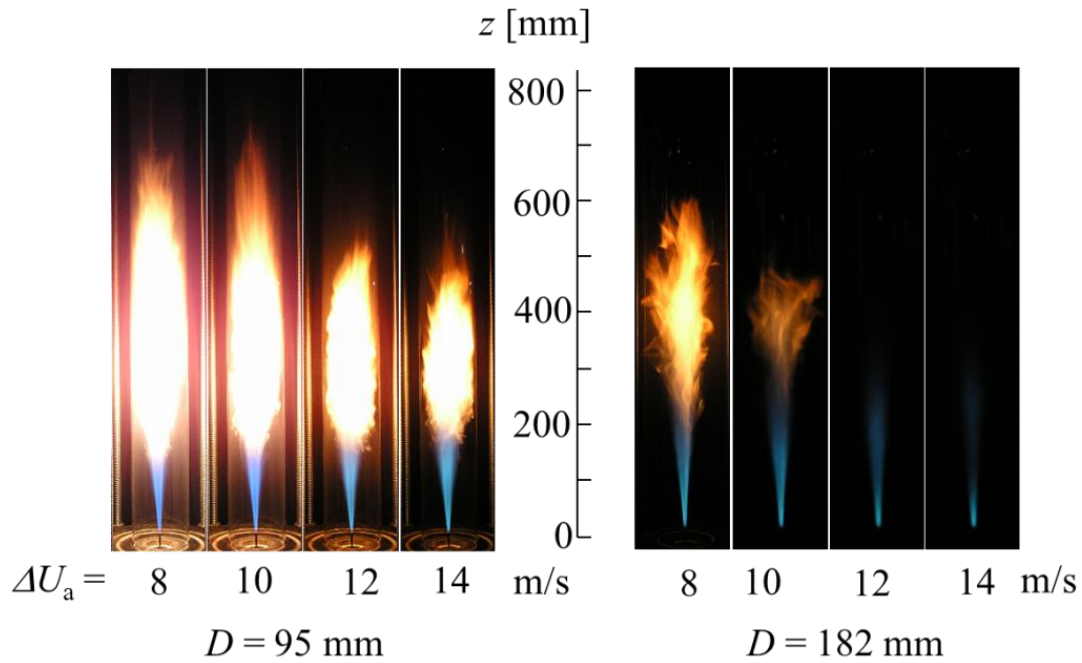
**Fig. 2.3 Flame photographs for $\phi = 0.8$**

### 2.5.2 The effect of inner diameter on temperature

The changes in the temperature with respect to the inner diameter of the furnace, $D$, for the case of $\phi = 0.8$ and $\Delta U_a = 14$ m/s in Pyrex glass wall furnaces are shown in Fig. 2.4. The temperature radial distributions at $z = 50$ mm show the maximum values in the flame region, which is identified by the blue flame in Fig. 2.3. The temperature decreases outside the high temperature region because of the cooling caused by the airflow. However, the temperature again increases outside the airflow. This is possibly caused by the transportation of the burnt gases towards the upstream region by recirculation vortex. The increase in $D$ decreases the temperature in the flame region. This is caused by the dilution through the strengthened burnt gases self-recirculation (BGR), resulting from the enlarged vortices. On the other hand, the maximum temperatures near $r = 20$ mm do not change monotonically with $D$. This is attributed to the vortex strength and the temperature of burnt gases. In the case of $D = 95$ mm, the strength of the vortex is weaker, and thus the temperature characteristics should be dominated by the cooling, which is caused by the

cold air flow. The increase in $D$ enhances the effects of BGR and increases the ambient temperature in the case of $D = 143$ mm. However, the BGR also decreases the flame temperature, and consequently, the temperature of burnt gases. This causes a decrease in the ambient maximum temperature at near $r = 20$ mm in the case of $D = 182$ mm. The temperature profiles at $z = 150$ mm and 250 mm may reflect the above flame appearances with respect to the luminosity and flame size. The temperature distributions tend toward uniform with $D$.
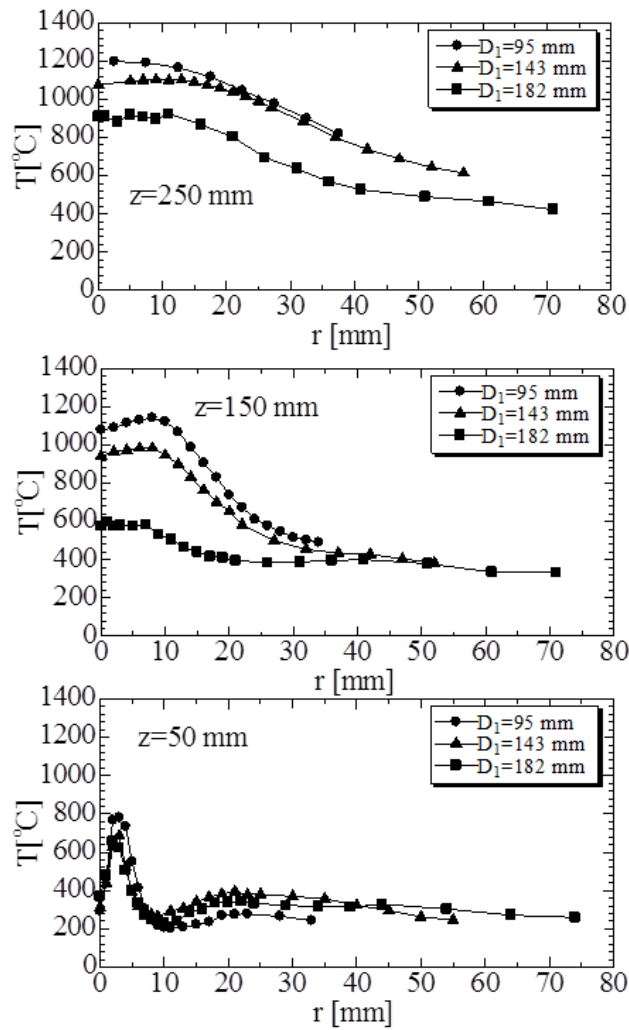


**Fig. 2.4 Radial distributions of mean temperature in terms of inner diameter, $D$, for $\phi = 0.8$ and $\Delta U a = 14$ m/s, in Pyrex glass wall furnaces.**

## 2.5.3 The effect of inner diameter on surrounding oxygen concentration

Figure 2.5 shows the radial distribution of oxygen concentration for the case of $D = 95$ mm and 182 mm, for $\phi = 0.8$ and $\Delta U_a = 14$ m/s, in Pyrex glass wall furnaces. The distributions of $O_2$ concentration at $z = 50$ mm show a saddle-shape, which is attributed to the air supplies. The increase in $D$ decreases the concentration in the flame and the ambient regions because of the dilution. Note that the concentration near the wall from $z = 50$ mm to 250 mm is maintained approximately 5 vol% for the case of $D = 182$ mm. This value is more approximate to the theoretical burnt gas volume composition for $\phi = 0.8$, such that $CO_2$ :9.7%, $H_2O$:12.6%, $N_2$:74.1%, and $O_2$:3.6%. This is an evidence of the occurrence of strong BGR in large cylindrical furnaces.
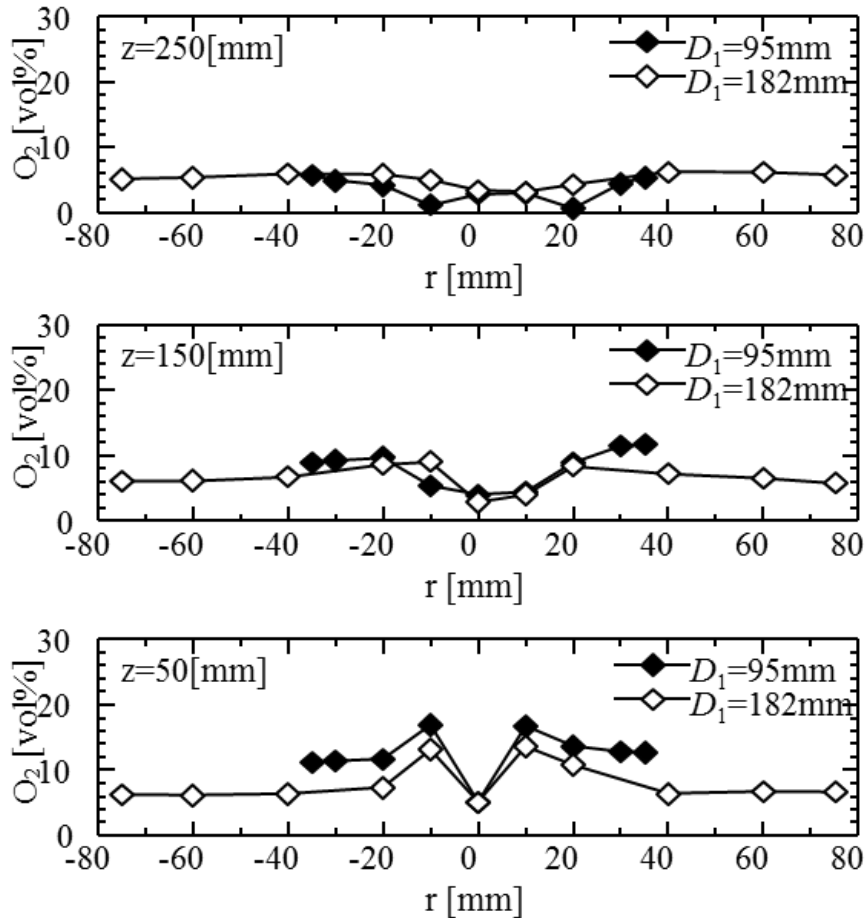


**Fig. 2.5 Radial distributions of oxygen concentration in terms of inner diameter, $D$, for $\phi = 0.8$ and $\Delta U$a = 14 m/s, in Pyrex glass wall furnaces**

## 2.5.4 The effect of radiation on EINOx characteristics
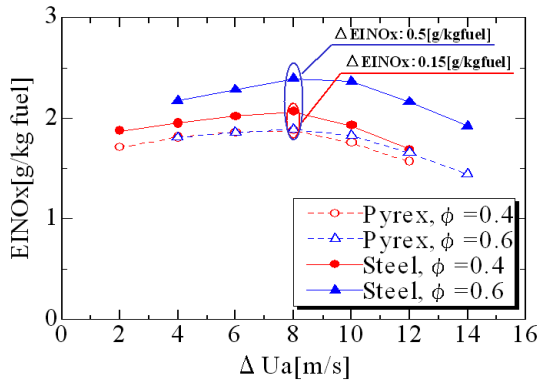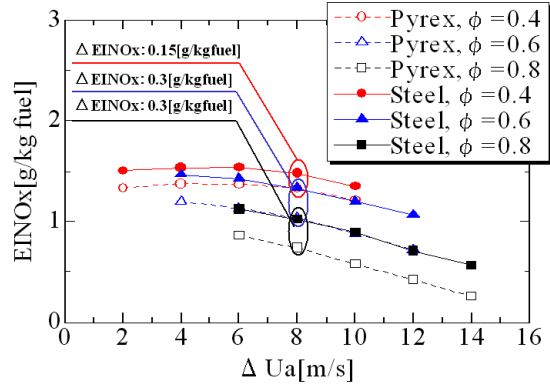


(a) $D = 95$ mm          (b) $D = 182$ mm

**Fig. 2.6 Radiation effect on EINOx**
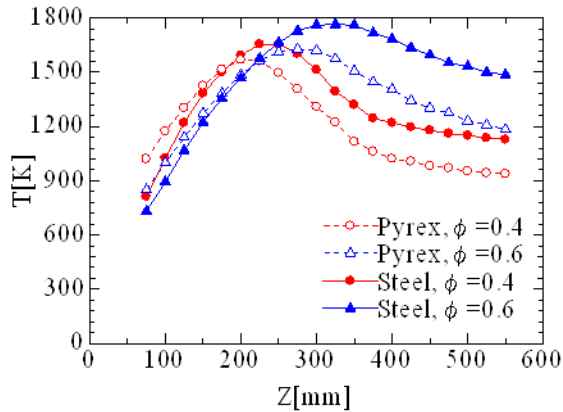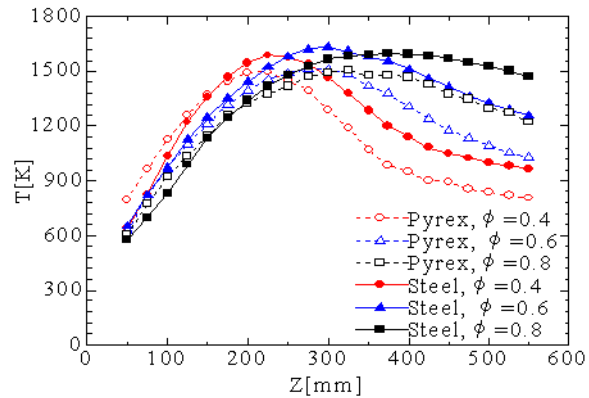


(a) $D = 95$ mm          (b) $D = 182$ mm

**Fig. 2.7 Axial mean temperature distributions for $\Delta U_a = 8$ m/s.**

Figure 2.6 shows emission indices of NOx (EINOx) in terms of the inner diameter, $D$, and the global equivalence ratio, $\phi$ for the cases of Pyrex glass wall and stainless steel wall, respectively. Figure 2.7 shows axial mean temperature distributions in Pyrex glass and stainless steel wall furnaces, in terms of $D$ and $\phi$, for $\Delta U_a = 8$ m/s, respectively. The EINOx difference for both

24

furnaces is attributed to the radiation with the consideration of the penetration wave length of Pyrex glass, as mentioned in Section 2.1. The characteristics of EINOx may be related to the flame appearances in Section 2.5.1, i.e. the EINOx is roughly proportional to the luminosity. The increase in $D$, $\Delta U_a$, and $\phi$ decreases EINOx with exceptions of $\Delta U_a$ and $\phi$ for $D = 95$ mm. The increase in $D$ should enlarge the recirculation vortices, and thereby, enhances the entrainment of burnt gases, and hence dilution. The increase in $\Delta U_a$ for the lower range, in the case of $D = 95$ mm, increases the EINOx as a result of the enhancement of the reaction through the mixing of fuel and oxidizer. However, the larger $\Delta U_a$ decreases the EINOx, and this is caused by the flame cooling associated with flame stretch and the dilution through the more enhancement of mixing. The increase in $\phi$ increases the furnace Reynolds number, $Re,c = DU_F/\nu$, under the present conditions, reflecting the turbulent intensity in the furnace as mentioned above. Thus, the increase also works for the enhancement of dilution through the recirculation of the burnt gases of lower oxygen concentration. Moreover, the increase in $\phi$ for $D = 182$ mm increases the flame volume non-linearly, and the increase rate is depressed with $\phi$, as shown in Fig. 2.2. This leads to the decrease in EINOx, which is defined as the total grams of NOx produced per 1kg of fuel burnt. Then, the above exception is elucidated with the temperature distributions in Fig. 2.7 (a). In the case of $D = 95$ mm, sizes of recirculation vortices are smaller, and thereby, the dilution effect is weaker. The volume of the flame and total heat amount become larger with $\phi$, and the maximum temperature becomes higher, as shown in Fig. 2.7 (a). This leads to the increase in EINOx. This tendency is stronger for the adiabatic case of steel wall. Thus, the radiation effect on the EINOx becomes stronger. The EINOx difference between the Pyrex and steel walls changes from approximately 0.15 g/ (kg fuel) for $\phi = 0.4$ to 0.5 for $\phi = 0.6$ in the case of $D = 95$ mm and $\Delta U_a = 8$ m/s. However, in the case of $D = 182$ mm and $\Delta U_a = 8$ m/s, the EINOx difference changes from approximately 0.15 g/ (kg fuel) for $\phi = 0.4$ to 0.3 for $\phi = 0.6$ and 0.8. The negligible differences between the $D = 95$ and 182 mm for $\phi = 0.4$ is caused by smaller volumes of the flames. The decrease in the EINOx differences for the larger $\phi$ of 0.6 and 0.8 in the case of $D = 182$ mm is also caused by the reduction of the flame volume due to the dilution as shown in Fig. 2.2. This volume reduction weakens the radiation effect. The dilution effect enhanced in $D = 182$ mm depresses maximum temperature. The increase in $\phi$ for $D = 182$ mm does not lead to an increase in maximum temperature through the entrainment of burnt gases with lower oxygen

concentration. Thereby, the radiation effect is decreased for larger $\phi$ in the case of $D = 182$ mm. Figure 2.8 shows the radiation effect on EINOx with respect to the parameter $DU_F \Delta U_a$, and the EINOx decreases linearly with the parameter, and the radiation effect is approximately constant except for small values of the parameter (as shown in a circle). Considering the reaction rate of NOx, as an exponential function of temperature, these results reflect small temperature changes in the furnace can reduce the NOx emission, even though flames are exposed to radiation.
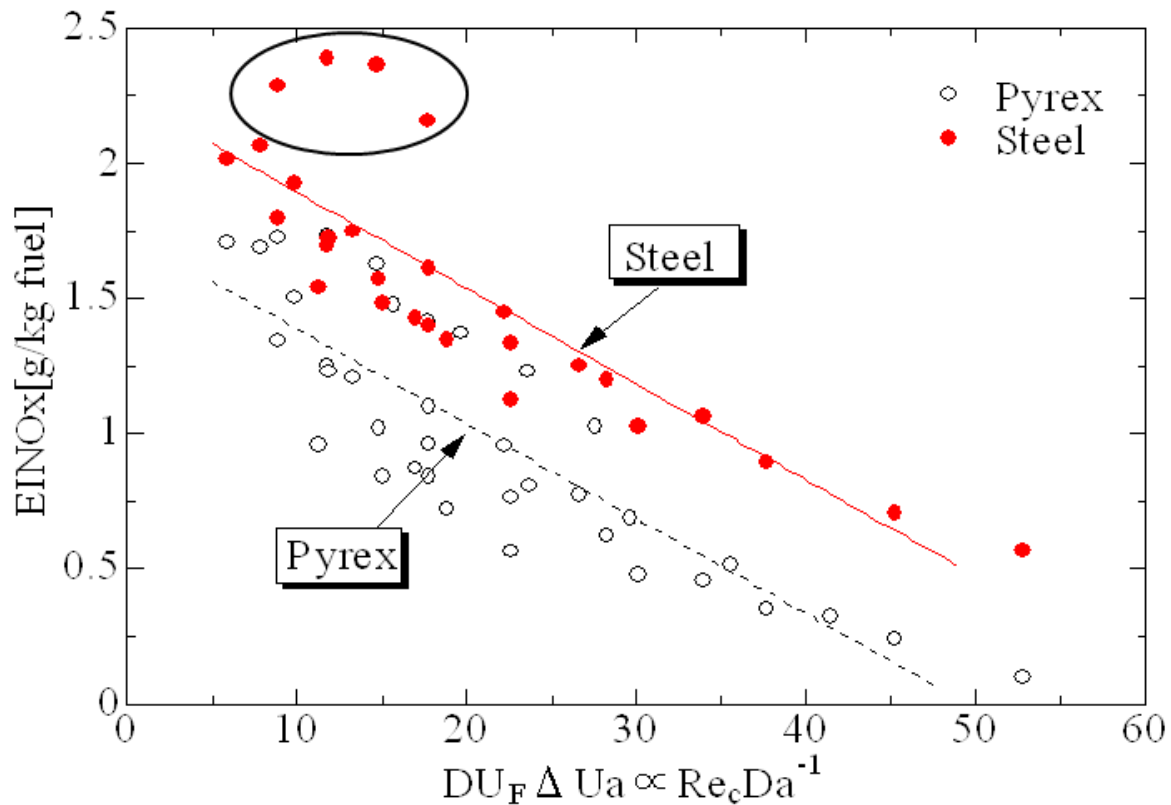


**Fig. 2.8 Radiation effect on EINOx with respect to $DU_F \Delta U_a$**

## 2.6 Conclusions

In this study, the radiation effect on the NOx emission was investigated through the comparison of NOx characteristics between Pyrex glass and stainless steel wall furnaces. The radiation effect under the present conditions is small, and the EINOx difference is almost constant with respect to the parameter of $DU_F \Delta U_a$.

# CHAPTER 3

# NUMERICAL SIMULATION OF CONFINED TURBULENT NON-PREMIXED FLAMES USING A PARTIALLY-STIRRED REACTOR COMBUSTION MODEL

## 3.1    Turbulent non-premixed jet flames

In non-premixed combustion, fuel and oxidizer enter separately into the combustion chamber, in which, they mix and burn during continuous inter-diffusion process. Fuel is supplied by jets of gaseous fuel, which entrain enough air from coaxial air jets so that all the fuel is burned within a certain distance from the nozzle, and that distance is called flame length [24]. There is no propagation in non-premixed flames, and it is located where the fuel and the oxidizer meet. This property is useful for safety purpose; nonetheless it also has consequences on the chemistry-turbulence interaction. Without propagation speed, non-premixed flames are unable to impose its own dynamics on the flow field, and are more sensitive to turbulence. Non-premixed combustion is sometimes called diffusive combustion or combustion in diffusion because diffusion is the rate controlling process. The time needs for convection and diffusion, and both being responsible for turbulent mixing. Turbulent mixing is typically much larger than the time needed for combustion reactions. Turbulent combustion results from the two-way interaction of chemistry and turbulence. When a flame interacts with a turbulent flow, turbulence is modified by combustion because of the strong flow accelerations through the flame front induced by heat release and because of the large changes in kinematic viscosity associated with temperature changes. On the other hands, turbulence alters the flame structure, which may enhance the chemical reaction but also, in extreme cases, completely inhabit it, and then, leads to the flame extinction.

## 3.2    Computational approaches to confined turbulent non-premixed combustion

The description of turbulent combustion process using computational fluid dynamics (CFD) may be achieved using three levels of computations [1]:

● Reynolds-Averaged Navier Stokes (RANS) computation technique was developed to solve for mean values of all quantities. The balance equations of Reynolds or Favre averaged

27

quantities are obtained by averaging the instantaneous balance equations. The average equations require closure rules. A turbulence model is needed to deal with the flow dynamics, whereas a combustion model is used to describe the chemistry-turbulence interaction. Solutions of these equations provide average quantities over time for stationary mean flows.

- In large eddy simulations, (LES), the large eddies in turbulence are explicitly calculated, whereas the effects of smaller eddies are modeled using sub-grid closure rules. The balance equations for LES are obtained by filtering the instantaneous balance equations. LES determines the instantaneous position of a large scale resolved flame front; nonetheless a sub-grid model is still required to take into account the effects of small turbulent scales on combustion.

- In direct numerical simulations (DNS), the full instantaneous Navier Stokes equations are solved without any model for turbulent motions. All turbulence scales are explicitly determined, and their effects on combustion are captured. DNS would predict all time variations of required quantities.

In terms of computational cost, DNS is the most demanding method, and is limited to fairly low Reynolds numbers and simplified geometries. LES works with moderately coarse grids and may be used to deal with higher Reynolds numbers; however it requires sub-grid scale methods. The computational quantity and the results accuracy are directly linked to these physical sub-grid models. In current engineering practices, RANS is extensively used because it is less demanding, in terms of computational resources, nonetheless its validity is limited by the accuracy of closure models, which describe the turbulence-combustion interaction. By considering, the accuracy of turbulent and chemical reaction models and computational limitations, in this study, RANS method is used.

## 3.3 Governing Equations

The governing equations, which describe the fluid-flow, can be derived from the principles of conservation of mass, momentum and energy [1, 25].

General conservation equation for a scalar can be written as;

$$\underbrace{\frac{\partial}{\partial t}(\rho\phi)}_{Unsteady}+\underbrace{\nabla.(\rho U\phi)}_{Convection}=\underbrace{\nabla.(\rho D\nabla\phi)}_{Diffusion}+\underbrace{S(\phi)}_{Source} \qquad (3.1)$$

where $\rho$ is the density, $U$ is the velocity vector, $D$ is the diffusion coefficient, and $\phi$ denotes all conserved scalars.

### 3.3.1 Species conservation

The species mass balance equation in terms of the species mass fraction $Y_i$ is given by;

$$\frac{\partial \rho Y_i}{\partial t}+\nabla.(\rho U Y_i)=\nabla.(\rho D\nabla Y_i)+\dot{\omega}_i \qquad (3.2)$$

where $\dot{\omega}_i$ is the net formation rate of species $i$ ($i = 1,…..,N$) per unit volume. The mass diffusion coefficient, $D$, is defined as;

$$D = \frac{\mu}{\rho Sc} \qquad (3.3)$$

where $\mu$ is the dynamic viscosity and $Sc$ is Schmidt number. Schmidt number is a dimensionless number, which describes the relationship between viscosity and mass diffusivity.

### 3.3.2 Momentum conservation

The momentum conservation is expressed by the equation;

$$\frac{\partial \rho U}{\partial t}+\nabla.(\rho U U)=\nabla.(\underline{\underline{s}})-\nabla p \qquad (3.4)$$

where $p$ is the fluid pressure, and the viscous stress tensor $\underline{\underline{s}}$ for a Newtonian fluid is given by;

$$\underline{\underline{s}} = \mu\left(\nabla U + (\nabla U)^T\right)-\frac{2}{3}\mu((\nabla.U)\mathbf{I} \qquad (3.5)$$

where superscript $T$ denotes for a matrix transpose, and **I** is an identity matrix.

### 3.3.3    Energy conservation

Specific enthalpy, $h_s$, equation is derived based on the first law of thermodynamics.

$$\frac{\partial(\rho h_s)}{\partial t}+\nabla.(\rho \mathbf{U} h_s)=\nabla.(\rho \alpha \nabla h_s)+\nabla.\sum_{i=1}^{N}[h_{si}(\rho D-\rho \alpha)\nabla Y_i]+\dot{\omega}_h \tag{3.6}$$

where $\omega_h$ is the chemical source term of the sensible enthalpy. The thermal diffusion coefficient, $\alpha$, is defined as;

$$\alpha = \frac{\mu}{\rho Pr} \tag{3.7}$$

where $Pr$ is Prandtl number, and it is a dimensionless number, which describes the relationship between viscosity and thermal diffusivity. Moreover,

$$h_s = \sum_{i=1}^{N} Y_i h_{si} \tag{3.8}$$

where;

$$h_{si} = \int_{T_{ref}}^{T} c_{pi} dT \tag{3.9}$$

$T$ is the absolute temperature.

### 3.3.4    State equation

The state relations are assumed to be those of an ideal gas mixture.

$$p = \rho R_0 T \sum_i (Y_i/W_i) \tag{3.10}$$

where $R_o$ is the universal gas constant and $W_i$ is the molecular weight of species $i$

### 3.3.5  Averaging the governing equations

The equations, which are descried so far, constitute closed set equations, and, in principle, they could be solved numerically with appropriate initial and boundary conditions. This method is known as direct numerical simulation; however, this method is computationally prohibitive for high Reynolds numbers and complex geometries. The traditional approach for treating high Reynolds number turbulent flows has been to average the conservation equations. Different types of averaging can be applied, however they all share a common feature; the closed set of instantaneous equations is transformed by averaging into an 'open' set of equations [25]. Two common types of averaging are the Reynolds (un-weighted) and Favre (density-weighted) approach, which are defined as follows;

**Reynolds averaging**

$$\bar{A}(x,t) \equiv \lim_{N \to \infty} \frac{1}{N} \sum_{i=1}^{N} A^{(i)}(x,t) \tag{3.11}$$

**Favre averaging**

$$\tilde{A}(x,t) \equiv \frac{1}{\bar{\rho}} \lim_{N \to \infty} \frac{1}{N} \sum_{i=1}^{N} \rho^{(i)} A^{(i)}(x,t) \tag{3.12}$$

where $A^{(i)}(x,t)$ is the $i^{th}$ realization. A standard practice is to decompose the instantaneous equations into mean and fluctuating parts, and then average them. With density-weighted averaging the velocity and scalars (but not the density and pressure) are decomposed according to

$$\mathbf{u} = \tilde{\mathbf{u}} + \mathbf{u}'' \tag{3.13}$$

$$\phi = \tilde{\phi} + \phi'' \tag{3.14}$$

With the definition of Favre averaging, it can be easily shown that

$$\overline{\rho \mathbf{u}''} = \overline{\rho \phi''} = 0 \tag{3.15}$$

For Reynolds averaging,

$$\mathbf{u} = \overline{\mathbf{u}} + \mathbf{u}' \tag{3.16}$$

$$\phi = \overline{\phi} + \phi' \tag{3.17}$$

where $\overline{\mathbf{u}'} = \overline{\phi'} = 0$ (3.18)

The reason for employing Favre averaging is that the resulting conservation equations do not include terms involving correlations of density fluctuations. Consequently, the resulting equations are easier to interpret, and hence, do not required model than their Reynolds averaged counterparts. Moreover, Favre averaging leads to equations, which describe the mean of conserved quantities. The resulting momentum equation is in terms of $\overline{\rho\mathbf{u}} \equiv \overline{\rho}\widetilde{\mathbf{u}}$ rather than $\overline{\rho}\overline{\mathbf{u}}$, which is obtained from Reynolds averaging and is not conserved. Thus, $\overline{\rho\mathbf{u}} \equiv \overline{\rho}\widetilde{\mathbf{u}} = \overline{\rho}\overline{\mathbf{u}} + \overline{\rho'\mathbf{u}'}$ and $\overline{\rho'\mathbf{u}'}$ can be very difficult to calculate accurately [25]. By applying the Favre averaging into the conservation Eq. of (3.2), (3.4), and (3.6), it yields;

Species conservation

$$\frac{\partial \overline{\rho}\widetilde{Y}_i}{\partial t} + \nabla.(\widehat{\overline{\rho}U\widetilde{Y}_i}) = \nabla.(\overline{\rho D \nabla \widetilde{Y}_i} - \widehat{\overline{\rho}U''Y_i''}) + \overline{\dot{\omega}}_i \tag{3.19}$$

Momentum conservation

$$\frac{\partial \overline{\rho}\widetilde{U}}{\partial t} + \nabla.(\widehat{\overline{\rho}U\widetilde{U}}) = \nabla.(\underline{\widetilde{s}} - \widehat{\overline{\rho}U''\widetilde{U}''}) - \nabla\overline{p} \quad ; \quad \underline{\widetilde{s}} = \mu\left(\nabla\widetilde{U} + \left(\nabla\widetilde{U}\right)^T\right) - \frac{2}{3}\mu\left((\nabla.\widetilde{U}\right)\mathbf{I} \tag{3.20}$$

Energy conservation

$$\frac{\partial(\overline{\rho}\widetilde{h}_s)}{\partial t} + \nabla.(\widehat{\overline{\rho}U\widetilde{h}_s}) = \nabla.(\overline{\rho}\overline{\alpha}\nabla\widetilde{h}_s - \widehat{\overline{\rho}U''h_s''}) + \nabla.\sum_{i=1}^{N}[\widetilde{h}_{si}\left(\overline{\rho D} - \overline{\rho}\overline{\alpha}\right)\nabla\widetilde{Y}_i] + \overline{\dot{\omega}}_h \tag{3.21}$$

32

An unknown terms, which are appeared in Eq.(3.19) to (3.21) are the mean species formation rate $\bar{\dot{\omega}}_i$ owing to the chemical reaction, species turbulent mass flux, $\widehat{\overline{\rho U'' Y''}}$, Reynolds stress $\widehat{\overline{\rho U'' U''}}$, turbulent energy flux $\widehat{\overline{\rho U'' h_s''}}$ and mean chemical energy formation rate $\bar{\dot{\omega}}_h$.

### 3.3.6   Modeling of turbulent flux terms

The simplest turbulence closures are based on the eddy viscosity approach. The Reynolds stress in the momentum Eq. (3.20), and the turbulent mass and energy fluxes in the species (3.19) and energy (3.21) equations are assumed to be linearly related to the mean rate of strain rate via eddy viscosity [1].

$$\widehat{\overline{\rho U'' U''}} = -\mu_T \left[ \nabla \tilde{U} + \left( \nabla \tilde{U} \right)^T \right] + \frac{2}{3} \bar{\rho} \tilde{k} \mathbf{I} + \frac{2}{3} \mu_T \left( \nabla . \tilde{U} \right) \mathbf{I} \tag{3.22}$$

$$\widehat{\overline{\rho U'' Y''}} = -\frac{\mu_T}{Sc_T} \nabla \tilde{Y} \tag{3.23}$$

$$\widehat{\overline{\rho U'' h_s''}} = -\frac{\mu_T}{Pr_T} \nabla \tilde{h}_s \tag{3.24}$$

Eddy viscosity is given by;

$$\mu_T = C_\mu \bar{\rho} \frac{\tilde{k}^2}{\tilde{\varepsilon}} \tag{3.25}$$

where $C_\mu$ is the constant with the standard value of 0.09, and the values of $k$ and $\varepsilon$ are obtained from the solutions of the modeled transport equations of the turbulent kinetic energy $k$ and its dissipation rate $\varepsilon$, respectively.

### 3.3.7   The k - ε turbulence model

The Favre average turbulent kinetic energy $\tilde{k}$ and its dissipation rate $\tilde{\varepsilon}$ are defined as follows [1, 25].

$$\tilde{k} = \frac{1}{2} \widehat{U'' U''} \tag{3.26}$$

33

$$\tilde{\varepsilon} = \frac{\mu}{\rho}\left[\nabla U'' + (\nabla U'')^T\right]\cdot\nabla U'' \tag{3.27}$$

The values of $\tilde{k}$ and $\tilde{\varepsilon}$ are obtained from the solutions of the modeled transport equations as shown in Eq. (3.28) and (3.29), respectively.

$$\frac{\partial(\bar{\rho}\tilde{k})}{\partial t} + \nabla\cdot(\bar{\rho}\tilde{U}\tilde{k}) = \nabla\cdot\left(\frac{\mu_{eff}}{\mathrm{Pr}_k}\nabla\tilde{k}\right) + [\underline{\underline{\tilde{s}}}:\nabla\tilde{U} - \bar{\rho}\tilde{\varepsilon}] \tag{3.28}$$

$$\frac{\partial(\bar{\rho}\tilde{\varepsilon})}{\partial t} + \nabla\cdot(\bar{\rho}\tilde{U}\tilde{\varepsilon}) = \nabla\cdot\left(\frac{\mu_{eff}}{\mathrm{Pr}_\varepsilon}\nabla\tilde{\varepsilon}\right) + [\frac{\tilde{\varepsilon}}{\tilde{k}}\left(c_{\varepsilon 1}(\underline{\underline{\tilde{s}}}:\nabla\tilde{U}) - c_{\varepsilon 2}\bar{\rho}\tilde{\varepsilon}\right)] \tag{3.29}$$

In Eq. of (3.28) and (3.29), the two terms, on the left hand side, represent the local rate of temporal change and convection, respectively. The first term, on the right hand side, represents the turbulent diffusion, and the second one composed of turbulent production and the turbulent dissipation.

The model constants are assigned standard values as; $c_{\varepsilon 1} = 1.44, c_{\varepsilon 2} = 1.92, \mathrm{Pr}_k = 1.0, \mathrm{Pr}_\varepsilon = 1.3$

The dissipation $\varepsilon$ plays a fundamental role in turbulent theory. The eddy cascade hypothesis states that it is equal to the energy transfer rate from the large eddies to the smaller eddies, and thus, it is invariant within the inertial sub-range of turbulence.

## 3.4 Turbulent combustion models

The production rate of species $i$, $(\dot{\omega}_i)$, $(g/\mathrm{cm}^3\mathrm{s})$, in Eq. (3.2), is evaluated based on the Arrhenius law as shown in Eq. (3.30) and (3.31) [1].

$$\dot{\omega}_i = W_i \sum_{l=1}^{nrk}(v_{il}'' - v_{il}')\left[k_{fl}\prod_{n=1}^{ns}\left(\frac{\rho_n}{W_n}\right)^{v_{nl}'} - k_{bl}\prod_{n=1}^{ns}\left(\frac{\rho_n}{W_n}\right)^{v_{nl}''}\right] \tag{3.30}$$

$$k_l = AT^\theta \exp(-E/R_0 T) \tag{3.31}$$

where $v'_{il}$ is the stoichiometric coefficient of reactant $i$ in reaction $l$, and $v''_{il}$ is the stoichiometric coefficient of product $i$ in reaction $l$, $k_{fl}$ and $k_{bl}$ are the forward and backward reaction rate coefficients of reaction $l$, respectively. As shown in the equation 3.31, the reaction rate coefficient is typically exponential function of temperature, $T$, pre-exponential constant, $A$, activation energy, $E$, and universal gas constant, $R_0$. Moreover, $\rho_n$ is the product of mixture density, and the mass fraction of species $n$; i.e. $(\rho_n = \rho Y_n)$. In addition, $W_n$ is the molecular weight of species $n$.

In turbulent reactive flows, temperature and species compositions are random functions of space and time as shown in Fig. 3.1. Because of the non-linear dependence of the production rate, on temperature and compositions, the time average of the Reynolds decomposition of the species production rates yields a large number of terms, of which, most are unknown higher order correlations, as illustrated in the following section.

Let us consider a single step, irreversible, and elementary reaction.

$$A + B \rightarrow C \tag{3.32}$$
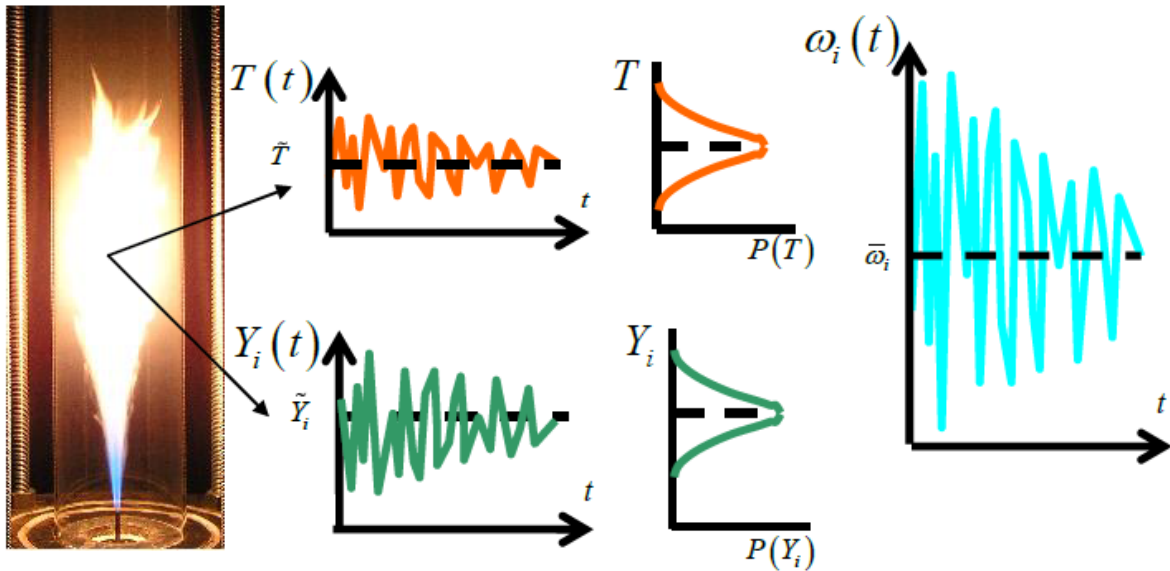


**Fig. 3.1 A Schematic on fluctuations of the turbulent chemical reaction rate**

35

Instantaneous production rate of C $\left(g/cm^3 s\right)$ can be written, according to Eq. (3.30) and (3.31), as follows.

$$\dot{\omega}_c = \rho^2 W_A^{-1} W_B^{-1} W_c A T^\theta \exp\left(\frac{-E}{R_0 T}\right) Y_A Y_B \qquad (3.33)$$

Then, the mean reaction rate is given by;

$$\begin{aligned}\overline{\dot{\omega}}_c &= \overline{\rho}^2 W_A^{-1} W_B^{-1} W_c A \exp\left(E/R\overline{T}\right)\overline{Y}_A \overline{Y}_B * \{1 + \frac{\overline{\rho'^2}}{\overline{\rho}^2} + \frac{\overline{Y_A' Y_B'}}{\overline{Y}_A \overline{Y}_B} + \frac{2\overline{\rho' Y_A'}}{\overline{\rho}\overline{Y}_A} + \frac{2\overline{\rho' Y_B'}}{\overline{\rho}\overline{Y}_B} \\ &+ \frac{E}{R_0\overline{T}}\left[\frac{\overline{Y_A' T'}}{\overline{Y}_A\overline{T}} + \frac{\overline{Y_B' T'}}{\overline{Y}_B\overline{T}} + \left(\frac{E}{2R_0\overline{T}} - 1\right)\frac{\overline{T'^2}}{\overline{T}^2}\right] + \ldots\ldots\ldots\ldots\ldots\ldots\ldots\ldots\ldots\} \end{aligned} \qquad (3.34)$$

In Eq. (3.34), higher order terms do not converge, and it is very difficult to model all unknown correlations. Hence, the chemical source terms are averaged by integrating the product of the species production rates with the joint probability density function (joint PDF) of temperature and composition at the each spatial location, as shown in Eq. (3.35).

$$\overline{\dot{\omega}}_i = \int \dot{\omega}_i\left(\hat{T},\hat{Y}_1,\hat{Y}_2,\ldots,\hat{Y}_{NS}\right) P\left(\hat{T},\hat{Y}_1,\hat{Y}_2,\ldots,\hat{Y}_{NS}\right) d\hat{T} d\hat{Y}_1 d\hat{Y}_2,\ldots, d\hat{Y}_{NS} \qquad (3.35)$$

where $\overline{\dot{\omega}}_i$ is the mean reaction rate, $\dot{\omega}_i$ is instantaneous reaction rate, $P$ is the joint PDF of temperature and species compositions.

The integration, in the above expression (3.35), is taken over all realizable values of temperature and compositions, and the independent variables of the joint PDF represent the sample space of the random variables $T$ and $Y_i$. If the PDF of temperature and compositions are known, then the average of the chemical source terms can be evaluated exactly.

The PDF method was suggested by Pope [26] in 1985. The aim of the method is to calculate the properties of turbulent reactive flow fields. At each point in the flow field, a complete statistical description of the state of the fluid is provided by the velocity-composition joint PDF. This is the joint PDF of the three components of velocity and of the composition variables (species mass fractions and enthalpy). This method is to solve a modeled transport equation for the velocity-

composition joint PDF. For a variable-density flow, with arbitrarily complex and nonlinear reactions, it is remarkable that in this equation the effects of convection, reaction, body forces and the mean pressure gradient appear exactly, and thus, do not have to be modeled. Even though the joint PDF is a function of many independent variables, its transport equation can be solved by a Monte Carlo method [27] for the inhomogeneous flows of practical interest. Even though PDF approach is more elaborate and consequently, this method is computationally more expensive.

As an alternative to the highly computational expensive PDF method, Girimaji [28] has suggested the assumed PDF approach, in which the form of PDF is assumed and completely defined according to the information of only the first and second moments. In the assumed PDF approach, it is for simplicity assumed that statistical independence between temperature and composition [28].

$$\overline{\dot{\omega}}_i = \int \dot{\omega}_{i,T}\left(\hat{T}\right)\widetilde{P}_T\left(\hat{T}\right)\dot{\omega}_{i,Y}\left(\hat{Y}_1,\hat{Y}_2,....\hat{Y}_{NS}\right)\widetilde{P}_Y\left(\hat{Y}_1,\hat{Y}_2,....\hat{Y}_{NS}\right)\delta\left(\hat{\rho}-\overline{\rho}\right)d\hat{T}d\hat{Y}_1d\hat{Y}_2......d\hat{Y}_{NS} \qquad (3.36)$$

The temperature PDF, $\widetilde{P}_T\left(\hat{T}\right)$, and composition PDF , $\widetilde{P}_Y\left(\hat{Y}_1,\hat{Y}_2,..........\hat{Y}_{NS}\right)$, are approximated by an uni-variate beta function and a multivariate beta function, respectively [29, 30]. However, as a number of species increases, this technique leads to the ambiguity in the interaction between turbulence and reactions, especially in terms of minor species, because it needs to construct several marginal PDFs to evaluate of each chemical source term.

A sophisticated idea regarding turbulent combustion modeling was presented by Golovitchev et al. [31], called as a partially-stirred-reactor (PaSR) model. Under highly turbulent intensity, turbulence primarily influences combustion, and the influence of finite-rate chemistry is never negligible. The formation of archipelagos of unburnt gas pockets behind the flame front is regarded as the main consequence of this model. Therefore, PaSR has been generalized to account the effect of the mixture imperfection. This model is similar to the turbulent-dissipation approach, but this model can account for detailed finite-rate chemistry.

The PaSR model expresses the concept that the combustion in the reactor is a sequential process, in which the chemical reaction (process I) is followed by the mixing (process II) as shown in Fig. 3.2, and that, in any process, the rates of individual processes and the overall process must be

37
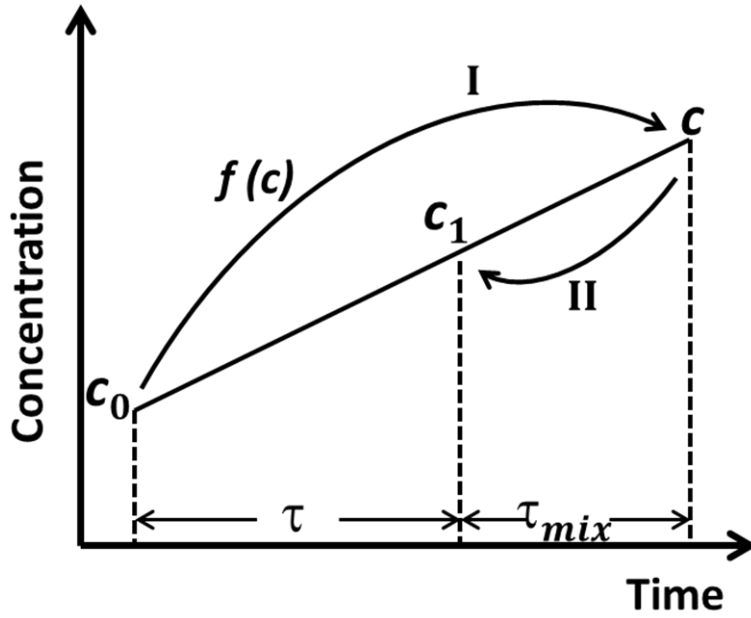
**Fig. 3.2 Process diagram of the PaSR**

equal. The model distinguishes between the concentration in the reactor exit, $c_1$, concentration in the reaction zone, $c$, and concentration in the feed, $c_0$, as shown in Fig.3.2. The rates of the processes I and II in the reactor are assumed to be linear:

$$\frac{dc}{d\tau} = \frac{c_1 - c_0}{\tau} = -\frac{c}{\tau_c} = \frac{c - c_1}{\tau_{mix}} \tag{3.37}$$

where $\tau$ is the progression of time, $\tau_c$ is the chemical-reaction time, and $\tau_{mix}$ is the micro-mixing time. After some algebraic manipulations:

$$\frac{dc}{d\tau} = -\frac{c_1}{\tau_{mix} + \tau_c}. \tag{3.38}$$

Equation (3.38) shows that the turbulent-combustion time is the summation of mixing and reaction times. The model is generalized by the substituting the Arrhenius reaction rate, $f_r(c)$, (as shown in Eq. (3.30)) in to Eq. (3.37).

$$\frac{dc}{d\tau} = \frac{c_1 - c_0}{\tau} = f_r(c) = \frac{c - c_1}{\tau_{mix}} \tag{3.39}$$

A combination of the second and fourth parts of Eq. (3.39) leads to the definition of the reactor volume ratio, $K^*$,

$$c_1 = cK^* + c_0\left(1 - K^*\right)$$

(3.40)

where

$$K^* = \frac{\tau}{\tau_{mix} + \tau}$$

(3.41)

Finally, after algebraic manipulations, the turbulent combustion reaction rate can be expressed in terms of the reactor exit parameters.

$$\left(\frac{c_1 - c_0}{\tau}\right) = f_r(c_1)\left(\frac{\tau_c}{\tau_c + \tau_{mix}}\right)$$

(3.42)

Micro-mixing time can be calculated using Eq. (3.43)

$$\tau_{mix} = C_{mix}\sqrt{\frac{\mu_{eff}}{\bar{\rho}\tilde{\varepsilon}}}$$

(3.43)

In this study, $C_{mix}$ is a tuning constant and it is set to 0.005.

## 3.5    Chemical kinetics models and *in-situ* adaptive tabulation

The global chemistry kinetics of hydrocarbon fuels, which was developed by Westbrook et al. [32], consists of single-step or two-step Arrhenius kinetics for the fuel oxidation. The kinetics is optimized to reproduce the main features of laminar premixed flames by tuning activation energy, pre-exponential factor, and reaction orders of the fuel and oxidizer. However, when used in non-premixed combustion, this kinetics yields reaction rates beyond the flammability range. Therefore, the amount of heat released per mole of fuel is overestimated especially on the fuel-rich side [33]. In this study, the flammability range is not considered with the PaSR combustion model, and thus, it would result in overprediction of temperature. Hence, this study considers a detailed kinetic model for the propane-air oxidation. Djavdan et al. [34] proposed and validated an augmented-starting mechanism for propane-air combustion, which includes 28-species and 69-elementary reaction steps. This mechanism, which improved the reduced propane-air

mechanism proposed by Paczko et al. [35], was compared with the detailed propane-air chemical kinetic model of Warnatz, which involves 32 species and 123 reaction steps [34]. The 69-step/28-species kinetics showed a good agreement with the Warnatz mechanism with a fair degree of precision [34], and was also computationally less expensive. Thus, in this study, the Djavdan propane-air mechanism was selected to use in PaSR model. The Djavdan and Warnatz kinetics model are shown in Appendix A and Appendix B, respectively.

The use of the detailed chemistry model has become a fundamental prerequisite for the PaSR concept. Chemical-characteristic time is much smaller than flow-characteristic time. Therefore, splitting the operator approach is appropriate, in which variations at the molecular level resulting from the CFD time-step, reaction and molecular mixing, are evaluated separately from the contributions of convection and diffusion. The *in-situ* Adaptive Tabulation (ISAT) algorithm, which was developed by Pope [36], is a storage/retrieval technique that is used calculated the composition change owing to the chemical reaction. The accuracy of the ISAT algorithm depends on a specified ISAT- absolute-error tolerance ($1 \times 10^{-6}$), which controls the error occurred during retrieval from the ISAT table. Based on Pope, Contino et al. [37] developed a library called as the tabulation of dynamic adaptive chemistry for OpenFOAM. This study uses this library to reduce the impact of the detailed propane oxidation on the computational cost.

## 3.6    NOx Modeling

Several studies on NOx formation have been reported in the literature [38-42].There are several possible means of producing nitric oxide in diffusion flames; for all of the mechanisms, the relevant reaction rates are slow with respect to the overall rate of combustion for the primary fuel. Thus, in calculating emissions in combustion, it is necessary to take into account the finite rates of the associated reactions. Moreover, the NO production is strongly influenced by the flame temperature and radical concentrations; hence, these must be modeled carefully. In this study, four routes to NO formation are considered. These are the thermal mechanism (thermal-NO), the prompt mechanism (prompt-NO), the nitrous-oxide ($N_2O$) mechanism, and NO production through the oxidation of NNH, as shown in Table 3.1. If NO concentrations are significant enough, reburn reactions, which lead from NO back to $N_2$, can become important, and these are also considered in this study (NO-reburning). The NOx  kinetics [39] is shown in Appendix C.

**Table 3.1 NOx mechanisms from GRI 2.11 [39]**

| Reaction No. | Reaction | Reaction No. | Reaction | Reaction No. | Reaction |
|---|---|---|---|---|---|
| 178 | N+NO<=>N2+O  (Thermal NO) | 212 | H+NO+M<=>HNO+M | 246 | CH+NO<=>HCN+O |
| 179 | N+O2<=>NO+O | 213 | HNO+O<=>NO+OH | 247 | CH+NO<=>H+NCO |
| 180 | N+OH<=>NO+H | 214 | HNO+H<=>H2+NO | 248 | CH+NO<=>N+HCO |
| 181 | N2O+O<=>N2+O2  (N2O) | 215 | HNO+OH<=>NO+H2O | 249 | CH2+NO<=>H+HNCO |
| 182 | N2O+O<=>2NO | 216 | HNO+O2<=>HO2+NO | 250 | CH2+NO<=>OH+HCN |
| 183 | N2O+H<=>N2+OH | 217 | CN+O<=>CO+N | 251 | CH2+NO<=>H+HCNO |
| 184 | N2O+OH<=>N2+HO2 | 218 | CN+OH<=>NCO+H | 252 | CH2(S)+NO<=>H+HNCO |
| 185 | N2O(+M)<=>N2+O(+M) | 219 | CN+H2O<=>HCN+OH | 253 | CH2(S)+NO<=>OH+HCN |
| 186 | HO2+NO<=>NO2+OH  (NO2) | 220 | CN+O2<=>NCO+O | 254 | CH2(S)+NO<=>H+HCNO |
| 187 | NO+O+M<=>NO2+M | 221 | CN+H2<=>HCN+H  (NO reburning) | 255 | CH3+NO<=>HCN+H2O |
| 188 | NO2+O<=>NO+O2 | 222 | NCO+O<=>NO+CO | 256 | CH3+NO<=>H2CN+OH |
| 189 | NO2+H<=>NO+OH | 223 | NCO+H<=>NH+CO | 257 | HCNN+O<=>CO+H+N2 |
| 190 | NH+O<=>NO+H  (Prompt NO) | 224 | NCO+OH<=>NO+H+CO | 258 | HCNN+O<=>HCN+NO |
| 191 | NH+H<=>N+H2 | 225 | NCO+N<=>N2+CO | 259 | HCNN+O2<=>O+HCO+N2 |
| 192 | NH+OH<=>HNO+H | 226 | NCO+O2<=>NO+CO2 | 260 | HCNN+OH<=>H+HCO+N2 |
| 193 | NH+OH<=>N+H2O | 227 | NCO+M<=>N+CO+M | 261 | HCNN+H<=>CH2+N2 |
| 194 | NH+O2<=>HNO+O  (Prompt NO) | 228 | NCO+NO<=>N2O+CO  (N2O) | 262 | HNCO+O<=>NH+CO2 |
| 195 | NH+O2<=>NO+OH | 229 | NCO+NO<=>N2+CO2 | 263 | HNCO+O<=>HNO+CO |
| 196 | NH+N<=>N2+H | 230 | HCN+M<=>H+CN+M | 264 | HNCO+O<=>NCO+OH |
| 197 | NH+H2O<=>HNO+H2 | 231 | HCN+O<=>NCO+H | 265 | HNCO+H<=>NH2+CO |
| 198 | NH+NO<=>N2+OH | 232 | HCN+O<=>NH+CO | 266 | HNCO+H<=>H2+NCO |
| 199 | NH+NO<=>N2O+H  (N2O) | 233 | HCN+O<=>CN+OH | 267 | HNCO+OH<=>NCO+H2O |
| 200 | NH2+O<=>OH+NH | 234 | HCN+OH<=>HOCN+H | 268 | HNCO+OH<=>NH2+CO2 |
| 201 | NH2+O<=>H+HNO | 235 | HCN+OH<=>HNCO+H | 269 | HNCO+M<=>NH+CO+M |
| 202 | NH2+H<=>NH+H2 | 236 | HCN+OH<=>NH2+CO | 270 | HCNO+H<=>H+HNCO |
| 203 | NH2+OH<=>NH+H2O | 237 | H+HCN+M<=>H2CN+M | 271 | HCNO+H<=>OH+HCN |
| 204 | NNH<=>N2+H  (NNH) | 238 | H2CN+N<=>N2+CH2 | 272 | HCNO+H<=>NH2+CO |
| 205 | NNH+M<=>N2+H+M | 239 | C+N2<=>CN+N | 273 | HOCN+H<=>H+HNCO |
| 206 | NNH+O2<=>HO2+N2 | 240 | CH+N2<=>HCN+N | 274 | HCCO+NO<=>HCNO+CO |
| 207 | NNH+O<=>OH+N2 | 241 | CH+N2(+M)<=>HCNN(+M) | 275 | CH3+N<=>H2CN+H |
| 208 | NNH+O<=>NH+NO | 242 | CH2+N2<=>HCN+NH | 276 | CH3+N<=>HCN+H2 |
| 209 | NNH+H<=>H2+N2 | 243 | CH2(S)+N2<=>NH+HCN | 277 | NH3+H<=>NH2+H2  (NH3) |
| 210 | NNH+OH<=>H2O+N2 | 244 | C+NO<=>CN+O  (NH3) | 278 | NH3+OH<=>NH2+H2O |
| 211 | NNH+CH3<=>CH4+N2 | 245 | C+NO<=>CO+N | 279 | NH3+O<=>NH2+OH |

The thermal mechanisms are long recognized as a source for nitric oxide in flames, and it was calculated through the Zel'dovich mechanisms (R178-R180), as shown in Table 3.1, where R denotes the reaction number of GRI 2.11[39]. The reaction R178, with the large activation energy, is the rate-controlling step, and the very strong temperature dependence, associated with its high activation energy, implies that accurate knowledge of the peak temperature is crucial in obtaining correct predictions for emissions. Since the rate of this step also proportional to O-atom concentration, accurate results for the radical-O, in the flame, are also needed.

The reactions, between $N_2$ and hydrocarbon radicals, lead to what is commonly referred to as prompt NO; this mechanism is also known as the Fenimore mechanism. The prompt NO formation is started through the reactions R240-R243 to form HCN, which is then subsequently oxidized to NO, as pointed out by Ju et al. [41] and Cho et al. [42]. Cho et al. [42] have made the NOx mechanisms reaction-path diagram for better understanding of the prompt NO formation, as shown in Fig.3.3.

**Fig. 3.3 NOx reaction paths for a case of $\phi = 0.9$ [42]**

According to Fig. 3.3, the main routes of the formation of prompt NOx are HCN→ HOCN→HNCO→$NH_2$ → NH →HNO →NO and HCN → NCO → NH→HNO→NO.

In the $N_2O$ mechanism, $N_2$ is converted to $N_2O$, and then NO through the reactions R181-R185, R199, and R228. At the lower temperature and oxygen-rich conditions, the $N_2O$ route is more important. Hence, as $\phi$ is increased, the oxygen concentration decreases, and thus, the $N_2O$ emission decreases.

The NO production by the oxidation of NNH radicals was proposed by Bozzelli and Dean [43]. They found that significant amounts of NO can be produced in combustion from $N_2$ via NNH, and then NNH radicals are oxidized into NO, as illustrated in the reaction R208, in Table 3.1. The importance of NNH mechanism has been investigated through a number of experimental and numerical studies in hydrocarbon flames, and especially, Galletti et al. [44] recently found that

the NNH intermediate route must be taken into account in the mild combustion of hydrogen containing fuels.

The NO-reburning mechanism denotes a group of reactions, (R244-R276), in which NO is reduced by hydrocarbon radicals ($CH_i$). The reduction of NO by reburning is influenced by fuel mixing, temperature, stoichiometry, and gas residence time [45].

In addition to NO and $N_2O$, nitrogen dioxide ($NO_2$) is also an important pollutant arising from the reactions of nitrogen-containing species. $NO_2$ is formed from NO on the lean side of the flame, and it is a significant emission. Generally, however, emissions are reported in terms of the summation of NO, $N_2O$ and $NO_2$ emissions. Since the $NO_2$ is formed through NO, as illustrated in reactions (R186-R189) in Table 3.1, its formation does not alter the total pollutant emissions.

Hewson et al. [40] showed that when peak temperature is reduced, the nitric-oxide production is minimized, and prompt mechanism is generally the dominant route for the formation of NOx. In addition, this study showed that reburning chemistry is significant in flames, and neglecting prompt and reburning chemistries leads to the underprediction of NOx emissions for short residence times and its overprediction for long residence times, respectively. Ju et al. [41] demonstrated that prompt and thermal mechanisms are strongly coupled. The conventional method, which decoupled thermal and prompt mechanisms, considerably overpredicts the thermal NO and underpredicts the prompt NO. Therefore, this study employs the detailed NOx formation mechanism extracted from GRI 2.11 [39]. However, detailed NOx mechanisms have many uncertainties. Cao and Pope [46] showed that NOx formation of GRI 3.0 [47] overpredicts the experimental results of methane-air non-premixed combustion whereas the GRI 2.11 evaluates NOx reasonably well with the PDF combustion model.

## 3.7    Numerical models and conditions

In this study, the flow-calculation software OpenFOAM [48], which is a high-fidelity open source code, is employed as a finite-volume solver for Reynolds-averaged Navier-Stokes (RANS) equations, and the $k$-$\varepsilon$ model is used to model the turbulent flux terms in RANS equations, as described in Section 3.3.7. A Furnace consist of the cylindrical combustion
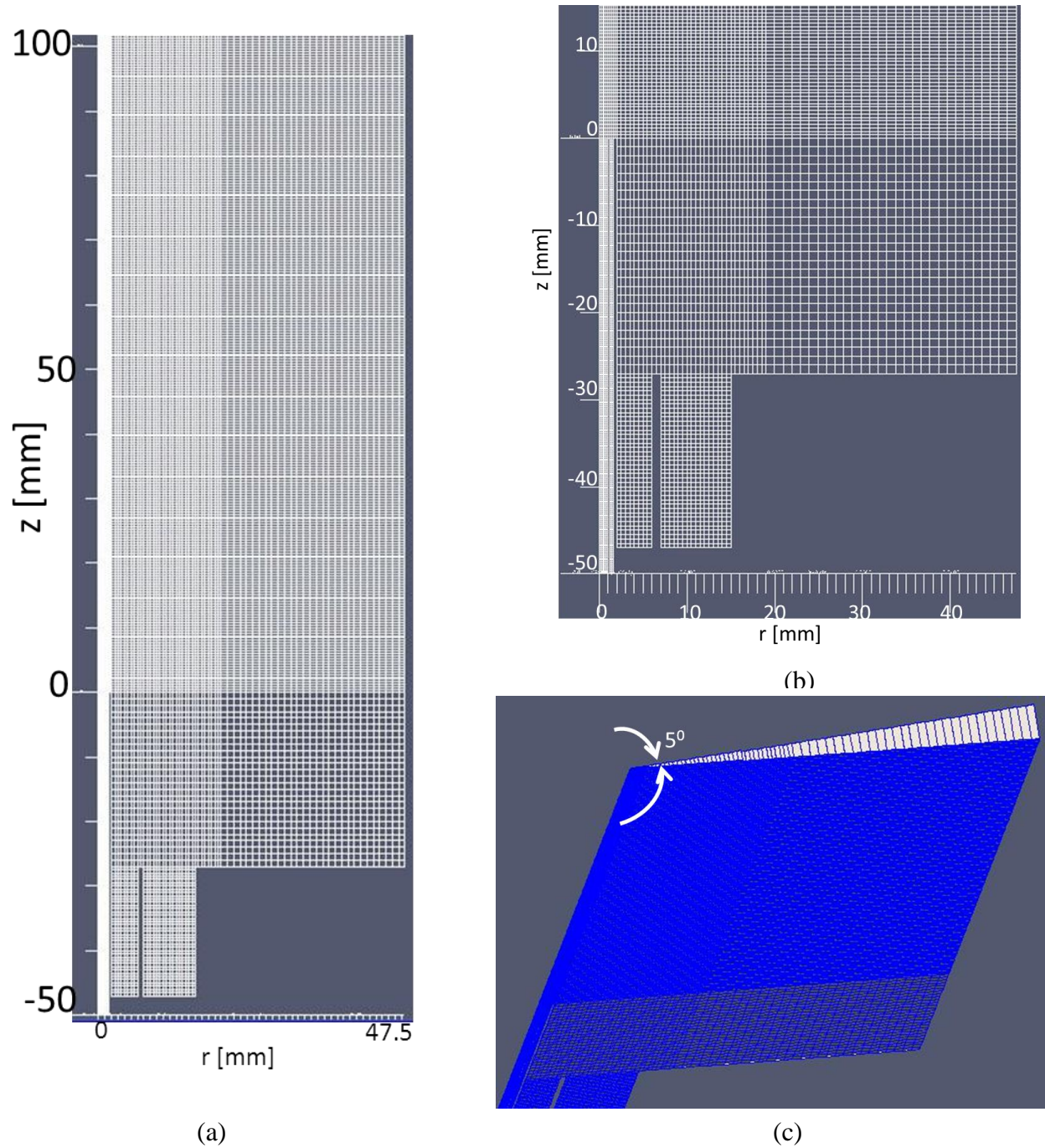
**Fig. 3.4 Calculation grid configuration (a) 2-D view of burner and upstream region of combustion chamber (b) Enlarged 2-D view of burner configuration (c) 3-D view of grid structure**

chamber, which is installed vertically, and a burner is installed at the center of the bottom of the chamber, and more details of the geometry can be found in Section 2.2. The upstream region of

the axi-symmetric calculation domain is shown in Fig. 3.4 (a), and the numerical simulation was performed in the three-dimensional grids using the periodic boundary condition. The geometry is specified as a wedge of small angle ($<5^0$), and one cell thickness is running along the plane of symmetry, which straddling one of the coordinate planes, as shown in Fig. 3.4 (c). The inner diameter of chamber is 95 mm, and the height is 840 mm. The calculation grids were concentrated at the flame region, and the smallest grid size was 0.2 mm. Thus, the computational domain was discretized to 120,000 grid cells. In order to get the fully-developed turbulent flow profile at the exit of the fuel nozzle, in this study, the nozzle inlet was located 50 mm upstream from the exit, as shown in Fig. 3.4 (b). Propane was used as the main-fuel, whereas hydrogen was used as the pilot-fuel. The global equivalence ratios were 0.4, 0.6, and 0.8; initial flow velocities are shown in Table 1.1. The total air flow rate was fixed at 0.002 m$^3$/s, and the high and low air velocities of two air annular nozzles were 9.8 and 1.8 m/s, respectively. A turbulence intensity of 10% was set for both fuel and air-inlet flows. The furnace walls were non-slip and adiabatic, and the outlet was specified by the continuity boundary condition. The reactingFOAM solver is based on the unsteady pressure implicit splitting of operation algorithm with two pressure correctors and two momentum correctors per time-step. The initial CFD time-step was selected as $1\times 10^{-6}$ s with a corresponding Courant number of approximately 0.4, whereas the initial chemical time-step was selected as $1\times 10^{-7}$ s. Numerical results have been compared with experimental measurements of stainless wall furnaces, but the experimental data for $\phi = 0.8$ were not available.

## 3.8    Results and discussion

### 3.8.1   Flow Field

The radial distributions of the mean axial velocity in terms of global equivalence ratio, $\phi$, at axial distances of $z = 25$ mm through $z = 200$ mm are shown together with the experimental data in Figs. 3.5 (a), (b) and (c). The tilde symbol of the mean is henceforth ignored in figures. There is a good agreement between the velocity predictions and experimental data. Both the shapes and peak values of the radial distributions of the mean axial velocity are accurately captured. The increase in $\phi$ corresponds to the increase in the fuel flow rate. Therefore, axial velocities near the center for $\phi = 0.8$ result in higher velocities than others, at each cross section. However, each velocity distribution is very similar. The axial velocities near the furnace wall show negative
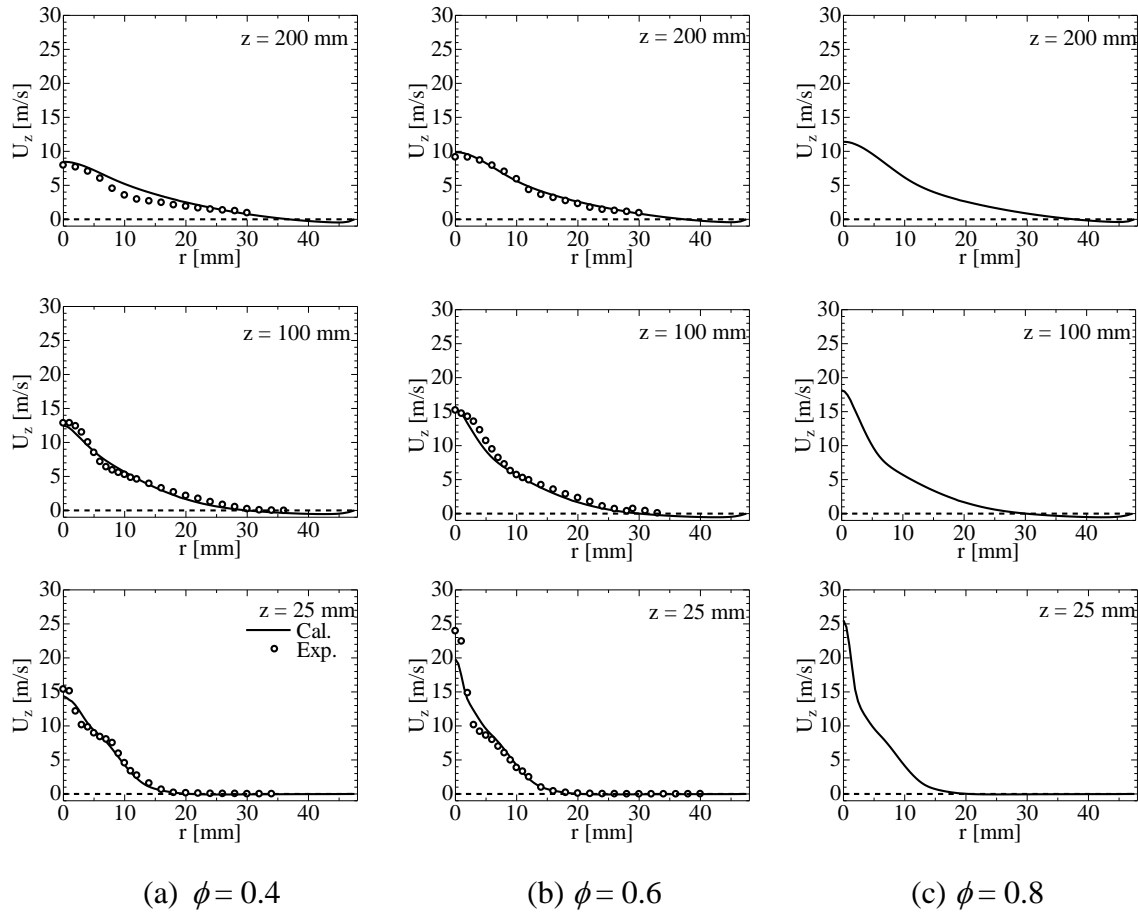
**Fig. 3.5 Radial distributions of mean axial velocity in terms of $\phi$**

values, which clearly indicate the existence of a recirculation vortex between the flame boundary and furnace wall. Therefore, the flow field consists of two zones: recirculation and jet-like propagation zones. Figures 3.6 (a) and (b) show the vector maps of flow fields to the upstream and downstream of the combustion chamber, respectively, for $\phi = 0.4$. The vector maps of flow fields for $\phi = 0.6$ and 0.8 show similar flow fields to $\phi = 0.4$, not shown here. The arrows of the vector are not in the scale, and the colored bar shows the magnitude of velocity vector. Moreover, Figs. 3.6 (a) and (b) show a recirculation vortex generated between the fuel jet and the wall. Therefore, this vortex should lead the entrainment of burnt gases to the flame and the dilution in confined flames.

46
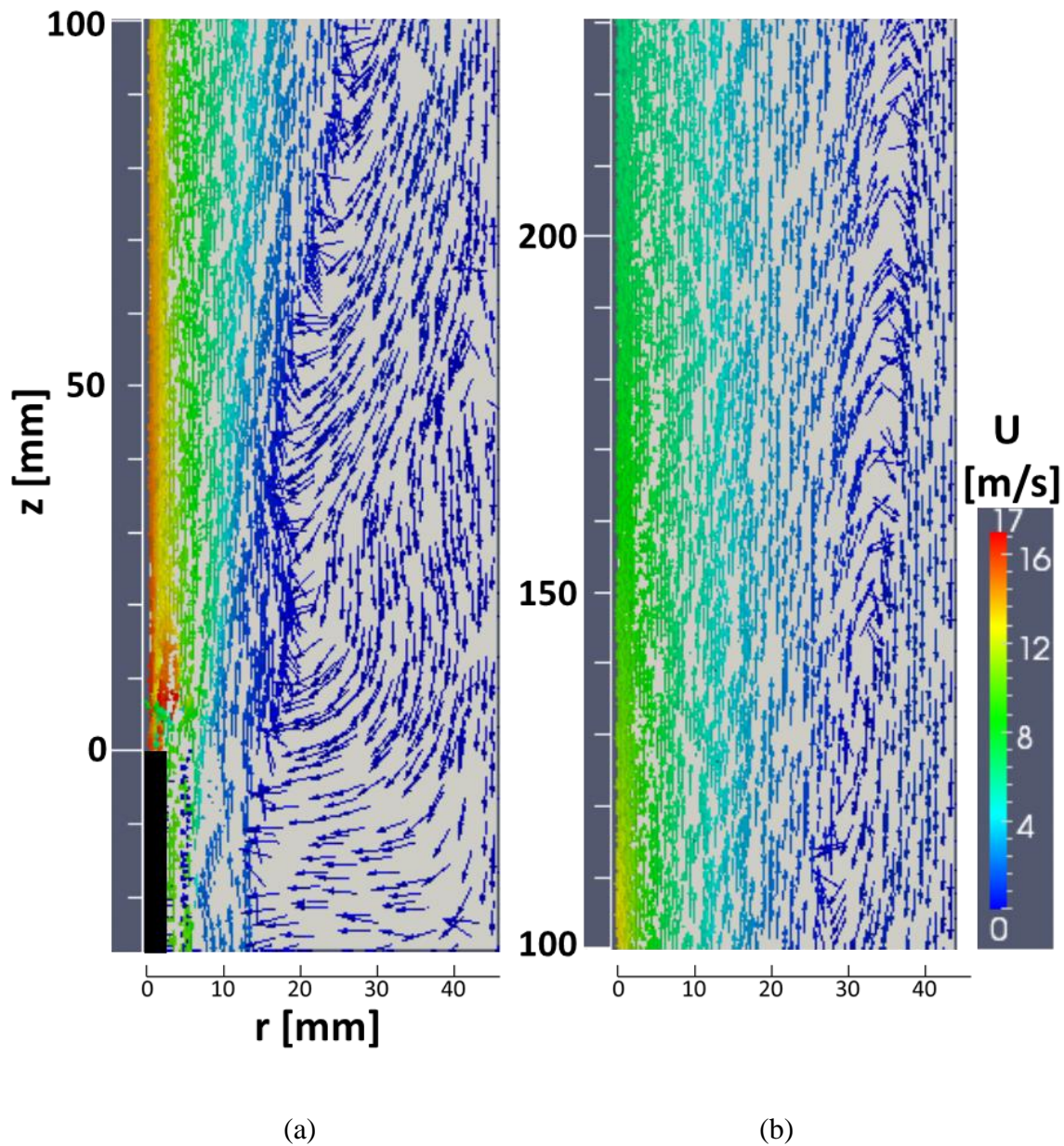
**Fig. 3.6 Vector maps of flow field in combustion chamber for $\phi = 0.4$ (a) Upstream (z = -27 mm to 100 mm) (b) Downstream (z = 100 mm to 230 mm)**

These results are based on the standard two-equation $k$-$\varepsilon$ model used as a turbulent model. It is well known that the $k$-$\varepsilon$ model overpredicts the decay rate and the spreading rate of a round jet flow. Pope [49] has suggested that, in a round jet flow, the stretching of turbulent vortex tubes by the mean flow has a significant influence on the process of scale reduction. As the jet spreads,
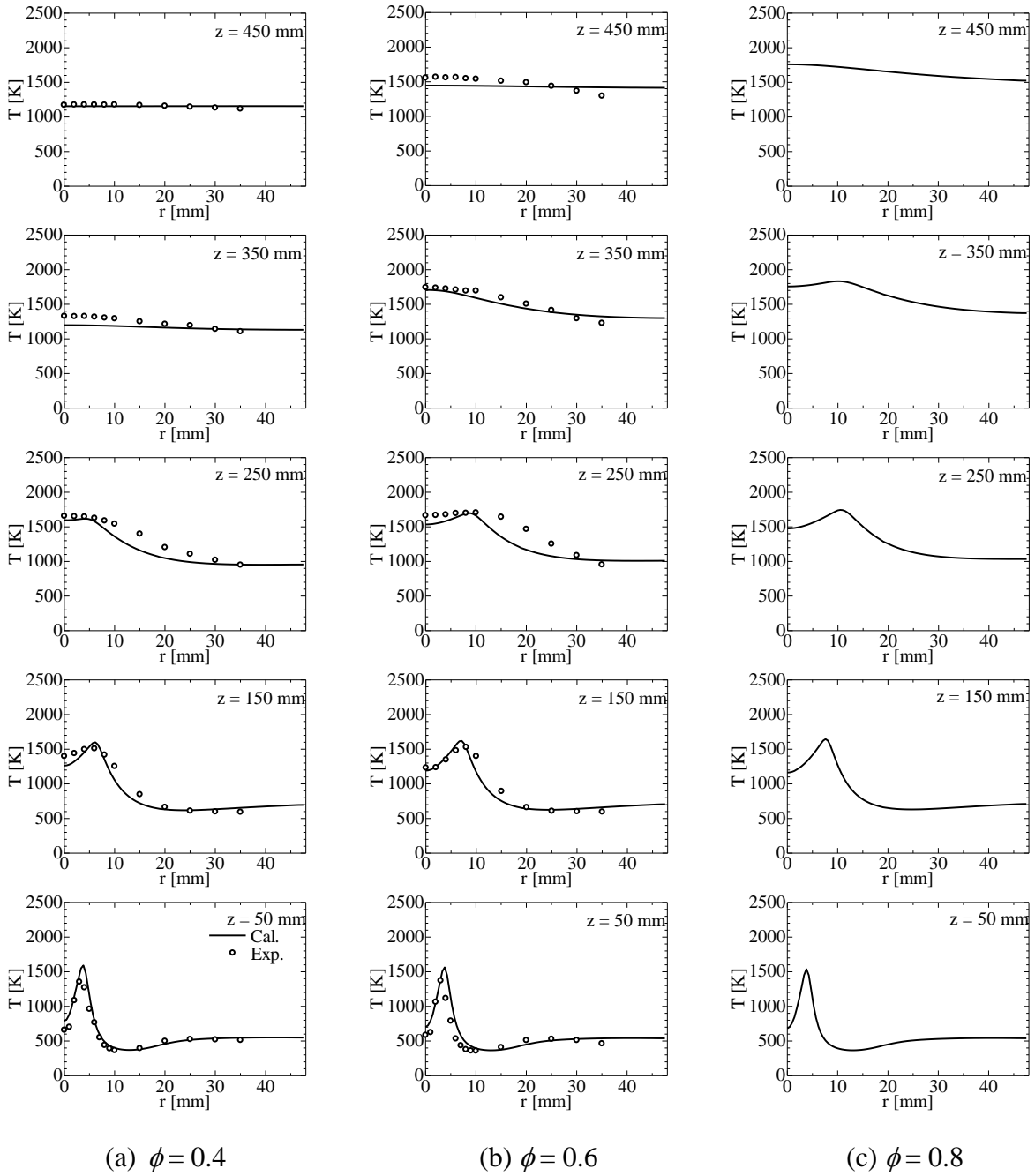
**Fig. 3.7 Radial distributions of mean temperature in terms of $\phi$**

rings of vorticity are stretched. This leads to greater scale reduction, greater dissipation, less kinetic energy and hence to lower effective viscosity. According to this argument, the effective viscosity and the spreading rate are lower in a round jet than in a plane jet. Therefore, in this

study, we tuned the constant $C_\mu$ in the $k$-$\varepsilon$ model from 0.09 to 0.05 to reduce eddy viscosity, and thereby lower the spreading rate. Thus, the spreading rate of the axisymmetric jet is significantly improved in a confined flow.

### 3.8.2  Temperature characteristics

The radial mean temperature distributions in terms of global equivalence ratio, $\phi$, from $z = 50$ mm through 450 mm are shown in Figs. 3.7 (a), (b) and (c). This study reproduces the radial temperature distributions of the experimental measurements to a considerable degree. The increase in $\phi$ corresponds to the increase of fuel flow rate, and thus, the reaction rate should be enhanced to approximately $\phi = 1$. Thereby, the maximum temperature at each axial distance is recorded in $\phi = 0.8$. The temperature distributions at an axial distance of $z = 50$ mm, in all cases of $\phi$, show the maximum value in the flame region, and temperature decreases outside the high-temperature flame region because of the airflow. However, temperature again increases outside the airflow because of burnt gases, which transported by the recirculation vortex. Moreover, flat temperature distributions in the downstream are reproduced perfectly. Figures 3.8 (a), (b) and (c) indicate the axial distributions of mean temperature in terms of $\phi$ with the experimental measurements. The predicted temperature shows a very good agreement with the measurements. As expected, the maximum axial temperature increases with $\phi$, and the maximum temperatures of $\phi = 0.4$, 0.6 and 0.8 are located near $z = 250$, 330 and 425 mm, respectively. The temperatures decrease in the downstream and become constant. The locations, where temperatures become constant, should correspond to the end of flame. This will be justified through reaction rates shown in the later section. Thus, the present model predicts the correct flame volume.

In this study, the turbulent Schmidt number is maintained at unity, whereas the turbulent Prandtl number is set to 0.7 for proper thermal dissipation. The turbulent Schmidt number describes the momentum and mass transfer interaction, whereas the turbulent Prandtl number describes the momentum and heat transfer interaction. Unlike open flames, confined flames undergo the entrainment of recirculated fluid at jet boundaries. Moreover, there exist no radial momentum and mass transfers at the furnace wall. The circumstance makes both the rates of the momentum and the mass transfers get near in turbulence. Thus, the turbulent Schmidt number is set to unity.
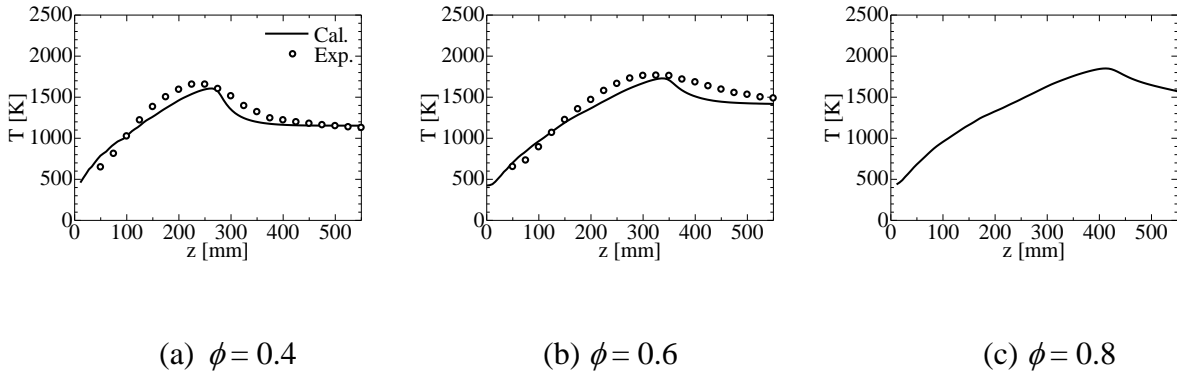
Fig. 3.8 Axial distributions of mean temperature in terms of $\phi$

On the other hand, heat is transferred through the furnace wall in the experiment. This enhances the heat transfer than other transfers. Therefore, the turbulent Prandtl number should be less than unity. Consequently, the turbulent Prandtl number is tuned and set to 0.7, and thereby the temperature predictions match those of the experimental measurements.

### 3.8.3 Species concentration characteristics

The radial distributions of mean mole fraction of CO and $O_2$ in terms of the global equivalence ratio, $\phi$, are shown in Figs. 3.9 and 3.10. The CO mole fraction increases at $z = 50$ mm sharply around the reaction region and in the downstream rapidly diffuses to the center of the flame to change the distribution to top-hat shape. The exhaustion of CO shows the complete combustion. As expected, the maximum mole fractions at each axial distance increase with the increase in $\phi$. Here, the experimental measurements at the central axis show CO of $1 \times 10^4$ ppm. This is due to the upper measurement limit of the analyzer [23]. The distributions of $O_2$ mole fraction at $z = 50$ mm show a saddle shape distribution attributable to the air supply from the air nozzles and the dilution by the burnt gases in the surrounding. The increase in $\phi$ delays the diffusion of $O_2$ towards the inside of flame because of the increase in the fuel velocity making the length of flames longer. Both the CO and $O_2$ concentrations are in fair agreement with the experiments in terms of the order.
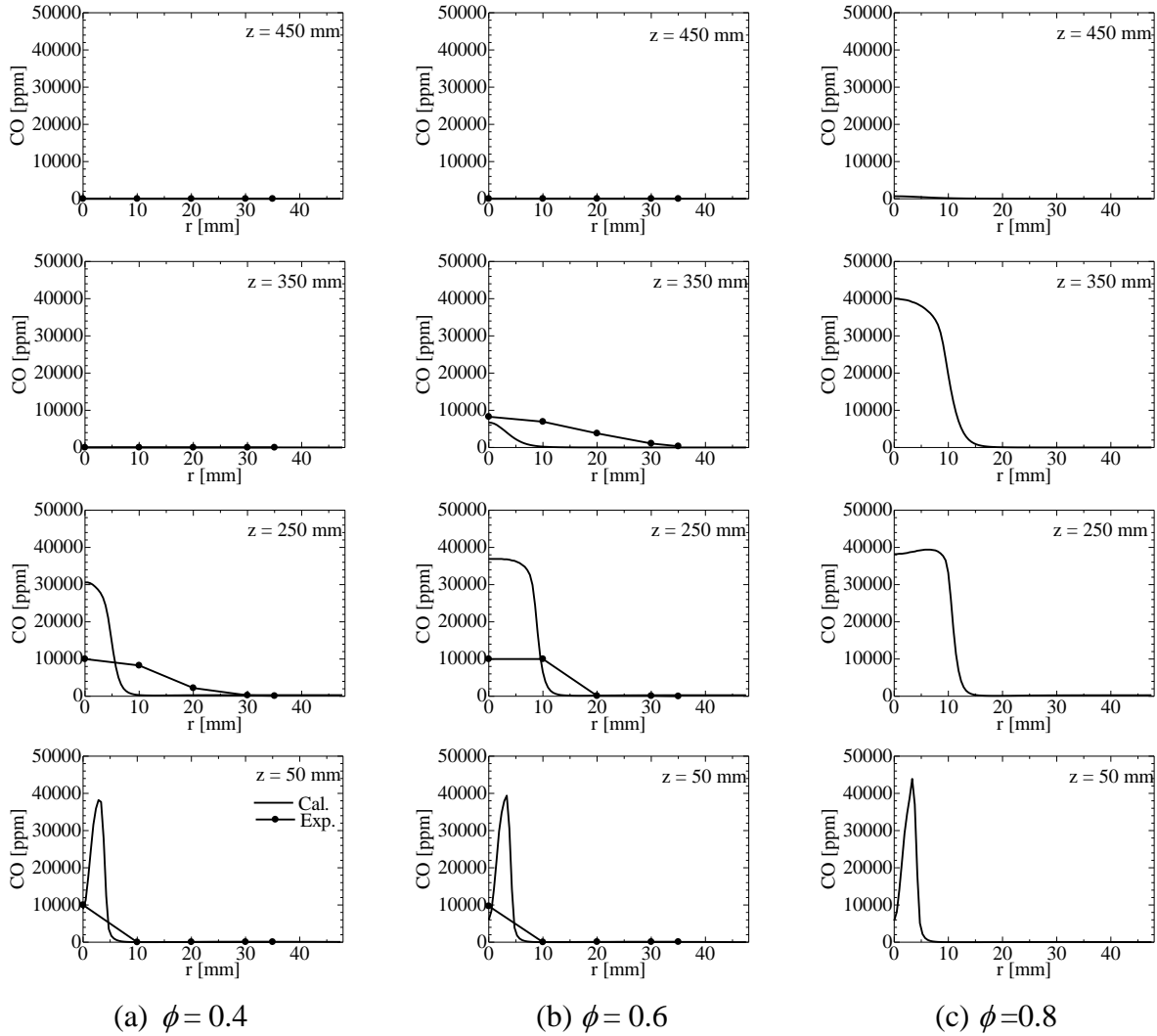
**Fig. 3.9 Radial distributions of mean CO mole fractions in terms of $\phi$**

*3.8.4   Mean reaction and mean heat-release rates*

The radical distributions of the mean reaction rates of the species $C_3H_8$, $O_2$, CO, $CO_2$, $H_2O$, and $CH_4$, and the mean heat-release rates from $z = 50$ mm through 300 mm for $\phi = 0.4$ are illustrated in Fig. 3.11. The $C_3H_8$ concentration decreases with the progress of reaction. Thereby, the $C_3H_8$ reaction rate gradually decreases with the axial distance, and disappears by $z = 200$ mm. The $O_2$ reaction rate also gradually decreases in the downstream region. CO is generated in the fuel-rich region on the center side and consumed in the fuel-lean region. The $CO_2$ reaction rate increases
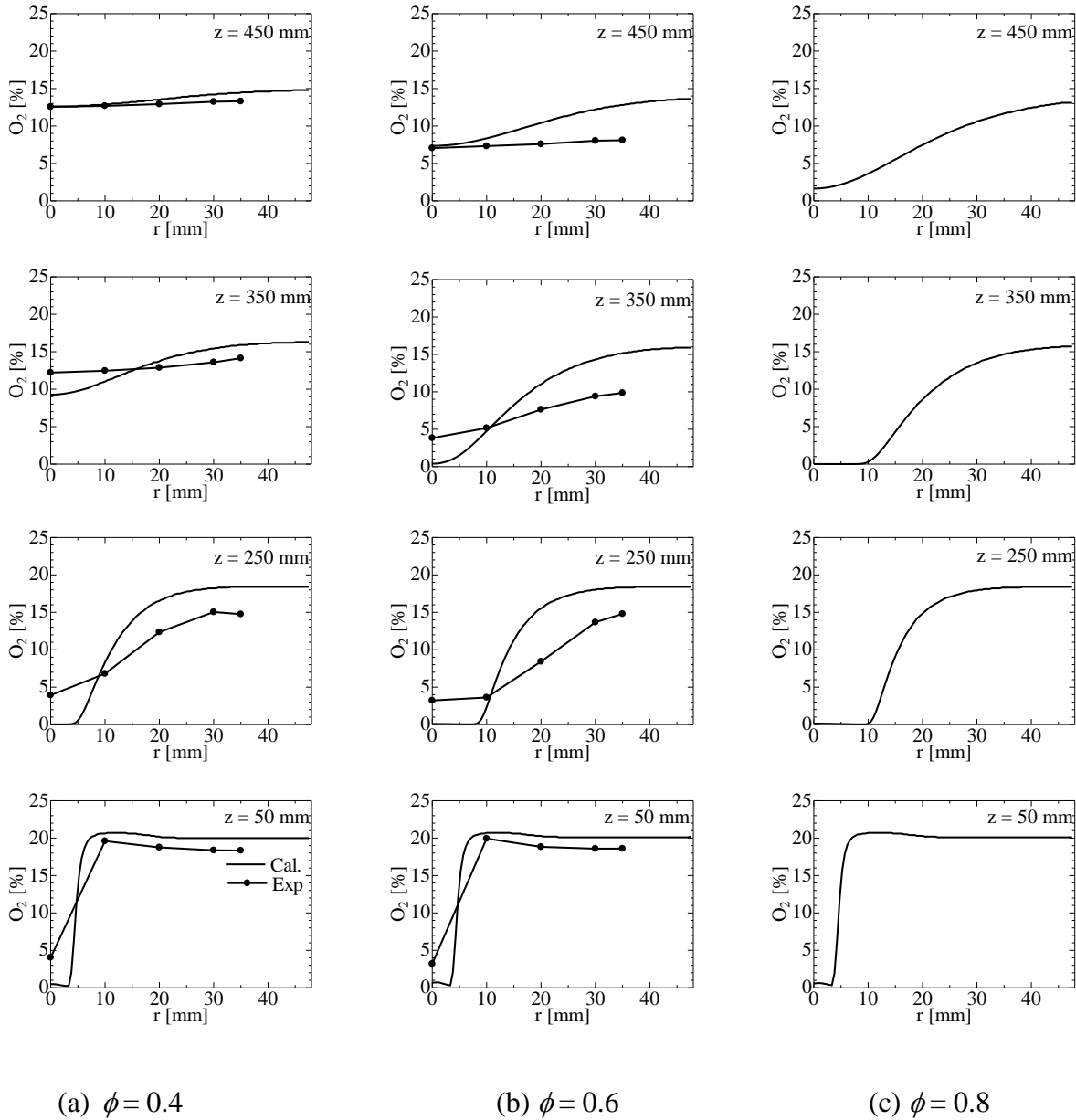
**Fig. 3.10 Radial distributions of mean $O_2$ mole fractions in terms of $\phi$**

in the lean region corresponding to the consumption of CO. Moreover, the intermediate species of $CH_4$ is generated in the rich region and decomposed to final products in the lean region.

The global reaction rate of propane-air oxidation quantitatively should correspond to the mean heat-release rate. For $\phi = 0.4$, the mean heat-release rate increases up to the axial distance of $z =$

52
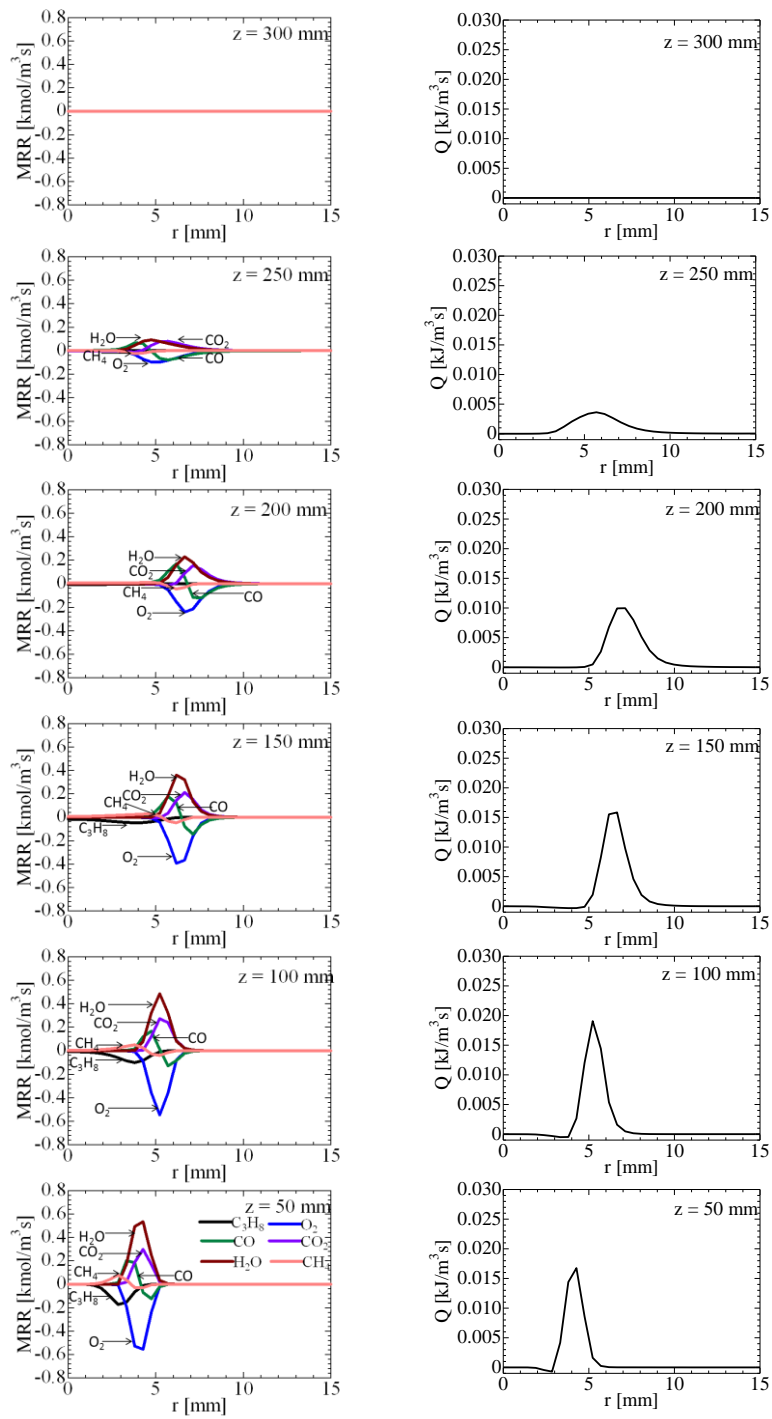
(a) Mean reaction rate (MRR)    (b) Mean heat-release rate (Q)

**Fig. 3.11 Radial distributions of mean reaction and mean heat-release rates for $\phi = 0.4$**

100 mm, and then decreases in the downstream region. Every reaction is completed by approximately $z = 300$ mm for $\phi = 0.4$. These results verify the temperature features for $\phi = 0.4$ in Figs. 3.7 and 3.8. The heat release region expands gradually in the radial direction with the axial distance because of the turbulence. Turbulence enhances convection and diffusion of heat and mass in the flame. Therefore, turbulence expands the mean-reaction zone in the radial direction with the axial distance, and thereby mean heat-release region



(a) $\phi = 0.4$        (b) $\phi = 0.6$        (c) $\phi = 0.8$
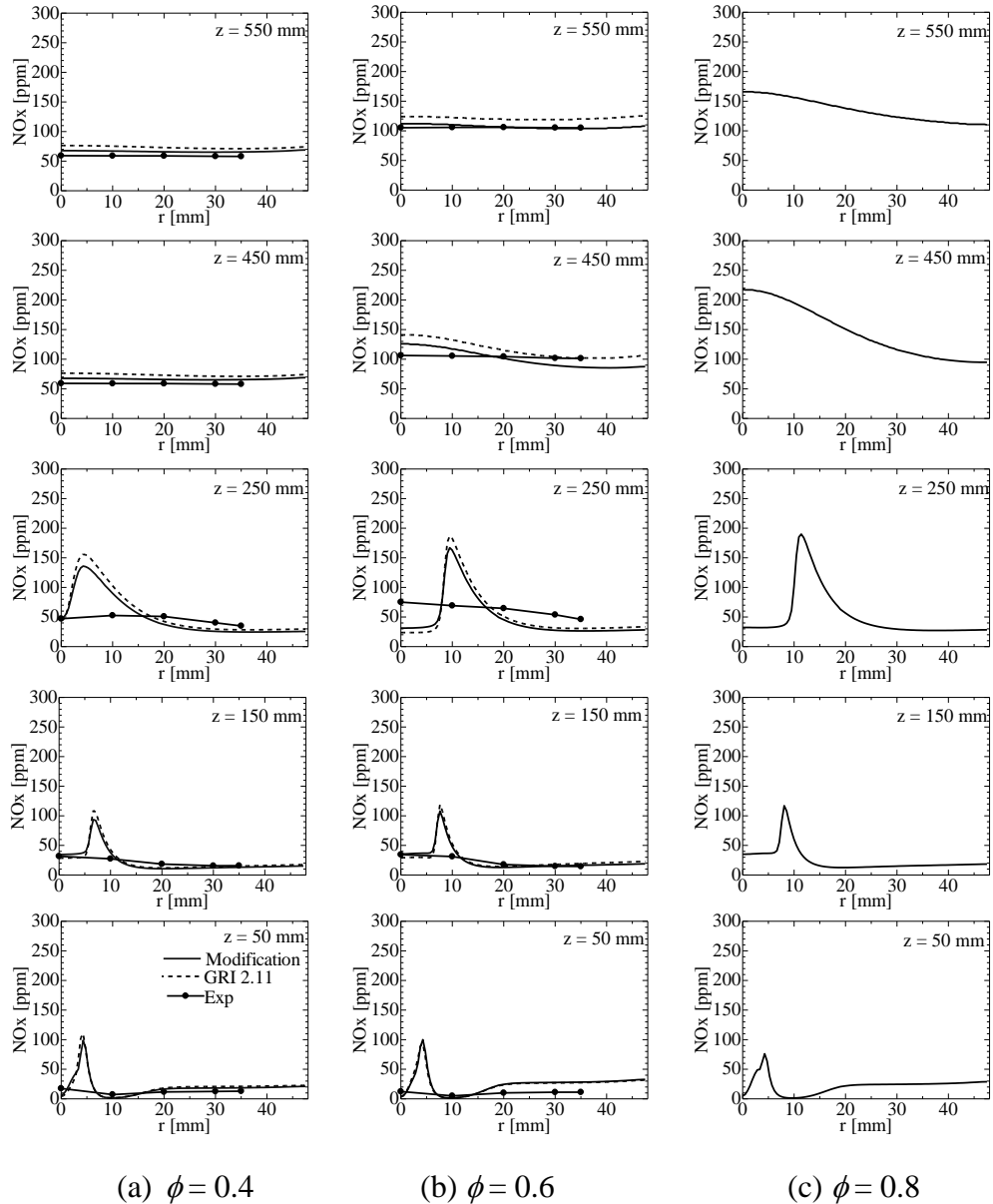
**Fig. 3.12 Radial distribution of NOx emission in terms of $\phi$**

### 3.8.5 NOx Emission

Figures 3.12 (a), (b), and (c) show the NOx emission distributions from $z = 50$ mm through $z = 550$ mm with the experimental measurements in terms of global equivalence ratio, $\phi$. The NOx emission is the summation of NO, $N_2O$, and $NO_2$ emissions, as described in 3.6. The NOx emission was estimated at first with GRI 2.11 NOx mechanism [39]. The results show a good agreement with the measurements in terms of order, as shown in Fig. 3.12. However, the NOx concentrations are underestimated near the central axis of the upstream region ($z = 50$ mm of $\phi = 0.4$ and 0.6, and $z = 250$ mm of $\phi = 0.6$) and overestimated in the downstream region. The same phenomenon resulted in the study of Frassoldati et al. [50]. This is attributable to the delay of the NOx reaction. Therefore, some modification is needed to overcome the delay of NOx reaction. The main routes of the prompt formation of NOx are HCN $\rightarrow$ HOCN $\rightarrow$ HNCO $\rightarrow$ $NH_2$ $\rightarrow$ NH $\rightarrow$ HNO $\rightarrow$ NO and HCN $\rightarrow$ NCO $\rightarrow$ NH $\rightarrow$ HNO $\rightarrow$ NO, respectively, as described in 3.6. A possible cause of the delay is related to reactions of $NH_3$. The reactions consist of the following three steps:

$$NH_3 + H \Longleftrightarrow NH_2 + H_2 \qquad\qquad\qquad\qquad (R\ 277)$$

$$NH_3 + OH \Longleftrightarrow NH_2 + H_2O \qquad\qquad\qquad\qquad (R\ 278)$$

$$NH_3 + O \Longleftrightarrow NH_2 + OH \qquad\qquad\qquad\qquad (R\ 279)$$
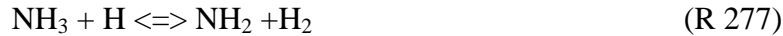
As shown in Fig. 3.13 (concentration of $NH_3$ and $NH_2$ for $\phi = 0.6$), $NH_3$ was resulted significantly higher concentration near the central axis of the upstream region than $NH_2$ with GRI 2.11. Moreover, in the downstream region, $NH_3$ and $NH_2$ concentrations were disappeared with GRI 2.11, as shown in Fig. 3.13. This means that $NH_3$ again forms $NH_2$, and $NH_2$ proceeds to NO in the downstream region. However, $NH_2$ concentration was significantly increased near the central axis of the upstream region without R277-R279 in GRI 2.11, as shown in Fig. 3.13 (blue solid lines). This modification verifies clearly that the $NH_3$ reactions depress the concentration of $NH_2$, and thereby NO formation in the upstream region. Thus, NOx was re-evaluated under the modification. The results are shown by solid lines in Fig. 3.12. The modification improves slightly the NOx estimation, but completely evaluates the measurements in the downstream. We
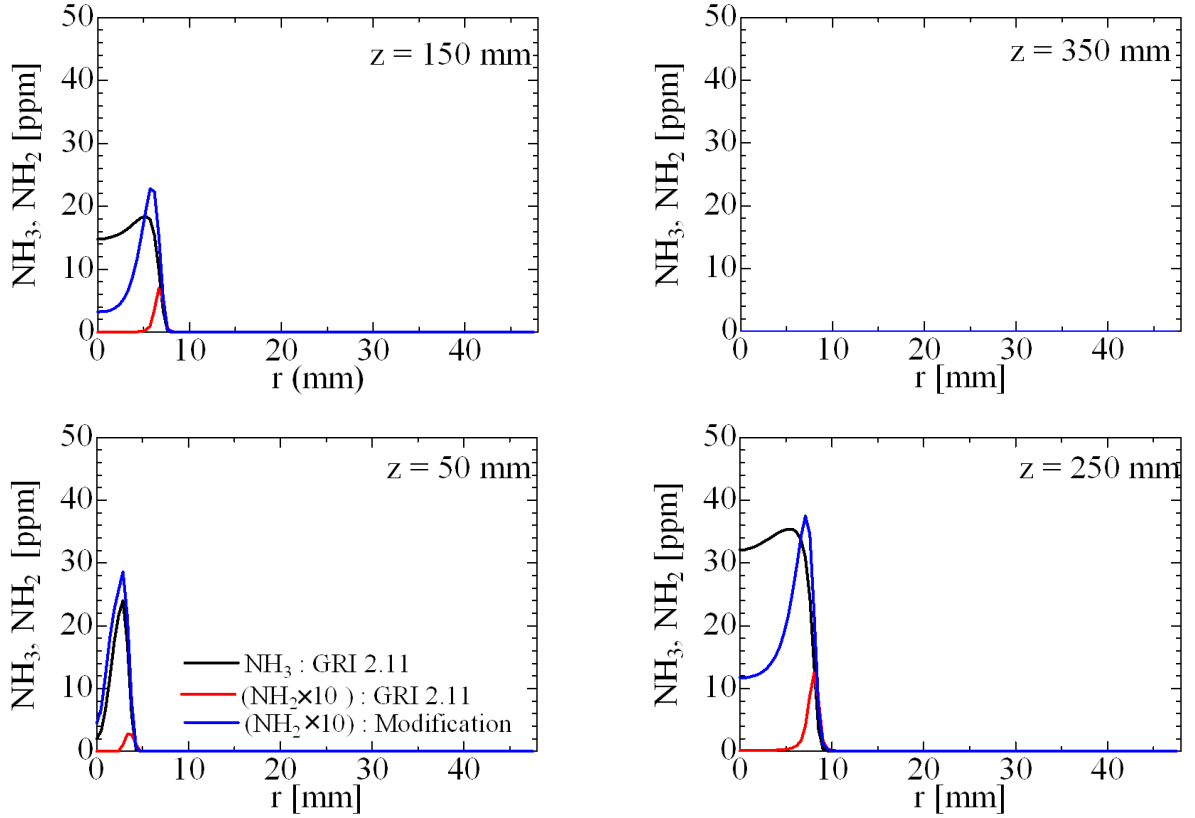
**Fig. 3.13 Radial distributions of mean $NH_3$ and $NH_2$ mole fractions for $\phi = 0.6$**

believe that the improvement leads the accurate estimation of the emission index of NOx, because the index is evaluated at the furnace exit.

### 3.8.6 Emission index of NOx (EINOx)

The evaluation of NOx emission is given in terms of the emission index of NOx, EINOx, which is defined as the total grams of NOx produced to fuel 1kg burnt. The value is obtained by dividing the net NOx mass flow rate at the furnace exit by net fuel feeding mass flow rate, $M_f$.

$$EINOx \,[\text{g/kg fuel}] = \frac{\int_0^{R_{Exit}} \overline{\rho} \tilde{Y}_{NOx} \tilde{U}_z \, 2\pi r dr \times 1000}{M_f} \tag{3.44}$$

where $R_{Exit}$ is the radius of the furnace exit.
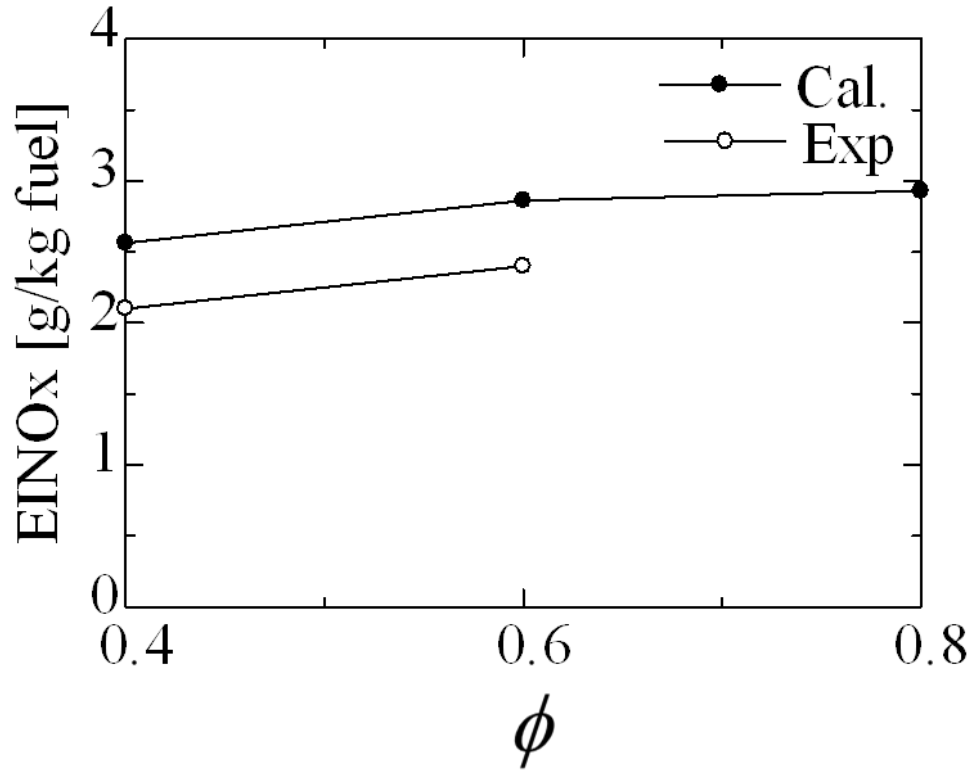
**Fig. 3.14 EINOx in terms of $\phi$**

Figure 3.14 shows EINOx predictions in terms of $\phi$ with the experimental measurements, which the predictions are based on the above modification of NOx mechanism. The EINOx shows a good agreement with the measurements in terms of the order. The EINOx increases with $\phi$. The increase in $\phi$ increases the furnace temperature significantly in small cylindrical furnaces, thereby the EINOx is increased through the enhancement of the thermal NOx reaction. However, this tendency should be limited to the case of furnace inner diameter of 95mm. If we investigate cases of larger inner diameters conducted experimentally, as shown in Fig. 2.5 (b), the increase in $\phi$ must strengthen the recirculation vortices and the dilution, and finally decrease the NOx emission.

### 3.9    Conclusions

The PaSR combustion model has been incorporated into the OpenFOAM CFD tool to investigate turbulent flow fields, temperature, species concentration, and NOx emissions of confined

turbulent propane non-premixed jet flames, in terms of the global equivalence ratio, $\phi$. The predicted mean axial velocities and mean temperature show an excellent agreement with the experimental measurements. The axial distributions of mean temperature excellently predict the flame length. The mean mole fraction predictions of CO and $O_2$ show a reasonable agreement with the experimental measurements. The mean reaction and the mean heat-release rates verify the features of temperature and mole fractions of species. The NOx emission predictions with GRI 2.11 NOx mechanism show a reasonable agreement with experimental data in terms of the order, but higher $NH_3$ formation in the upstream depresses the NOx formation reactions. Thus, reactions related to $NH_3$ were removed from GRI 2.11. The modification has improved the EINOx predictions. The increase in $\phi$ enhances the reaction for the case of an inner diameter of 95 mm. Consequently, the EINOx increases with $\phi$. Finally, this study has verified that the present numerical method with the PaSR model is very useful for the evaluation of confined turbulent non-premixed flames.

# CHAPTER 4

# NUMERICAL INVESTIGATION OF THE EFFECT OF SELF-DILUTION CHARACTERISTICS IN CONFINED FLAMES ON $NO_X$ ABATEMENT

## 4.1    Introduction

This chapter describes a numerical evaluation to characterize the effect of self-dilution in confined flames, in terms of the furnace geometry and the global equivalence ratio on NOx emission properties. In confined flames, the recirculation vortex, which is generated between the flame and the furnace wall, as shown in Fig.3.6, leads to self-dilution of the combustion mixture. Therefore, the enhancement in self-dilution should lead to the peak temperature reduction in the furnace, and thereby, considerable thermal NOx abatement. In this chapter, the recirculation boosting techniques have been numerically studied, and the flame dilution quantitatively evaluated.   Consequently, this study found that the increase of dilution factor as a dominant parameter, which controls the characteristics of confined flames, is very important for NOx abatement.

## 4.2    Numerical models and conditions

In this study also, the flow calculation software OpenFOAM [48] is employed as a finite-volume solver for Reynolds-Averaged Navier Stokes (RANS) equations, and the $k-\omega$ SST model [51], as described in Section 4.2.1, is used to model the turbulent flux terms in RANS equations of continuity, momentum, species mass fraction, and sensible enthalpy. The turbulence-chemistry interaction is accounted for with the partially-stirred-reactor combustion model [31]. Djavdan et al. [34] proposed and validated an augmented reduced kinetic mechanism for the propane–air combustion, which includes 28-species and 69-elementary steps, was selected as the chemical kinetics of propane-air oxidation, and coupled with the NOx formation mechanism, which is extracted from GRI 2.11 [39]. An *in-situ* adaptive tabulation algorithm library [37] is used to calculate the composition changes through chemical reactions, and thereby to reduce the computational burden. Furnaces consist of cylindrical combustion chambers, which are installed vertically, and a burner is installed at the center of the bottom of the combustion chamber [20].

The chambers have inner diameters of 95 mm and 182 mm and a height of 840 mm. More details of the geometries can be found in Section 2.2. In addition, the nozzle inlet is located 50 mm upstream from the nozzle exit in order to ensure a fully-developed turbulent flow profile at the nozzle exit. The origin of the coordinates was set at the center of the fuel nozzle exit, as usual, and the axial and radial coordinates are indicated by $z$ and $r$, respectively. This numerical simulation was also performed in the three-dimensional grids using the periodic boundary condition. The geometry is specified as a wedge of small angle ($<5^0$), and one cell thickness is running along the plane of symmetry, as shown in Fig. 3.4(c). The calculation grids were concentrated at the flame region, and the smallest grid size was 0.2 mm. Propane was used as the main-fuel, whereas hydrogen was used as the pilot-fuel. The global equivalence ratios were 0.4 and 0.6, and the fuel inlet-velocities were shown in Table 1-1, in terms of the global equivalence ratio, $\phi$. The total airflow rate was fixed at 0.002 m$^3$/s. Thus, $\phi$ was determined through the fuel flow rate. In this study also, the high and low air velocities of two air annular nozzles were 9.8 m/s and 1.8 m/s, respectively. The turbulent Schmidt number was set as one, whereas turbulent Prandtl number was 0.7, as described in Section 3.8.2. The initial simulation conditions are almost similar to the study in Section 3.7. A turbulence intensity of 10 % was set for both fuel and air-inlet flows. The furnace walls were non-slip and adiabatic, and the outlet was specified by the continuity boundary condition. The initial CFD time-step was selected as $1\times 10^{-6}$ s with a corresponding Courant number of approximately 0.4, whereas the initial chemical time-step was selected as $1\times 10^{-7}$ s. Numerical results have been compared with experimental measurements.

### 4.2.1  $k$-$\omega$ SST turbulence model

The new two-equation eddy-viscosity turbulence model combines different elements of existing models that are considered superior to their alternatives. The model utilizes the original $k$-$\omega$ model of Wilcox [52] in the inner region of the boundary layer and switches to the standard $k$-$\varepsilon$ model in the outer region and in free shear flows. It has a performance similar to the Wilcox model, but avoids that model's strong free stream sensitivity. In addition, the model modifies the definition of the eddy-viscosity, and the modification leads to accounting the effect of the transport of the principal turbulent shear stress.

$k$ -Equation:

$$\frac{\partial(\overline{\rho}\tilde{k})}{\partial t} = \underset{=}{\tilde{s}}.\nabla\tilde{U} - \beta^*\overline{\rho}\tilde{\omega}\tilde{k} + \nabla.\left[(\mu + \sigma_k\mu_t)\nabla\tilde{k}\right]$$  (4.1)

$\omega$ -Equation

$$\frac{\partial(\overline{\rho}\tilde{\omega})}{\partial t} = \frac{\gamma}{\nu_t}\underset{=}{\tilde{s}}.\nabla\tilde{U} - \beta^*\overline{\rho}\tilde{\omega}^2 + \nabla.\left[(\mu + \sigma_\omega\mu_t)\nabla\tilde{\omega}\right]$$

$$+ 2(1 - F_1)\rho\sigma_{\omega 2}\frac{1}{\tilde{\omega}}\nabla\tilde{k}\nabla\tilde{\omega}$$  (4.2)

The constants $\phi$ of the new model are calculated from the constants, from the $\phi_1$ and $\phi_2$, as follows:

$$\phi = F_1\phi_1 + (1 - F_1)\phi_2$$  (4.3)

The constants of set 1 ($\phi_1$) are:

$\sigma_{k1} = 0.85$, $\sigma_{\omega 1} = 0.5$, $\beta_1 = 0.0750$, $\beta^* = 0.09$, $K = 0.41$, $\gamma_1 = \beta_1/\beta^*$- $\sigma_{\omega 1}K^2/(\beta^*)^{1/2}$

The constants of set 1 ($\phi_2$) are:

$\sigma_{k2} = 1.00$, $\sigma_{\omega 1} = 0.856$, $\beta_2 = 0.0828$, $\beta^* = 0.09$, $K = 0.41$, $\gamma_2 = \beta_2/\beta^*$- $\sigma_{\omega 2}K^2/(\beta^*)^{1/2}$

$$F_1 = \tanh(\arg_1^4)$$  (4.4)

$$\arg_1 = \min\left[\max\left(\frac{\sqrt{k}}{0.09\omega y};\frac{500\nu}{y^2\omega}\right);\frac{4\rho\sigma_{\omega 2}k}{CD_{k\omega}y^2}\right]$$  (4.5)

where $y$ is the distance to the next surface and $CD_{k\omega}$ is the positive portion of the cross-diffusion term of Eq. 4.2

$$CD_{k\omega} = \max\left[2\rho\sigma_{\omega 2}\frac{1}{\omega}\nabla k\nabla\omega;10^{-20}\right]$$  (4.6)

The term $\arg_1$ obviously goes to the zero far enough away from solid surfaces because of the $1/y$ or $1/y^2$ dependency in all three terms in Eq. 4.5. Inside a boundary layer the three arguments in Eq. 4.5 have the following purpose; the first argument is the turbulent length scale divided by $y$.

It is equal to 2.5 in the log layer and goes to zero towards the boundary layer edge. The second argument ensures that $F_1$ is equal to one in the sub-layer. (Note that $\omega$ goes like $1/y^2$ in the near wall region and is proportional to $1/y$ in the log region, so that $1/(\omega y^2)$ is constant near the surface and goes to zero in the log region.) The third argument is an additional safeguard against the free-stream dependent solution. It can be shown that the last argument ensures that $\arg_1$ goes to zero near the boundary layer edge. As $\arg_1$ goes to zero near the boundary layer edge, so does $F_1$ so that the standard $k$-$\varepsilon$ is used in that region.

The eddy viscosity is defined as;

$$v_t = \frac{a_1 k}{\max(a_1 \omega; \Omega F_2)} \; ; \; a_1 = 0.31 \tag{4.7}$$

where $\Omega$ is the absolute value of the vorticity. $F_2$ is given by;

$$F_2 = \tanh(\arg_2 2) \tag{4.8}$$

$$\arg_2 = \max\left( 2\frac{\sqrt{k}}{0.09 \omega y} ; \frac{500 v}{y^2 \omega} \right) \tag{4.9}$$

However, this model also overpredicts the decay rate and the spreading rate of a round jet flow. As discussed in the chapter 3, Pope [49] has suggested that, in a round jet flow, the stretching of turbulent vortex tubes by the mean flow has a significant influence on the process of scale reduction. As the jet spreads, rings of vorticity are stretched. This leads to greater scale reduction, greater dissipation, less kinetic energy and hence to lower effective viscosity. According to this argument, the effective viscosity and the spreading rate are lower in a round jet than in a plane jet. Therefore, in this study also, we tuned the constant $a_1$ from 0.31 to 0.12 to reduce eddy viscosity, and thereby lower the spreading rate. Thus, the spreading rate of the axisymmetric jet is significantly improved in a confined flow with good predictions of mean temperatures.

## 4.3 Results and discussion

### 4.3.1 Temperature characteristics



(a) $\phi = 0.4$        (b) $\phi = 0.6$
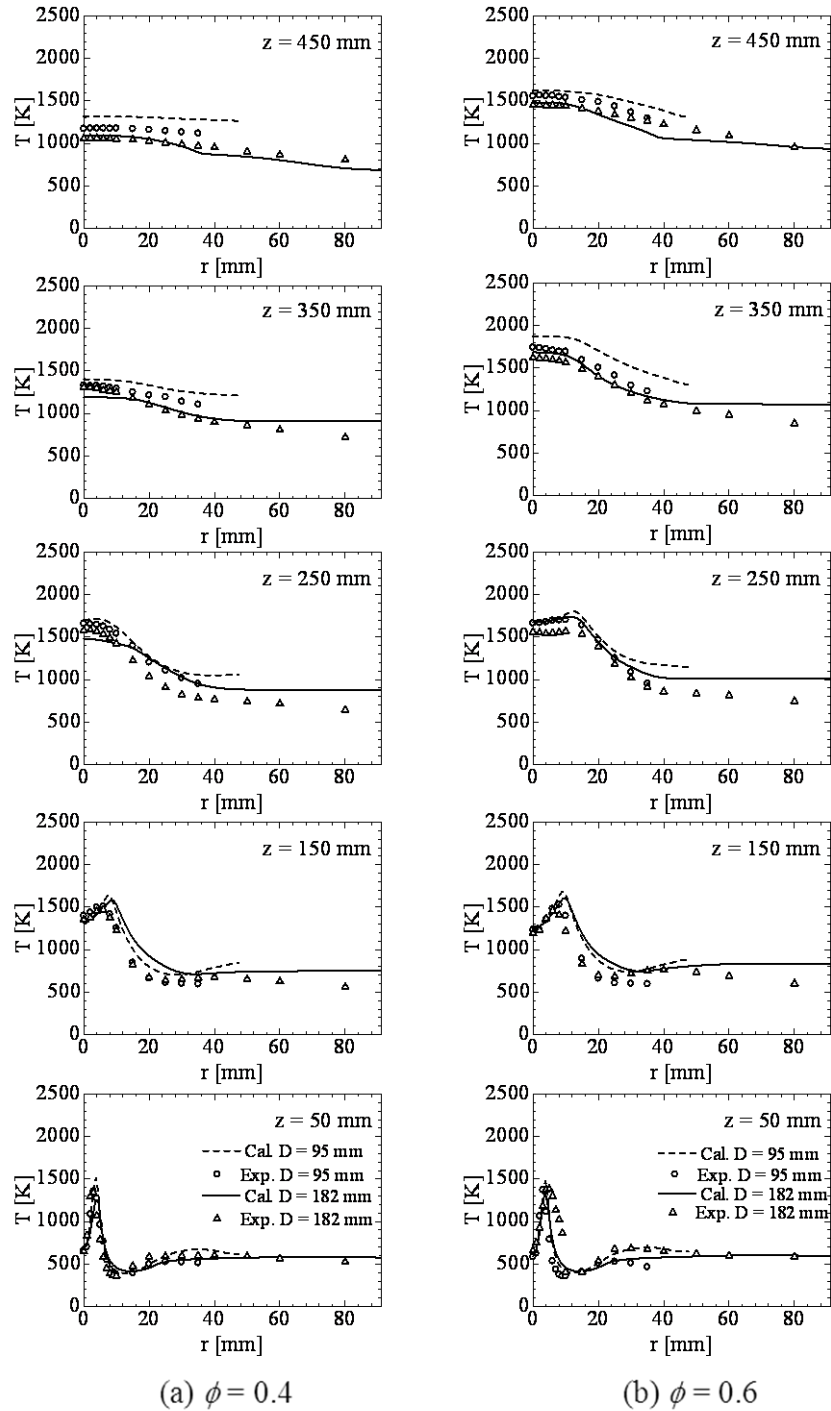
**Fig. 4.1 Radial distributions of mean temperature in terms of $D$ and $\phi$, for $\Delta U_a = 8$ m/s**

(a) $\phi = 0.4$         (b) $\phi = 0.6$
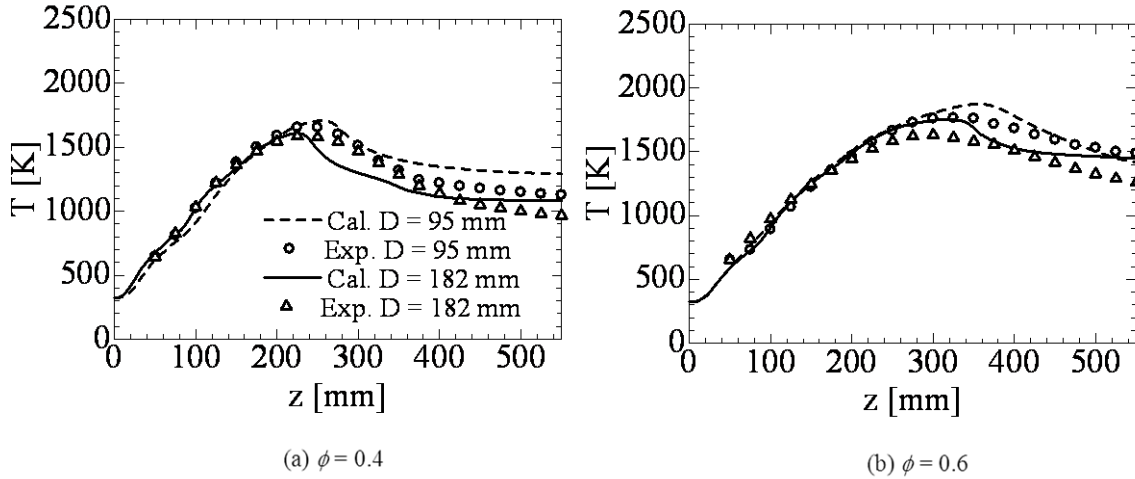
**Fig. 4.2 Axial distributions of mean temperature in terms of $D$ and $\phi$, for $\Delta U_a = 8$ m/s**

Figures 4.1 and 4.2 show the radial and axial mean temperature distributions, respectively, in terms of the inner diameter, $D$, and the global equivalence ratio, $\phi$, for the air velocity difference, $\Delta U_a$ of 8 m/s, from z = 50 mm through 450 mm. The study reproduces the experimentally obtained temperature distributions to a considerable degree of accuracy. The increase in $\phi$ is related to the increase in the fuel flow rate, and so the reaction rate should be enhanced. Consequently, the flame temperature increases at $\phi = 0.6$, as shown in Fig. 4.2. However, the increase in $D$ decreases the maximum temperature in the flame region. This should be caused by the strong dilution through the strengthened burnt gases entrainment to the flame in the larger cylindrical furnace. The increase in dilution increases the heat capacity of the combustion mixture and leads to a decrease in the flame temperature.

### 4.3.2 Flow field

The flame characteristics of confined flames should be strongly affected by dilution process through the recirculation vortices. Therefore, a quantitative evaluation is essential to express the dilution level. The radial distributions of mean axial velocity ($U_z$) from z = 25 mm through 200 mm in terms of $D$, for $\phi = 0.4$ and $\Delta U_a = 8$ m/s, are shown together with experimental measurements in Fig. 4.3. Negative velocities, near the furnace wall in Fig. 4.3, clearly indicate the existence of recirculation vortices. In flow regions, in which maximum velocity near the fuel nozzle (z = 25 mm, 50 mm), is approximately the same, irrespective of inner diameter. However,
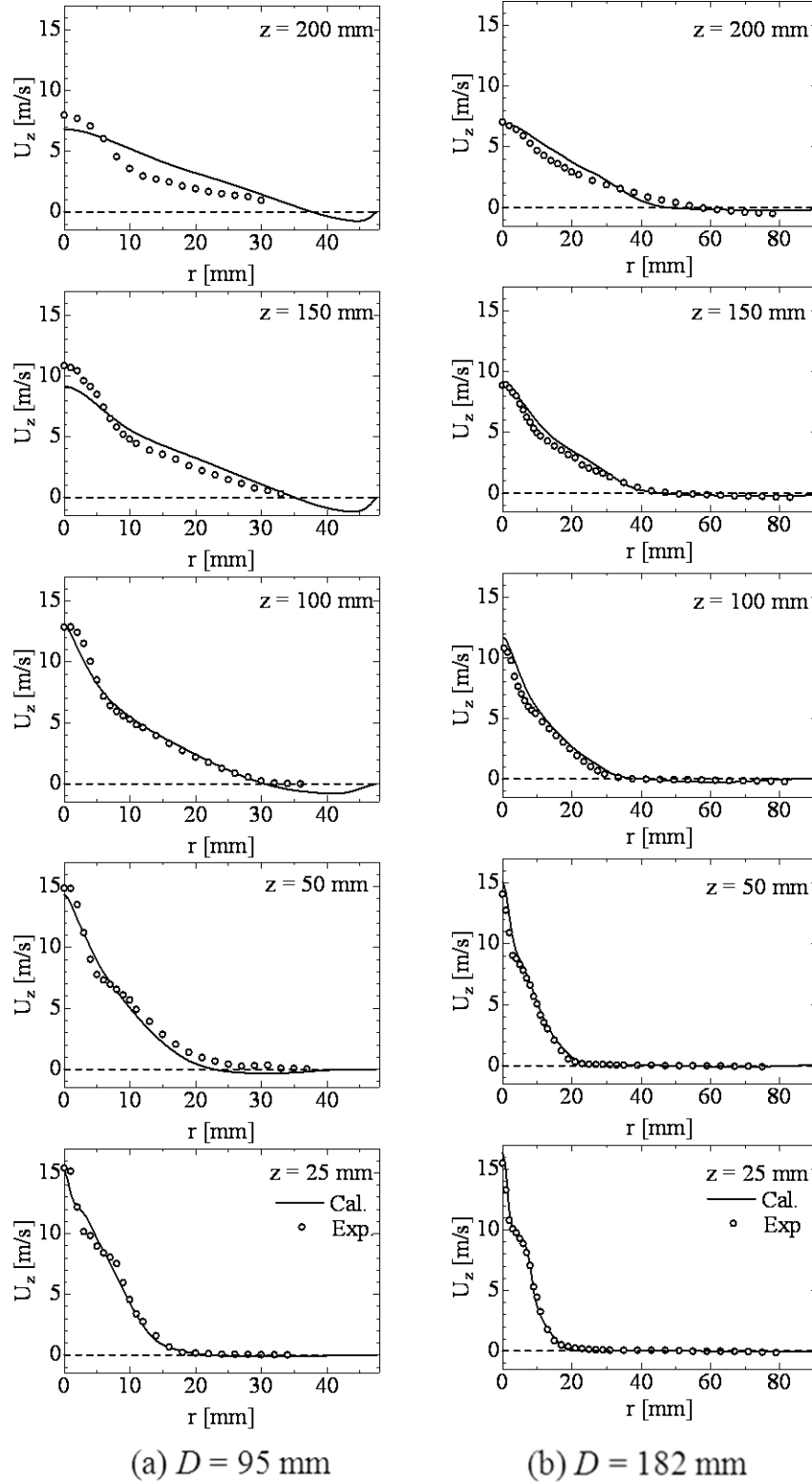
**Fig. 4.3 Radial distributions of mean axial velocity in terms of $D$ for $\phi = 0.4$ and $\Delta U_a = 8$ m/s**

(a)  $D = 95$ mm                          (b) $D = 182$ mm
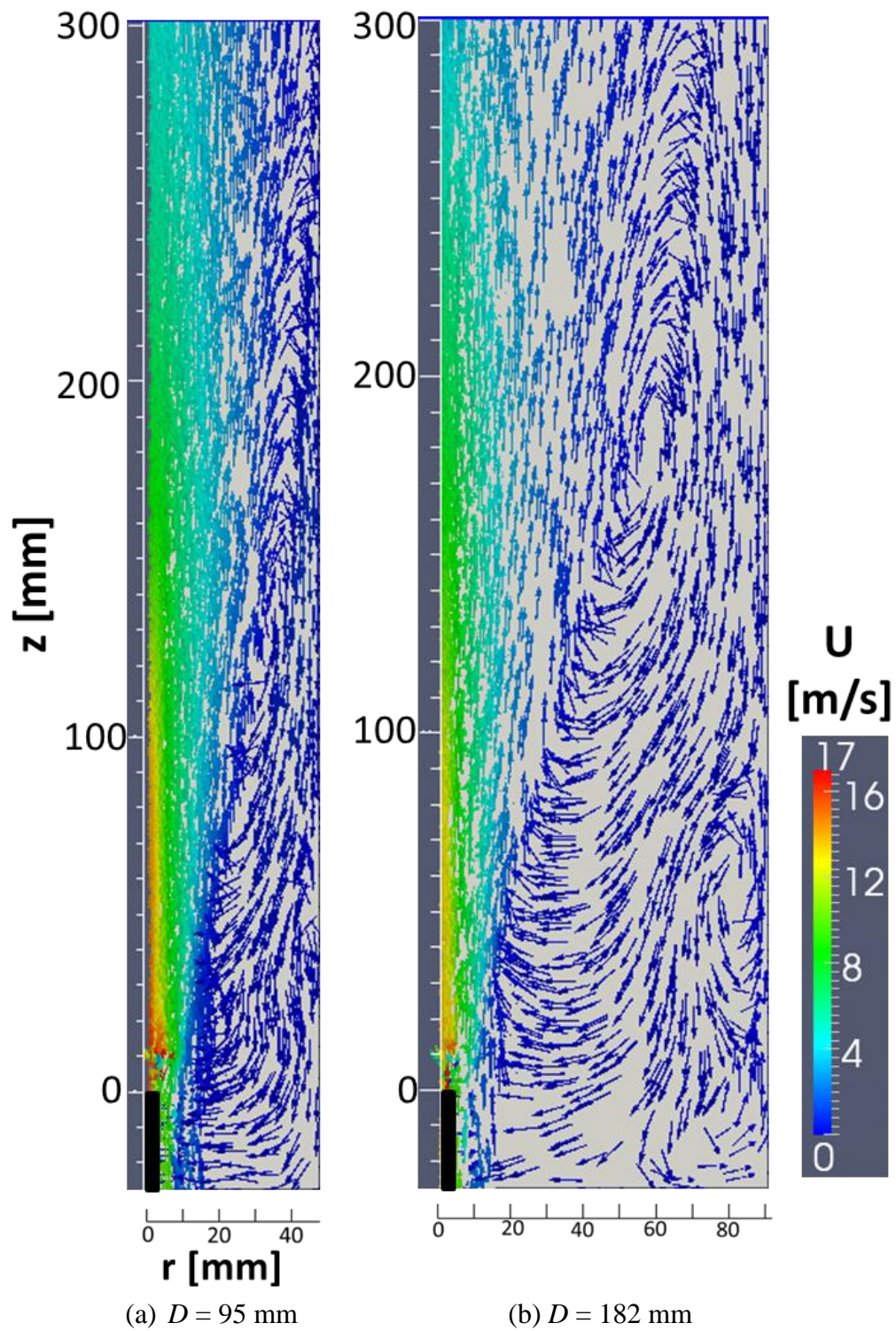
**Fig. 4.4 Vector maps of flow fields in combustion chambers in terms of $D$, for $\phi = 0.4$ and $\Delta U_{\mathrm{a}} = 8$ m/s**

the increase in the inner diameter enhances the mixing, spreading the $U_z$ distribution faster and decreasing the velocity in the center region, at around z = 100 mm in $D$ = 182 mm. Nonetheless, in downstream of $D$ = 182 mm (z = 200 mm), the maximum velocity again increases to a higher value corresponding to $D$ = 95 mm because of the strong burnt gas entrainment. Figure 4.4 shows the vector maps of flow fields in the combustion chamber up to z = 300 mm in terms of $D$ for $\phi$ = 0.4 and $\Delta U_a$ = 8 m/s and reveals a vortex, which has been generated between the jet and the wall. The arrows indicating the vectors are not to scale, and the colored bar indicates the magnitude of the velocity vector. The vector maps illustrated that, in the case of $D$ = 95 mm, the recirculation vortex is limited to z = 270 mm. On the other hand, in the case of $D$ = 182 mm, the recirculation extends beyond z = 300 mm. The recirculation vortex cores for $D$ = 95 and 182 mm are located at axial distances of z = 130 and 180 mm, respectively. This means that the recirculation vortex becomes larger with the increase in the inner diameter. Moreover, in the case of $D$ = 182 mm, there are small recirculation vortices around the corners of the cylinder in addition to the main recirculation vortex. This phenomena is not shown in $D$ = 95 mm. Thus, in the case $D$ = 182 mm, flow patterns should be more complex than $D$ = 95 mm, and it may lead to the strong burnt gas mixing with reactants.

### 4.3.3   Entrainment characteristics

Next, the recirculation flow characteristics are discussed by examining the jet zone. In order to facilitate the discussion, a parameter, $M_z$, which represents the mass flow rate of jet zone, is introduced:

$$M_z = \int_0^R 2\pi r \bar{\rho} \tilde{U}_z dr \tag{4.10}$$

where $R$ is the maximum radius of the jet zone at each cross section, and $\rho$ is the density of the combustion mixture. Figure 4.5 shows the variation of $M_z$ along the axial direction in terms of $D$ and $\phi$ ,for $\Delta U_a$ = 8 m/s. The value of $M_z$ increases in the upstream of the recirculation vortex because of the entrainment process, and decreases in the downstream of the vortex because of the discharge of gases from the jet zone to the recirculation zone. Therefore, the peak is located on the cross section of the core of the recirculation vortex. In addition, Fig. 4.5 shows that the

increase in $D$ significantly enhances the entrainment process and increases the peak value of $M_z$ because of large recirculation structure. However, the effect of fuel velocity, which is related to the global equivalence ratio, on the entrainment is minimal compared to the effect of the inner diameter. The entrainment factor defined in Eq. (4.11) characterizes the entrained mass quantity with respect to the jet zone mass flow rate, $M_z$.

$$\text{Entrainmen t Factor} = \frac{M_z - M_0}{M_z} \times 100 \tag{4.11}$$

where $M_0$ denotes the jet zone mass flow rate at z = 0 mm. The variation of entrainment characteristics are shown in Fig. 4.6 in terms of $D$ and $\phi$ for $\Delta U_a$ = 8 m/s. In the case of $D$ = 95 mm, the maximum entrainment factor is 30%, whereas, in $D$ = 182 mm, the maximum factor is about 45%, irrespective of the global equivalence ratio, $\phi$. The enhancement of entrainment should lead to greater dilution of the flame.
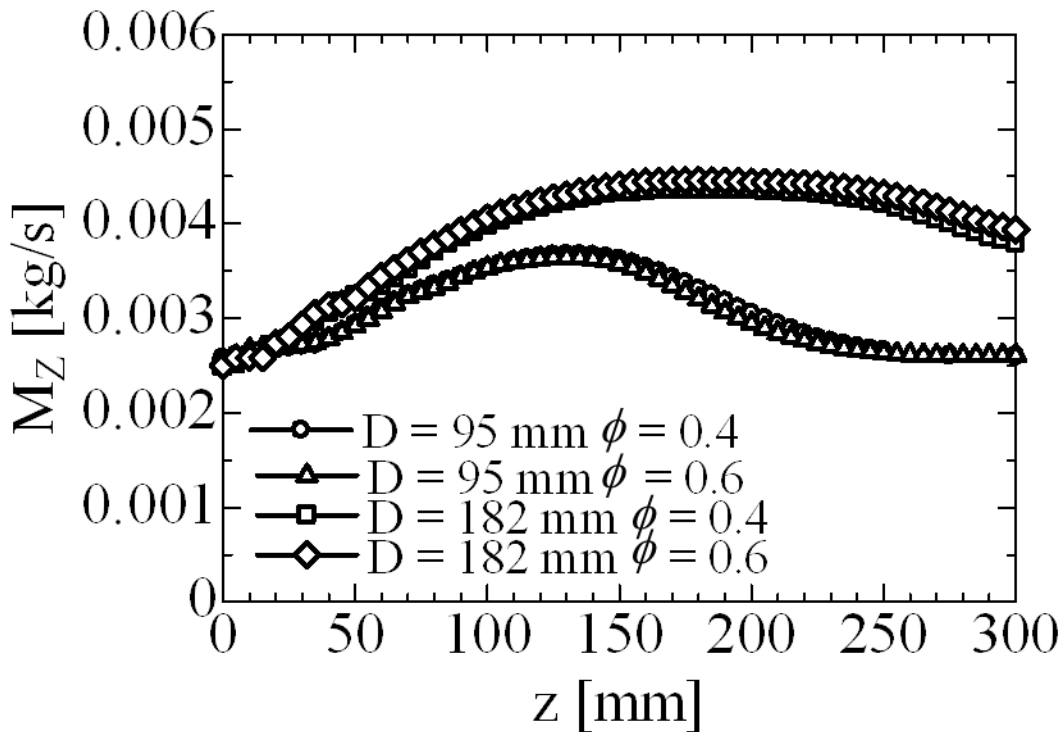


**Fig. 4.5 Jet zone mass flow rate, $Mz$, in terms of $D$ and $\phi$ for $\Delta Ua$ = 8 m/s**
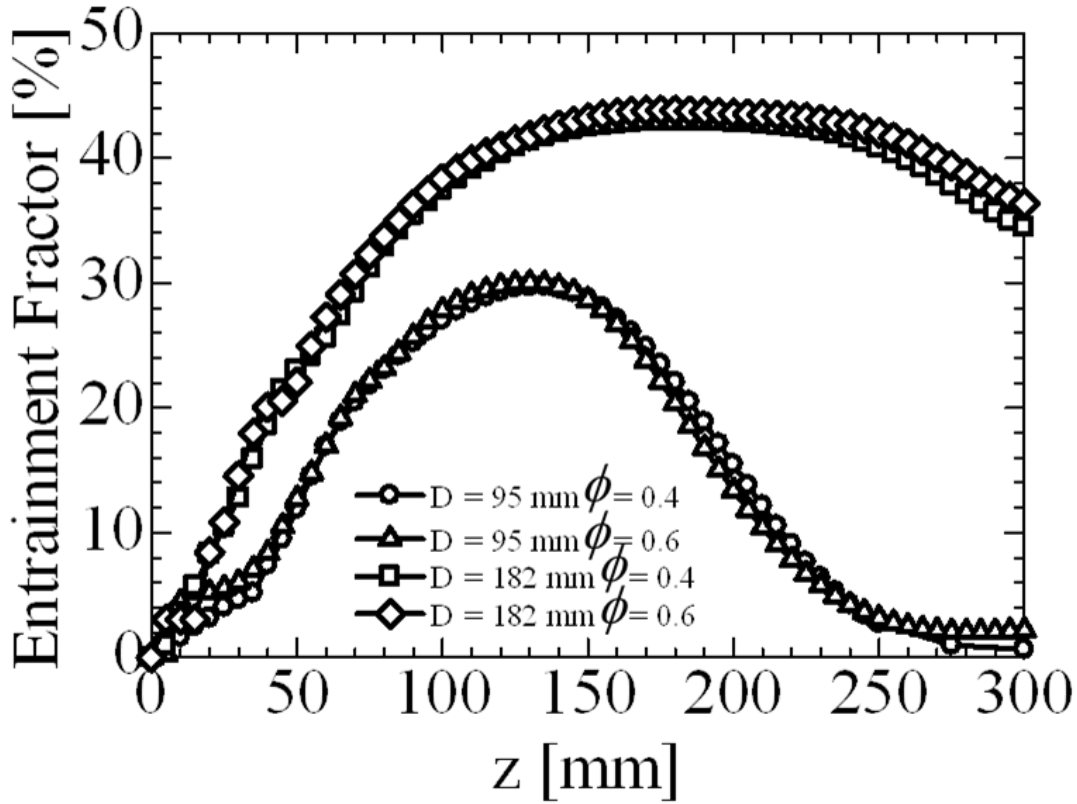
**Fig. 4.6 Entrainment Factor in terms of *D* and $\phi$ ,for $\Delta U_a$ = 8 m/s**

### 4.3.4  Dilution characteristics

The entrainment of burnt and inert gases, such as $CO_2$, $H_2O$, and $N_2$, into the flame, because of recirculation, leads to self-dilution. The local dilution factor, as defined in Eq. (4.12), characterizes the entrained burnt and inert gases mass quantities into the flame at each cross section with the respect to the jet zone mass flow rate.

$$\text{Local Dilution Factor}(z) = \frac{\int_0^{\Delta z}\left[\dfrac{dM_z}{dz}\right]\times\left(\tilde{Y}_{CO2}+\tilde{Y}_{H2O}+\tilde{Y}_{N2}\right)_{Near wall} dz}{M_z}\times100 \qquad (4.12)$$

where *Y* is mass fraction of the species and $\Delta z$ = 0.005 m. Figure 4.7 shows the local dilution factor variation, in terms of *D*, for $\phi$ = 0.4 and $\Delta U_a$ = 8 m/s. The increase in *D* increases the local dilution of the flame as shown in Fig. 4.7. The strong entrainment in large cylinder should lead to
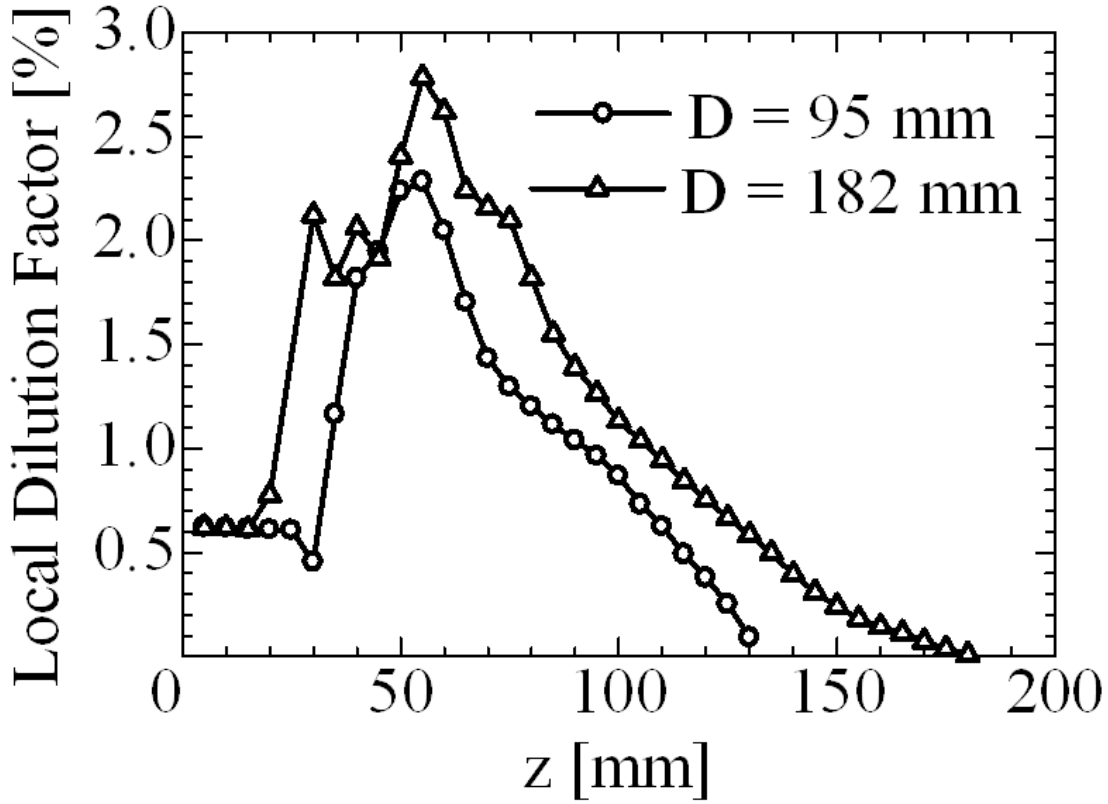
**Fig. 4.7 Local dilution factor variation in terms of $D$, for $\phi = 0.4$ and $\Delta U_a = 8$ m/s**

higher local dilution in the flame region. The local dilution factors increase up to $z = 60$ mm along axial direction irrespective of the inner diameter, and then gradually decrease up to the location, in which the jet zone mass flow rate reaches its maximum value. Because, as shown in Fig. 4.5, the gradient of jet zone mass flow rate along the axial direction increases up to $z = 60$ mm irrespective of the inner diameter, and then the gradient gradually decreases. This behavior should reflect in the local dilution factor variation. The integration of local dilution factors along the axial direction derived the total flame dilution as shown in Eq. (4.13).

$$\text{Total Flame Dilution} = \frac{\int_0^{z_1} \left[ \frac{dM_z}{dz} \right] \times \tilde{Y}_{(CO_2 + H_2O + N_2) Near\,wall}(z) \, dz}{M_{z,\,max}} \times 100 \qquad (4.13)$$

where $z_1$ locates the axial distance which has maximum jet zone mass flow rate, $M_{z,max}$. Thus, total flame dilution factors, in the case of $\phi = 0.4$, for $D = 95$ mm and 182 mm, are 23% and 34%, respectively, whereas, in the case of $\phi = 0.6$, the total dilutions are 21% and 34%, for $D = 95$ mm and 182 mm, respectively. Generally, the calculation verifies that confined flame self-dilution is enhanced by the increase in the inner diameter of the furnace. However, an increase in $\phi$ in small cylindrical furnaces leads to a decrease in flame self-dilution because the small diameter of the furnace limits burnt gas recirculation, as discussed above. On the other hand, an increase in $\phi$ in large cylindrical furnaces leads to either a constant in flame self-dilution or an increase in flame self-dilution. The large cylindrical furnace results in strong burnt gas recirculation, and an increase in $\phi$ results in a lower residual $O_2$ concentration in burnt gases. Both of these factors result in strong flame self-dilution in lager cylinders.

### 4.3.5   NOx Emission characteristics

Figure 4.8 shows radial distributions of NOx emission with respect to the $D$ and $\phi$ for $\Delta U_a = 8$ m/s. The increase in $D$ leads to a decrease in NOx at each axial position because of the strong flame dilution. The EINOx at the furnace exit was calculated by assuming continuity of the mass flow rate at the furnace exit, and the EINOx was then plotted with the total flame dilution, as shown in Fig. 4.9. The increase in flame dilution decreases the EINOx significantly.

## 4.4   Conclusions

In this study, a numerical evaluation was performed in order to characterize the effect of self-dilution in confined flames, in terms of the furnace geometry and global equivalence ratio, on NOx emission properties. In confined flames, the recirculation vortex, which is generated between the flame and the furnace wall, leads to self-dilution of combustion mixture. Therefore, the enhancement of the self-dilution should lead to the peak temperature reduction in the furnace, and thereby, considerable thermal NOx abatement. In order to quantify the entrainment, and consequently, dilution, in confined flames, a parameter, $M_z$, which represents the jet zone mass flow rate, was introduced. The study found that the increase in inner diameter of cylindrical furnace leads to the significant development of $M_z$ long the axial direction because of larger recirculation vortex in the larger cylinder. Then, higher entrainment leads to the grater flame

dilution in the large cylindrical furnaces. The EINOx characteristics of confined flames exhibit a liner reduction with increase in flame self-dilution. Thus, this study verified that that the EINOx
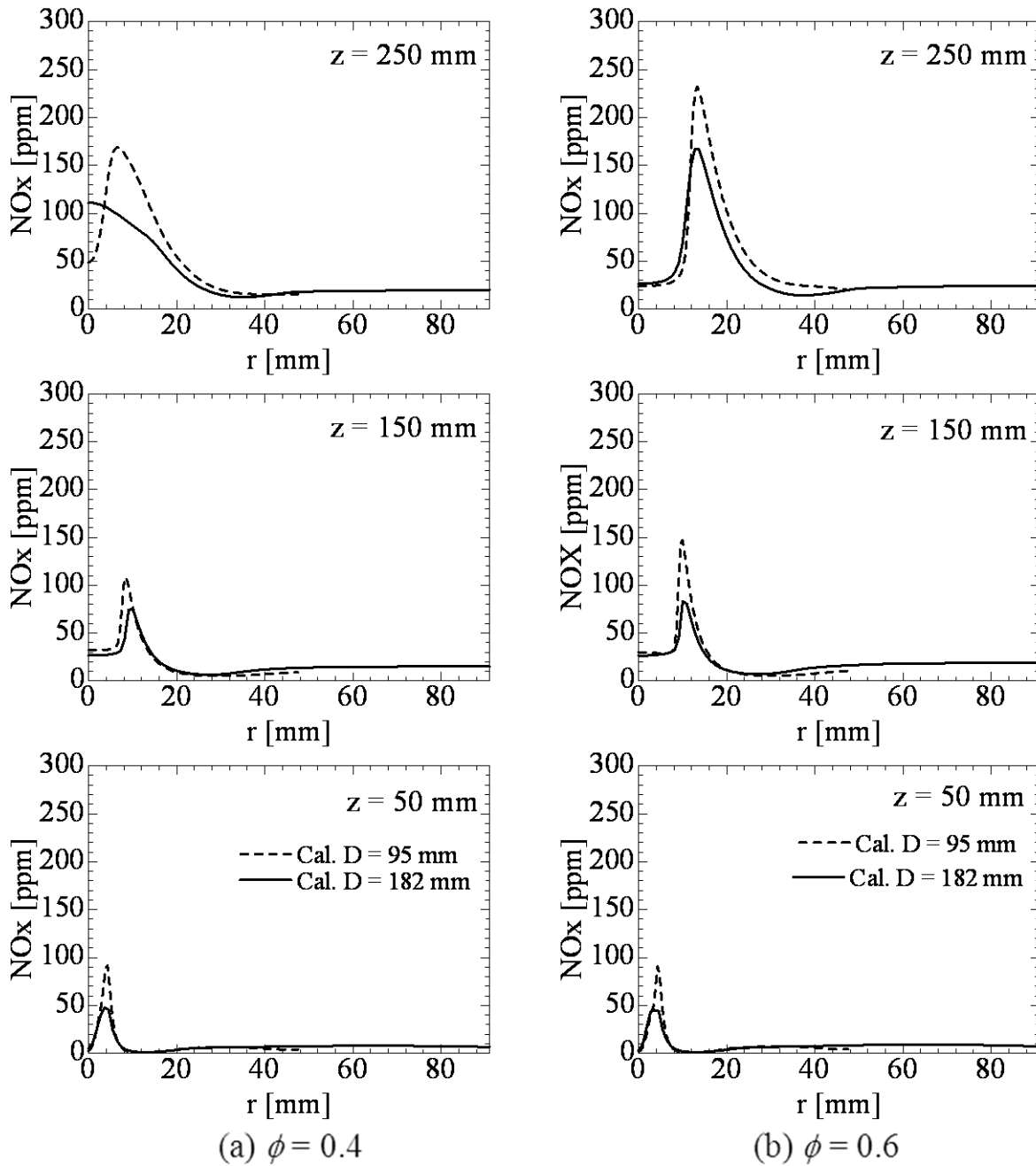


**Fig. 4.8 Radial distributions of NOx emission in terms of $D$ and $\phi$, for $\Delta U_a = 8$ m/s**
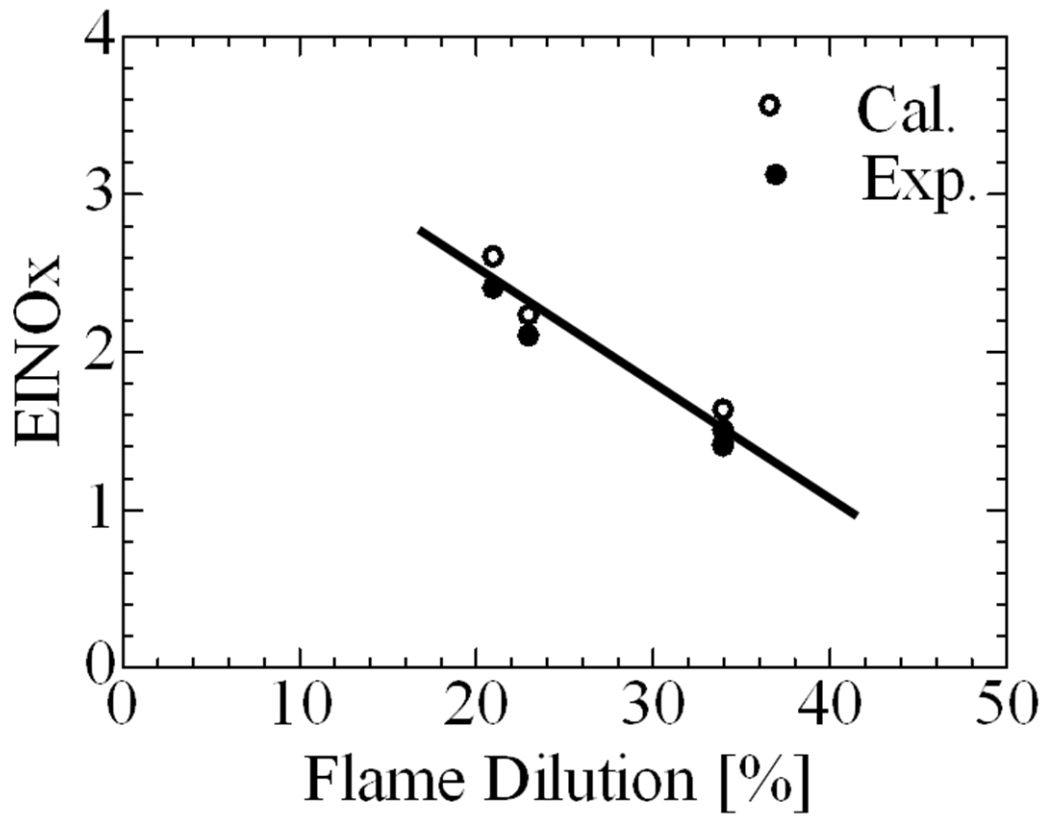
**Fig. 4.9 EINO$_X$ with total flame dilution**

of confined non-premixed flames is primarily dominated from the flame self-dilution, through the entrainment of burnt gases, and the enhancement of self-dilution of confined flames can be achieved by the increase in the inner diameter of the cylindrical furnace.

# CHAPTER 5

# DETERMINATION OF THE FLAME STRUCTURES OF CONFINED FLAMES IN THE MIXTURE FRACTION DOMAIN

## 5.1    Introduction

A confined combustion system with the self-recirculation can be referred as an unsteady combustion process. In a confined combustion system, two main exemplificative asymptotic conditions can be considered. In the first case, the air, which issued from the annular nozzles, starts to mix with high-temperature burnt gases, including residual oxygen, which are transported upstream in the furnace, and this yields hot diluted oxidant, which can mix and react with the fuel, issued from the central nozzle at room temperature. In the second case, both the fuel and the air, which issued from the central and annular nozzles, respectively, can mix with the high-temperature burnt gases, including residual oxygen, because of strong turbulence, and this yields hot diluted fuel/oxidant stream, and then start to react. Consequently, in confined flames, internal recirculation should generate variable-composition fuel and air streams along the axial direction. Thus, in this study, the confined flame-structures along the axial direction, in the mixture fraction domain are examined using the counter-diffusion configuration.

## 5.2    Problem formulation, numerical models and initial conditions

An investigation of a steady, two-dimensional diffusive layer was performed by means of the counter jets configuration. Depending on the pre-heating and dilution level of fuel and oxidant jets, because of the entrainment in confined flames, four cases of dilution were hypothetically generated. In this study, attention was focused on the confined combustion system of the inner diameter, $D = 182$ mm, the global equivalence ratio, $\phi = 0.6$, and air velocity difference, $\Delta U_a = 8$ m/s. The recirculated burnt gas mass quantity ($M_b$) along the axial direction ($z$) in the confined combustion system is computed by ($M_z - M_0$), where $M_z$ and $M_0$ are the jet zone mass flow rate at the location of z and the initial jet mass flow rate at z = 0, respectively, and the variation of $M_b$ along the axial direction is shown in Fig. 5.1. The maximum amount of recirculated burnt gas is reported at an axial distance of $z = 180$ mm. According to the experimental measurements and numerical calculations, the complete combustion of propane-air was achieved in the furnace, and
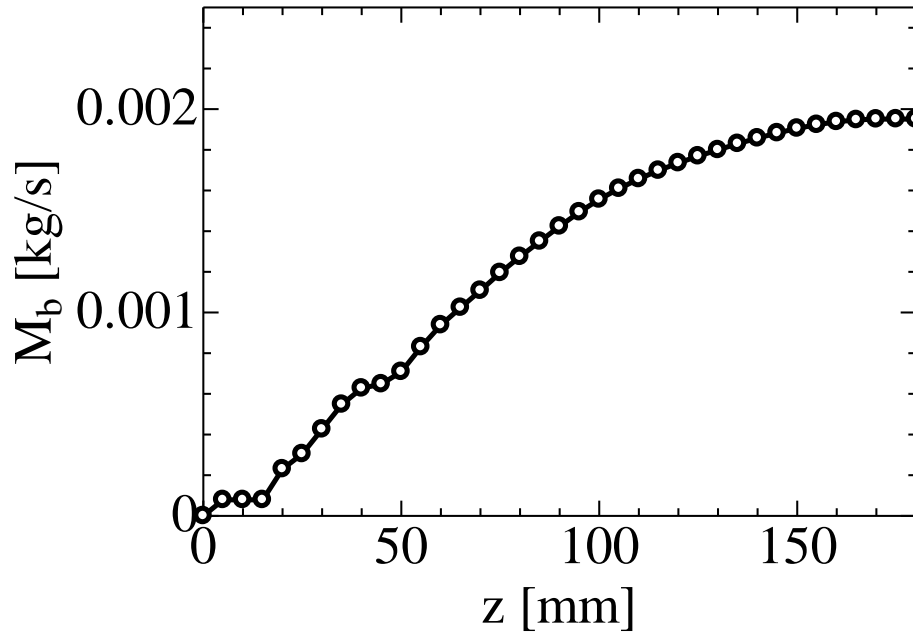
**Fig. 5.1 The recirculated burnt gas mass quantity ($M_b$) along the axial direction for $D = 182$ mm, $\phi = 0.6$, and $\Delta U_a = 8$ m/s**

thus, the burnt gas composition is computed as a chemical equilibrium composition of the fuel and oxidizer mixture at the complete combustion. The presence of small amounts of radicals in the burnt gas is neglected in this study, and only major species are considered. Because of the heat loss in the furnace, as shown in the experimental measurements and numerical calculations, temperature of the burnt gas is assumed to be cooled to 800 K. The average specific heat capacities of air, fuel, and burnt gas are 1.0, 1.67, and 1.35 kJ/kg K, respectively. The mass fraction of species and temperature of the burnt gas, for the global equivalence ratio, $\phi = 0.6$, are summarized in Table 5.1

**Table 5.1 Temperature and mass fraction of species in the burnt gases for $\phi = 0.6$**

| Temperature and mass fraction of species in the burnt gases | |
|---|---|
| $CO_2$ | 0.11 |
| $H_2O$ | 0.06 |
| $N_2$ | 0.74 |
| $O_2$ | 0.09 |
| $C_3H_8$ | 0.00 |
| Temperature | 800 K |

Then, four types of preheating/dilution cases were established to calculate the inlet conditions of the fuel and the air streams in terms of the axial distance according to the ratio of $M_{b,O}/M_b$ : $M_{b,F}/M_b$; where $M_{b,O}$ and $M_{b,F}$ are the hypothetical burnt gas mass quantity which mixes with the fresh air and the fuel streams, respectively.

(a) Case 1: $M_{b,O}/M_b$ : $M_{b,F}/M_b$ = 1: 0 (only the air stream is fully preheated and diluted by the recirculated burnt gas mass quantity and the undiluted fuel stream is at room temperature)

(b) Case 2: $M_{b,O}/M_b$ : $M_{b,F}/M_b$ = 0.91 : 0.09 (the air and the fuel streams are partially preheated and diluted by the recirculated burnt gas mass quantity)

(c) Case 3: $M_{b,O}/M_b$ : $M_{b,F}/M_b$ = 0.67 : 0.33 (the air and the fuel streams are partially preheated and diluted by the recirculated burnt gas mass quantity)

(d) Case 4: $M_{b,O}/M_b$ : $M_{b,F}/M_b$ = 0.5 : 0.5 (the air and the fuel streams are preheated and diluted by the recirculated burnt gas mass quantity)

Accordingly, the inlet flow conditions of the fuel and the air streams (temperature and mass fraction of species) at axial distances of $z$ = 50 mm, 100 mm, 150 mm, and 175 mm are computed for the four dilution cases, and values are summarized in the Table 5.2.

**Table 5.2 Inlet flow conditions (temperature and mass fraction of species) in diluted and pre-heated fuel and air streams in terms of axial distance ($z$)**

(a) Dilution case 1     $M_{b,O}/M_b$ : $M_{b,F}/M_b$ = 1 : 0

| z/Y | Air | | | | Fuel | | | |
|---|---|---|---|---|---|---|---|---|
| | 50 | 100 | 150 | 175 | 50 | 100 | 150 | 175 |
| $CO_2$ | 0.026 | 0.044 | 0.050 | 0.050 | 0.000 | 0.000 | 0.000 | 0.000 |
| $H_2O$ | 0.014 | 0.024 | 0.027 | 0.028 | 0.000 | 0.000 | 0.000 | 0.000 |
| $N_2$ | 0.763 | 0.758 | 0.756 | 0.756 | 0.000 | 0.000 | 0.000 | 0.000 |
| $O_2$ | 0.197 | 0.174 | 0.167 | 0.166 | 0.000 | 0.000 | 0.000 | 0.000 |
| $C_3H_8$ | 0.000 | 0.000 | 0.000 | 0.000 | 1.000 | 1.000 | 1.000 | 1.000 |
| T[K] | 447 | 537 | 562 | 565 | 300 | 300 | 300 | 300 |

(b) Dilution case 2     $M_{b,O}/M_b : M_{b,F}/M_b = 0.91 : 0.09$

| z/Y | Air | | | | Fuel | | | |
|---|---|---|---|---|---|---|---|---|
| | 50 | 100 | 150 | 175 | 50 | 100 | 150 | 175 |
| $CO_2$ | 0.024 | 0.042 | 0.047 | 0.048 | 0.045 | 0.066 | 0.071 | 0.072 |
| $H_2O$ | 0.013 | 0.023 | 0.026 | 0.026 | 0.024 | 0.036 | 0.039 | 0.039 |
| $N_2$ | 0.763 | 0.758 | 0.757 | 0.757 | 0.300 | 0.444 | 0.480 | 0.483 |
| $O_2$ | 0.200 | 0.177 | 0.170 | 0.169 | 0.037 | 0.054 | 0.058 | 0.059 |
| $C_3H_8$ | 0.000 | 0.000 | 0.000 | 0.000 | 0.594 | 0.400 | 0.352 | 0.347 |
| T[K] | 436 | 525 | 550 | 553 | 478 | 574 | 596 | 601 |

(c) Dilution case 3     $M_{b,O}/M_b : M_{b,F}/M_b = 0.67 : 0.33$

| z/Y | Air | | | | Fuel | | | |
|---|---|---|---|---|---|---|---|---|
| | 50 | 100 | 150 | 175 | 50 | 100 | 150 | 175 |
| $CO_2$ | 0.019 | 0.034 | 0.039 | 0.040 | 0.079 | 0.093 | 0.096 | 0.096 |
| $H_2O$ | 0.010 | 0.018 | 0.021 | 0.021 | 0.043 | 0.051 | 0.052 | 0.053 |
| $N_2$ | 0.765 | 0.761 | 0.759 | 0.759 | 0.529 | 0.626 | 0.645 | 0.646 |
| $O_2$ | 0.206 | 0.187 | 0.181 | 0.180 | 0.064 | 0.076 | 0.078 | 0.079 |
| $C_3H_8$ | 0.000 | 0.000 | 0.000 | 0.000 | 0.285 | 0.154 | 0.129 | 0.126 |
| T[K] | 407 | 487 | 511 | 514 | 634 | 708 | 722 | 724 |

(d) Dilution case 4     $M_{b,O}/M_b : M_{b,F}/M_b = 0.5 : 0.5$

| z/Y | Air | | | | Fuel | | | |
|---|---|---|---|---|---|---|---|---|
| | 50 | 100 | 150 | 175 | 50 | 100 | 150 | 175 |
| $CO_2$ | 0.015 | 0.028 | 0.032 | 0.032 | 0.087 | 0.098 | 0.100 | 0.010 |
| $H_2O$ | 0.008 | 0.015 | 0.017 | 0.018 | 0.047 | 0.054 | 0.055 | 0.055 |
| $N_2$ | 0.766 | 0.762 | 0.761 | 0.761 | 0.585 | 0.660 | 0.673 | 0.675 |
| $O_2$ | 0.211 | 0.195 | 0.190 | 0.189 | 0.071 | 0.080 | 0.082 | 0.082 |
| $C_3H_8$ | 0.000 | 0.000 | 0.000 | 0.000 | 0.210 | 0.108 | 0.090 | 0.088 |
| T[K] | 385 | 455 | 477 | 480 | 676 | 734 | 745 | 746 |
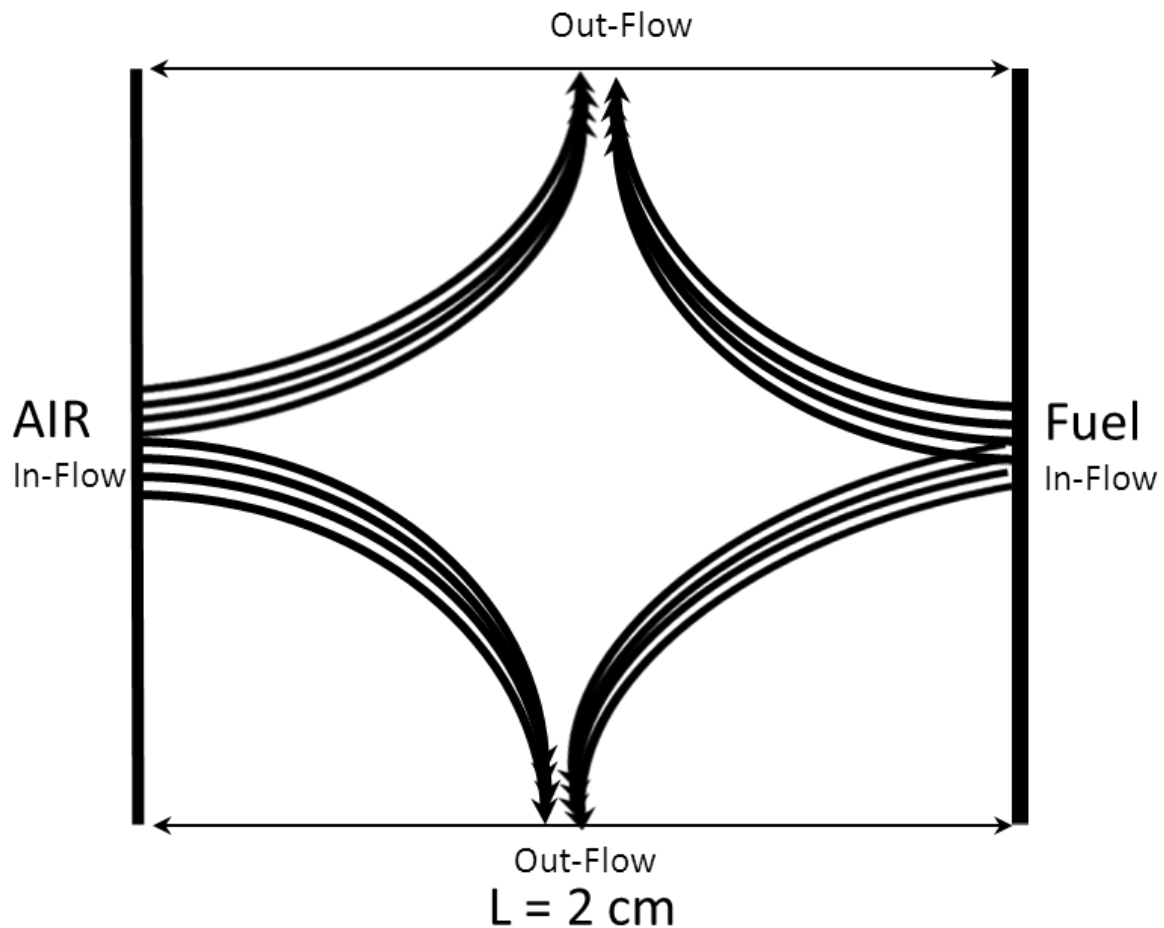
**Fig. 5.2 Schematization of the steady two-dimensional diffusive layer configuration**

The counter-diffusion configuration is schematized in Fig. 5.2. The flow rates ($V$) of the counter jets were set in such a way that, their kinetic energies are equal, meaning that the stagnation point in frozen conditions always occurs in the middle of the two inlet sections, and the average flame strain rate ($K = V/L$) was fixed at 50 s$^{-1}$.

A structured two-dimensional mesh, which was generated using OpenFOAM block-mesh [48], was used. The mesh consists of 4 $\times$ 10000 quadrilateral cells with a uniform spacing of 0.1 mm. Velocity inlet boundary conditions were used to define the flow velocity at the fuel and oxidant inlets, whereas outflow boundary conditions were used to model the flow outlets. Numerical analysis was performed using the OpenFOAM [48] finite-volume solver, by assuming a laminar two-dimensional flow structure. In addition, in the governing equations of species mass fraction

and sensible enthalpy, the unity Lewis number assumption was used. The propane-air detailed oxidation mechanism of Warnatz [34], which involves 32-species and 123-reaction steps, was implemented with the GRI 2.11 [39] NOx chemistry mechanism. In the previous studies of chapters 3 and 4, the 69-step/28-species reduced kinetics was employed because it had showed a good agreement with the Warnatz detailed mechanism with a fair degree of precision [34]. However, in the counter diffusion configuration, Warnatz mechanism was used to enhance the accuracy of the chemistry calculations.

Simulations were performed at atmospheric pressure. The ideal gas law was used for density calculations, whereas viscosity calculation was performed by using the Sutherland's law over a wide range of temperatures. The initial distribution of the species mass fractions, temperature and velocity was set equal to a step function from the inlet values. The space discretization was done using a second-order upwind scheme whereas an implicit integration method was used for time discretization as usual. The initial CFD time-step was selected as $1 \times 10^{-6}$ s with a corresponding Courant number of approximately 0.4, whereas the initial chemical time-step was selected as $1 \times 10^{-7}$ s.

All evaluations were made after the system was reached to the steady sate. The structure of the reactive zones, in terms of axial distance, for the four dilution cases were analyzed by an evaluation of the temperature and NO mass fraction distributions as a function of the mixture fraction ($Z$). The mixture fraction is used as a parameter to quantify mixing of the streams, and the mixture fraction of propane-air mixture was computed using the definition in Eq. (5.1), and the definition is corresponded to the Bilger's mixture fraction definition for methane-air mixture [53].

$$Z = \frac{\frac{5}{8}M_H^{-1}[Z_H - Z_{H,2}] + \frac{5}{3}M_C^{-1}[Z_C - Z_{C,2}] - M_o^{-1}[Z_o - Z_{o,2}]}{\frac{5}{8}M_H^{-1}[Z_{H,1} - Z_{H,2}] + \frac{5}{3}M_C^{-1}[Z_{C,1} - Z_{C,2}] - M_o^{-1}[Z_{o,1} - Z_{o,2}]} \tag{5.1}$$

where $Z_H$, $Z_C$, and $Z_O$ are the elemental mass fractions of the hydrogen, carbon and oxygen elements, respectively; $M_H$, $M_C$, and $M_O$ are the corresponding atomic masses; 1 and 2 digits

correspond to the fuel and oxidizer streams; and the mixture fraction, according to this definition, is a passive scalar normalized between $Z = 0$ and $Z = 1$ in the possibly diluted oxidizer and fuel, respectively.

In addition to the preheated and diluted conditions, a study was also carried out for the undiluted streams at the room temperature as a reference for the discussion.

## 5.3    Results and discussion



**Fig. 5.3 Distributions of temperature and NO mass fraction in the dilution case 1**

Table 5.2 (a) shows the temperature and mass fraction of species at the air and the fuel sides, in terms of axial distance, in the counter-flow flame after fully mixing of the hot burnt gas with the fresh air in the dilution case1. It can be seen that the burnt gas mixing has a considerable influence on the boundary conditions (initial temperature and species mass fraction) of the air, with respect to axial distance, of the counter-diffusion flow. This change in composition leads to various flame temperatures and NO formation, depending on the axial distance, as shown in Fig. 5.3. In the mixture fraction domain ($Z$), the peak value of temperature decreases with the increasing axial distance because of higher flame dilution. Moreover, temperature distributions of $z = 150$ mm and 175 mm overlap each other because, in this region, flame achieves its maximum dilution. The maximum temperature reduction is approximately 200 K, corresponding to the without-dilution case at the axial distance of $z = 150$ mm and 175 mm. In addition, peak temperature profiles are located at different mixture fraction for the various axial distances.
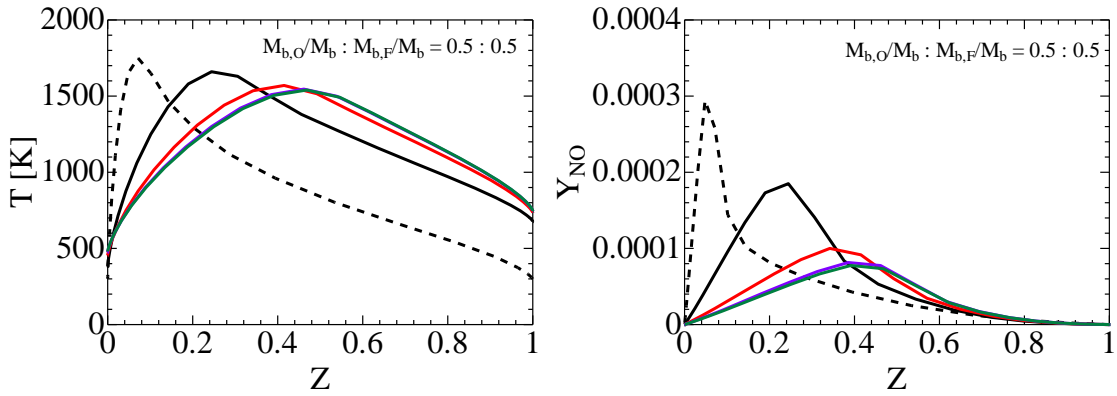
(c) Dilution case 4    $M_{b,O}/M_b : M_{b,F}/M_b = 0.5 : 0.5$
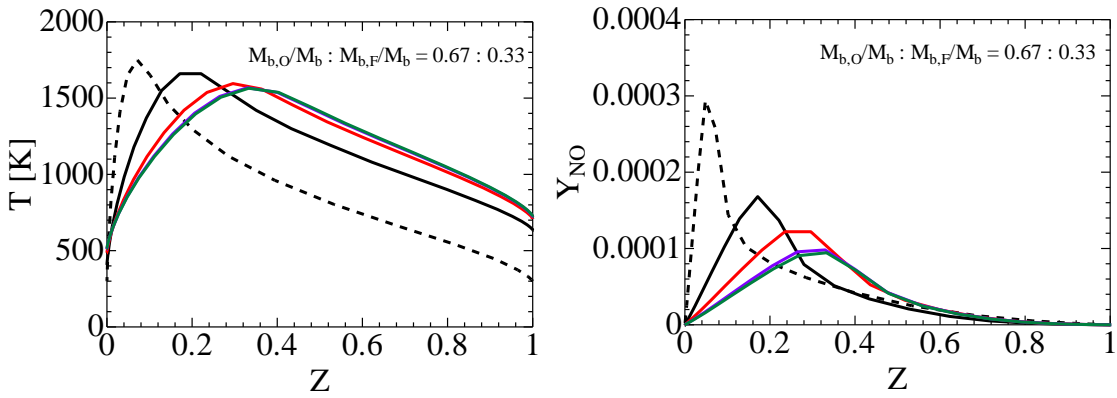


(b) Dilution case 3  $M_{b,O}/M_b : M_{b,F}/M_b = 0.67 : 0.33$



(a)  Dilution case 2 $M_{b,O}/M_b : M_{b,F}/M_b = 0.91 : 0.09$

**Fig. 5.4 Distributions of temperature and NO mass fraction in the dilution cases 2 - 4**

These mixture fractions are closer to the oxidizer side and their values are approximately equal to the stoichiometric values. NO formation follows the trend of the temperature. When considered the sufficiently low temperature levels ($< 1,600$ K), at the axial distance of $z = 150$ mm and 175 mm, in Fig. 5.3, NO formation was significantly decreased. This happens because of negligible formation of thermal NO at these temperature levels. Thus, Fig. 5.3 provides clear evidence that, in confined combustion system, even burnt gas mixing occurs with only the fresh air significant NO reduction can be achieved.

Tables 5.2 (b), (c), and (d) show the temperature and mass fraction of species at the air and fuel sides, in terms of axial distance, in the counter-flow flame after partially mixing of the hot burnt gas with the fresh air and the fuel streams in the dilution cases 2, 3 and 4. Table 5.2 (b) shows that very small amount of burnt gas mixing with the fuel stream has a significant effect on initial conditions of temperature and species mass fraction of fuel stream, and the effect is extensively increased with the increase of amount of burnt gas quantity, which is supposed to be mix with the fuel stream as shown in Tables 5.2 (c) and (d). The burnt gas mixing with the fuel and the air streams leads to more uniform temperature distributions, than dilution case 1, as shown in Fig. 5.4. This is caused by elevated temperature of reactants on both sides as a result of pre-heating of both streams. Similar to the dilution case 1, there is a significant temperature reduction, and thereby NO reduction, at axial distances of $z = 150$ mm and 175 mm corresponding to the without-dilution because of higher flame dilution. However, in the dilution cases 2, 3, and 4, there is a slightly higher peak temperature and NO formation, when compared to the dilution case 1. This happens as a result of the low conductive heat loss to the reactant streams as a result of the elevated temperature for both streams. Moreover, in the dilution cases 2, 3 and 4, the mixture fractions which are related to the maximum temperatures are closer to the fuel side, and however, their values are approximately equal to the stoichiometric values as similar to the dilution case 1.

Thus, Figs. 5.3 and 5.4 provide a clear evidence that, in a confined combustion system, the effect of self-dilution has a significant influence on maximum flame temperature reduction, and thereby NO abatement.
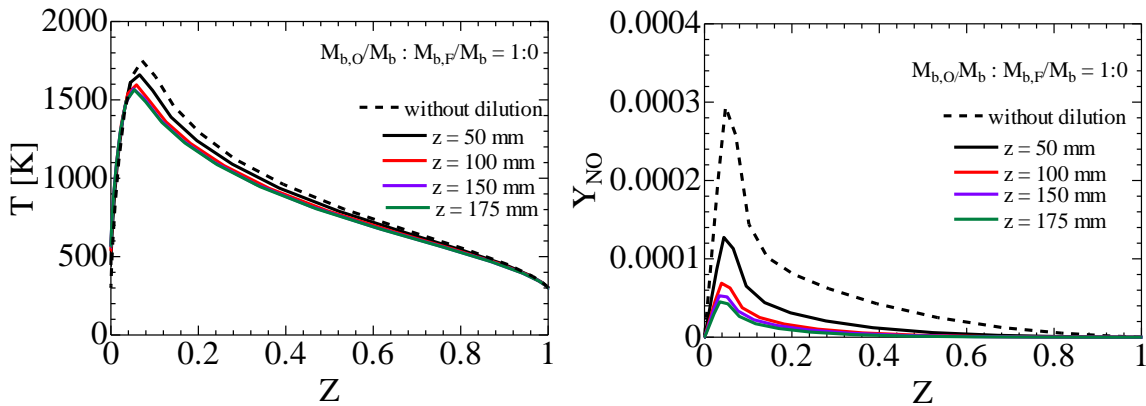
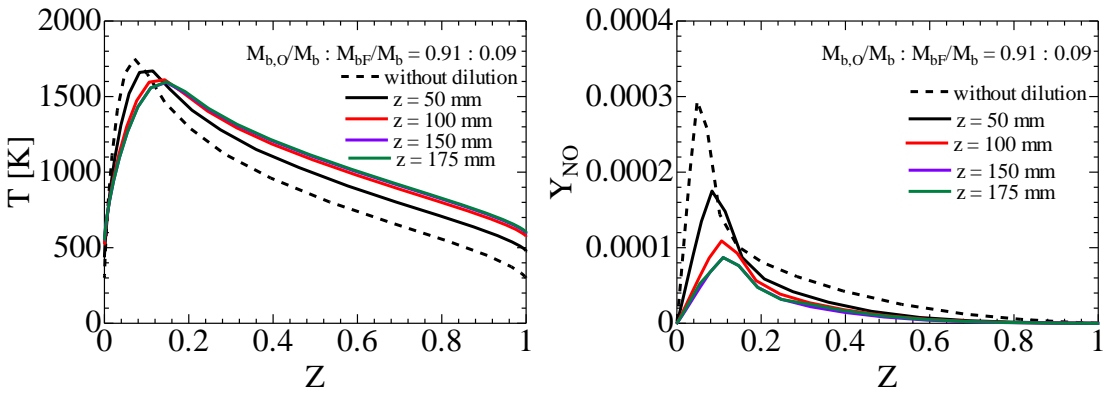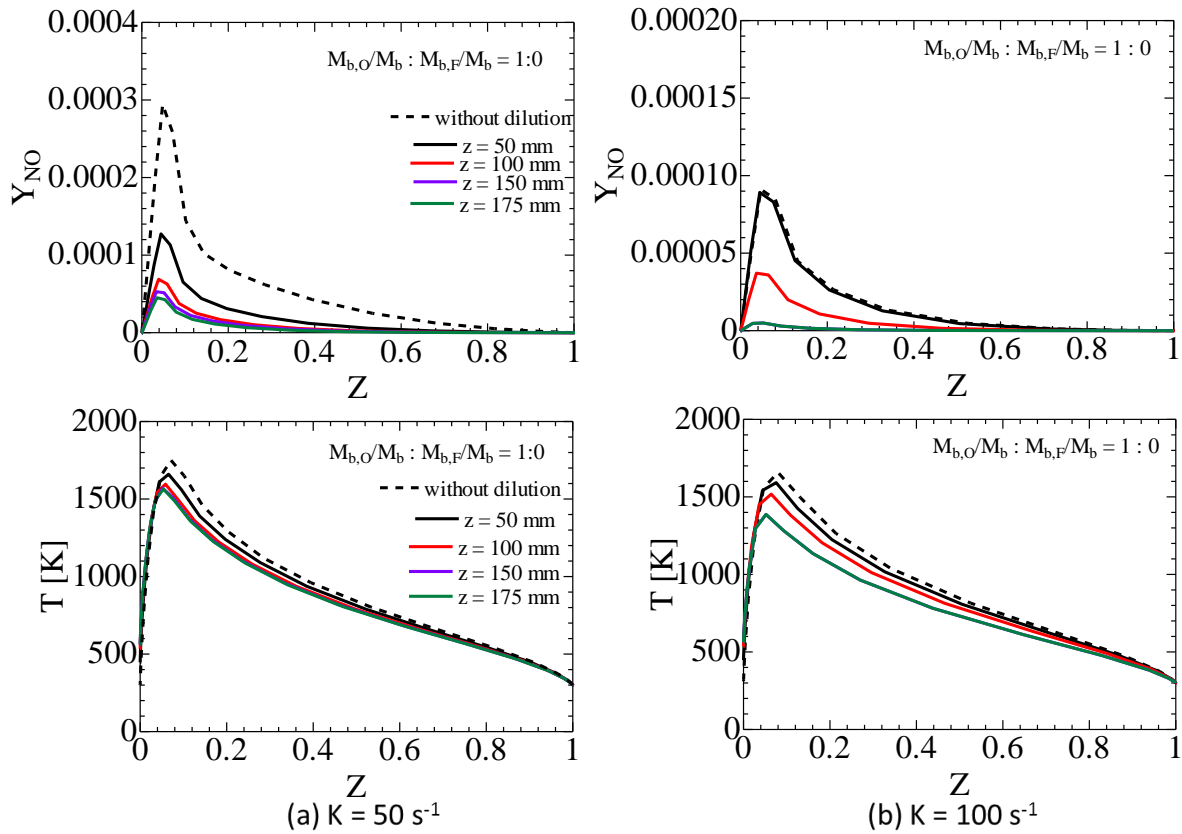**Fig. 5.5 Distributions of temperature and NO mass fraction in the dilution case 1, in terms of strain rate (K)**

In addition, an investigation of the flame structures, along of axial direction in confined flames, was made in terms of strain rate, $(K = V/L)$, as shown in Figs. 5.5 and 5.6. In this study, the calculation of flame-structures in the dilution cases 1 and 3 were repeated with the flame strain rate of $100s^{-1}$. The increase in strain rate is associated to the increase in air velocity difference $(\Delta U_a)$ in the experimental studies. The increase in the strain rate (or air velocity difference) should lead to the flame stretch effect. The general behavior of the flame structures in the dilution cases 1 and 3 with the strain rate $100s^{-1}$ is almost same as to the case of strain rate of $50\ s^{-1}$. However, at the higher strain rate $(K = 100s^{-1})$, irrespective of the dilution case, the maximum temperatures at each axial distance are lower than the case of $50\ s^{-1}$ and thereby NO formation takes a significantly lower value. This is caused by an enhanced conduction of heat owing to larger gradients at the higher strain rates. The conductive heat loss is proportional to the scalar dissipation rate, $\chi$, which is defined in Eq. 5.2, and $\chi$ is a key quantity in the
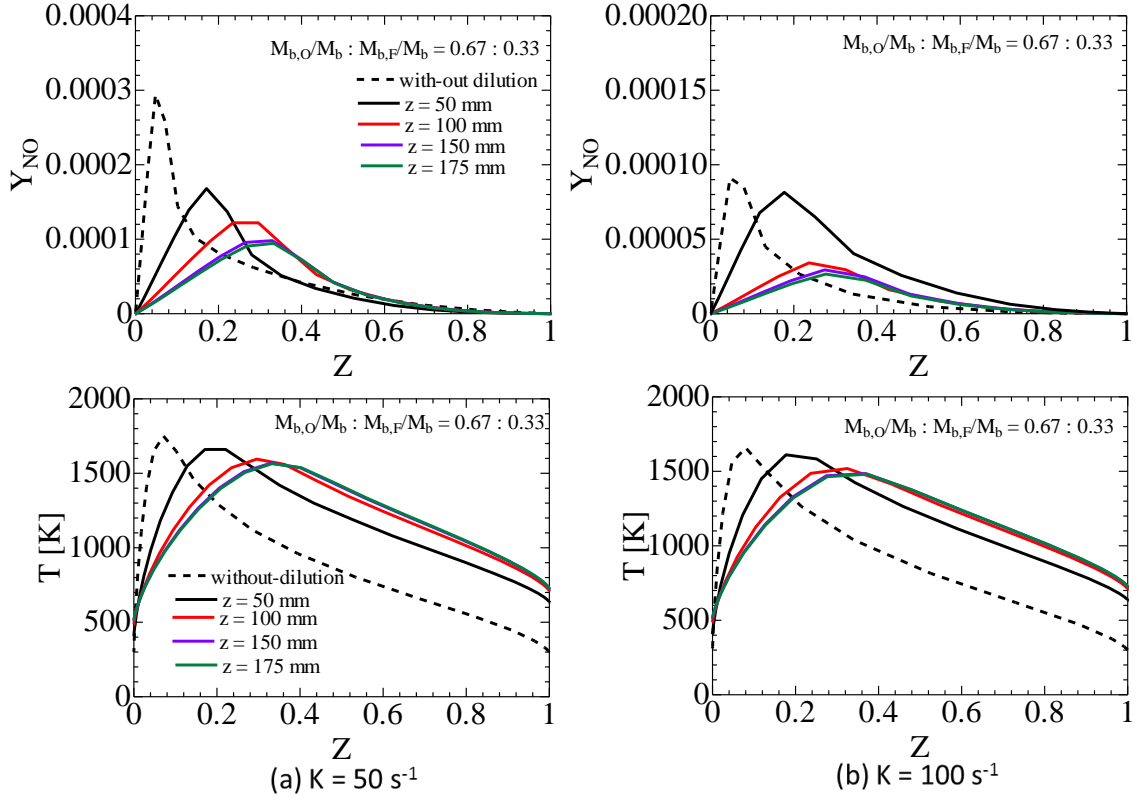
**Fig. 5.6 Distributions of temperature and NO mass fraction in the dilution case 3, in terms of strain rate (K)**

description of diffusion flames [24]. Thus, the increase in strain rate leads to the increase in scalar dissipation rate, and thereby, conductive heat losses.

$$\chi = 2\frac{\lambda}{\rho c_p}(\nabla Z)^2 \qquad (5.2)$$

where $\lambda$ is the coefficient of thermal conductivity.

Finally, the effect of inner diameter of the cylindrical furnace on the NOx reduction was indirectly evaluated using the flame-structures along axial direction in confined flames. In this study, the flame-structures, in terms of axial distance, of confined flame of $D = 95$ mm, $\phi = 0.6$, and $\Delta U_a = 8$ m/s are generated as discussed in Section 5.2. However, in the case of $D = 95$ mm,
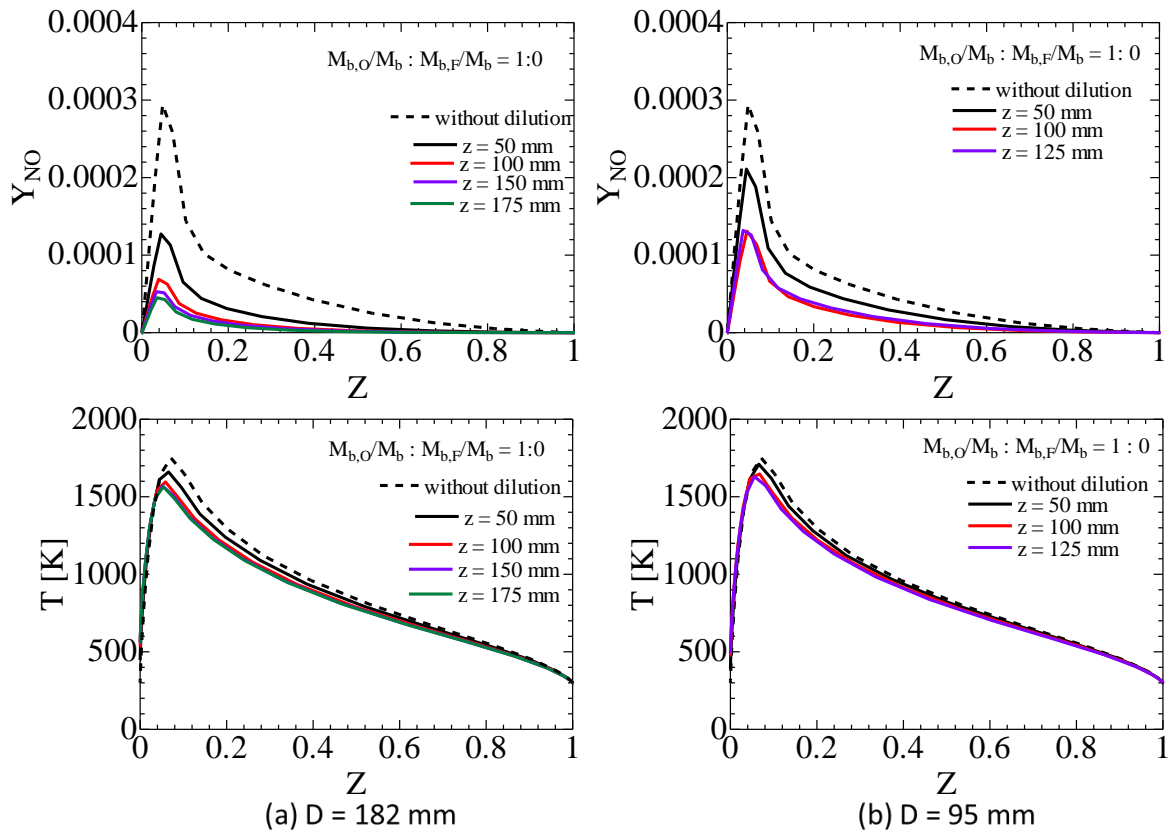
**Fig. 5.7 Distributions of temperature and NO mass fraction in the dilution case 1, in terms of inner diameter of the furnace ($D$)**

the maximum recirculated burnt gas mass quantity was reported at the axial distance $z = 130$ mm. Thus, flame structures at axial distances of $z = 50$ mm, 100 mm, and 125 mm are generated in this study for the dilution cases 1 and 3. Figures 5.7 and 5.8 show the distributions of temperature and NO mass fraction in the dilution cases 1 and 3, respectively, in terms of the inner diameter, $D$. Because of the weaker burnt gas entrainment in the case of $D = 95$ mm, the maximum temperature at the each axial distance shows higher value corresponding to the $D = 182$ mm. Moreover, the maximum temperature reduction, at the axial distance of $z = 125$ mm, corresponding to the with-out dilution case, is not highly significant. Hence, NO formation, in terms of axial distance, in the case of $D = 95$ mm, shows significantly higher value than the corresponding NO formation in $D = 182$ mm. Therefore, this study provides the verification that the increase in the inner diameter of the furnace leads to a significant NOx reduction.
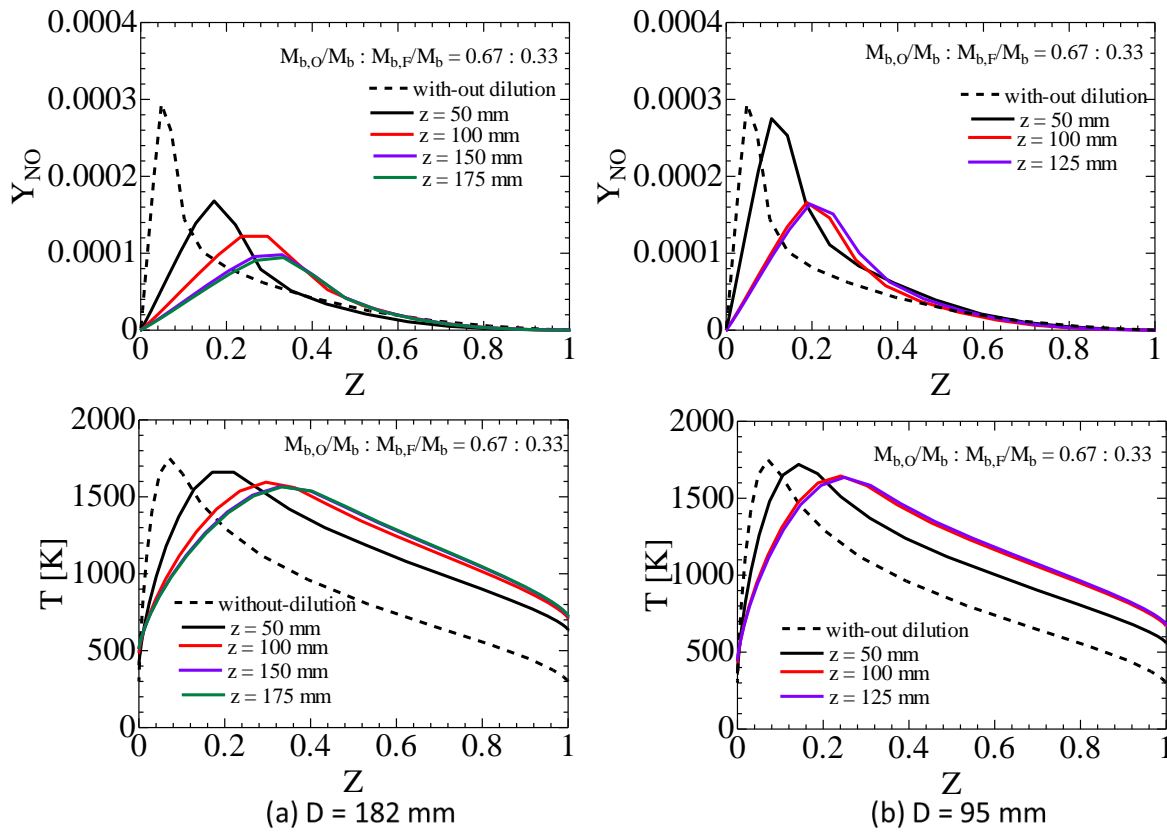
**Fig. 5.8 Distributions of temperature and NO mass fraction in the dilution case 3, in terms of inner diameter of the furnace (*D*)**

## 5.4    Conclusions

The study of confined flame structures, in terms of axial distance, in the mixture fraction domain showed that the peak value of temperature decreases with increasing axial distance because of the flame dilution in confined flames. Consequently, the NO formation was significantly decreased in the downstream of the flame. Moreover, the increase in flame strain rate, which corresponding to the increase in the air velocity difference in the experimental study, leads to a significant temperature reduction, and thereby NOx abatement as a result of the conduction heat loss. The increase in the scalar dissipation rate, owing to the flame strain increasing, is caused to the higher conduction heat loss. The comparison of flame structures, in terms of the inner diameter, shows that the entrained burnt gas mass quantity, which is a function of the inner diameter of the

furnace, plays an important role in the flame dilution, which leads to the decrease in maximum flame temperature and NOx emission.

# CHAPTER 6

# CONCLUSIONS AND RECOMMENDATIONS

## 6.1 Concluding remarks

The main objective of this dissertation was to make a numerical evaluation to characterize the effect of self-dilution phenomena in confined flames, in terms of the furnace geometry, global equivalence ratio, and air velocity difference, on NOx emission properties, and consequently realize a low-NOx combustion system using a small cylindrical furnace.

In confined flames, the recirculation vortex, which is generated between flame and the furnace wall, leads to self-dilution of the combustion mixture. Therefore, the enhancement of the self-dilution should lead to the peak temperature reduction in the furnace, and thereby, considerable thermal NOx abatement. This study was based on the comprehensive experimental study, which is performed by Noda et al., on NOx emission characteristics in turbulent non-premixed flames in Pyrex glass cylindrical furnaces, and the study showed that the NOx emission in confined flames is significantly decreased with the increase in the inner diameter of the furnace, the global equivalence ratio, and the air velocity difference. This NOx reduction is possibly caused by flame dilution and flame stretch.

Since Pyrex glass makes a penetration of thermal radiation of wave length between 0.3 μm and 0.4 μm, well insulated stainless steel cylindrical furnaces are also used to evaluate the effect on radiation on the NOx emission properties in confined flames under the same experimental conditions of Noda et al. This study showed that the radiation effect on the NOx emission, under those conditions, is small, and EINOx difference is almost constant with respect to the parameter of $DU_F\Delta U_a$; where $D$, $U_F$, and $\Delta U_a$, are the inner diameter of the furnace, fuel velocity, which relates the global equivalence ratio, and the air velocity difference, respectively. In addition, the study using the stainless steel cylinders showed the increase in global equivalence ratio in small cylindrical furnace increases the maximum flame temperature significantly and thereby the EINOx is also increased. This should be caused to the limitation of burnt gas recirculation in small cylindrical furnace. On the other hand, the study showed that, in the case of large

cylindrical furnace, the increase in global equivalence ratio leads to only the small increment in the maximum temperature and thereby the EINOx is decreased. In the large cylinders, the strong burnt gas entrainment and the decrease in residual oxygen concentration in the burnt gas with the increase in global equivalence ratio should cause to this EINOx reduction.

The numerical calculation of the physical interactions in confined flames, based on the mathematical models, paves the way to design the optimum combustion operation and prediction the pollutant emissions. However, the complicated interaction between the turbulence and chemistry makes it as a difficult task. Thus, initially, in this study, the partially-stirred-reaction combustion model has been incorporated into OpenFOAM CFD tool to investigate the turbulent flow fields, temperature, species concentration, and NOx emission of confined jet flames in small cylindrical furnace. The predicted mean axial velocities and mean temperature show an excellent agreement with the experimental measurements. Moreover, the axial distributions of mean temperature excellently predict the flame length. The mean radial distributions of species of CO and $O_2$ show a reasonable agreement with measurements, whereas the mean reaction and the mean heat-release rates verify the features of temperature and species concentration. In addition, the study numerically verified that the increase in global equivalence ratio in small cylinder furnaces lead to the increase in EINOx.

Then, this study made a numerical evaluation to characterize the effect of self-dilution in confined flames in terms of the furnace geometry and global equivalence ratio on NOx emission. In order to quantify the burnt gas entrainment, and consequently, the flame self-dilution, in confined flames, a parameter which represents the jet zone mass flow rate were introduced. The study found that the increase in inner diameter of cylindrical furnace leads to the significant development of the jet zone mass flow rate long the axial direction because of larger recirculation vortex in the larger cylinder. Accordingly, higher entrainment leads to the grater flame self-dilution in the large cylindrical furnaces. The EINOx characteristics of confined flames showed a liner reduction with increase in flame self-dilution. Thus, this study verified that EINOx of confined non-premixed flames is primarily dominated from the flame self-dilution, through the entrainment of burnt gases.

Finally, the confined flame structures, in terms of the axial distance, in the mixture fraction domain were examined using a counter diffusion configuration. In confined flames, the internal recirculation should generate the variable compositions of the fuel and the air streams along the axial direction, and consequently, a confined combustion system can be called as an unsteady combustion process. The study showed that the peak value of temperature decreases with increasing the axial distance because of higher flame dilution in the downstream of confined flames. Consequently, the NO formation was significantly decreased in the downstream. Moreover, the increase in flame strain rate, which corresponds to the increase in the air velocity difference in the experimental study, leads to significant temperature reduction, and thereby NOx abatement owing to the conduction heat loss. The increase in the scalar dissipation rate, as a result of the increase in flame strain rate, is caused to the higher conduction heat loss. The comparison of flame structures, in terms of inner diameter, showed that the entrained burnt gas mass quantity, which is a function of inner diameter of the furnace, plays the important role in the flame dilution, which leads to the decrease in maximum flame temperature and NOx emission.

This study, eventually, realized that the increase in inner diameter of the furnace, the global equivalence ratio, and the air velocity difference in confined combustion system leads to the decrease in maximum flame temperature and thereby NOx emission because of the flame self-dilution and the flame stretch effect. Therefore, the increase in the flame self-dilution ratio as a dominant parameter, which controls the characteristics of confined flames, is very important for NOx abatement.

## 6.2    Recommendations for future works

Even though our study could not achieve the ultra-low NOx emission, like in a sophisticated mild combustion furnace, the study shows that the confined flame combustion system can achieve the significant NOx abatement with the increase in the inner diameter, the global equivalence ratio, and the air velocity difference because of flame self-dilution. Because of the simplicity, in terms of the installation and the operation, this technique can be used in any narrow and limited spaces. The greater potential to increase the flame self-dilution, in this combustion system, by means of the simple combination of the burner and the combustion chamber, keeps this study at an

interesting space in the industrial utilization. However, in this study, the flame stability was maintained by using a pilot flame. Therefore, in future, it is suggested to identify more confined flame characteristics, which lead to the jet flame stabilizations by using an advanced CFD tools such as the large-eddy simulations (LES).

## REFERENCES

[1]     Poinsot, T. and Veynante, D.,*Theoritical and Numerical Combustion*, (2005), R.T.Edwards.

[2]     Turns, S.R., *An Introduction to Combustion: Concepts and Applications*, (2007), McGraw-Kill.

[3]     Li, S.C. and Williams, F.A., NOx Formation in Two-Stage Methane-Air Flames, *Combustion and Flames*, Vol. 118 (1999), pp. 339-414.

[4]     Katsuki, M. and Hasegawa, T., The Science and Technology of Combustion in Highly Preheated Air, *Proceedings of the Combustion Institute*, Vol. 27(1998), pp. 3135-3146.

[5]     Choi, G.M. and Katsuki, M., Advanced low NOx Combustion using Highly Preheated Air, *Energy Conversion and Management*, Vol. 42(2001), pp. 639-652.

[6]     Wunning, J.A. and Wunning, J.G., Flameless Oxidation to Reduce Thermal NO-Formation, *Progress in Energy and Combustion Science*, Vol. 23(1997), pp. 81-94.

[7]     Plessing, T., Peters, N. and Wunning, J.G., Laseroptical Investigation of Highly Preheated Combustion with Strong Exhaust Gas Recirculation, Proceedings of Combustion Institute, Vol. 27(1998), Vol. 3197-3204.

[8]     Szego, G.G., Dally, B.B. and Nathan, G.J., Operational Characteristics of Parallel Jet MILD Combustion Burner System, *Combustion and Flame*, Vol. 156(2009), pp. 429-438.

[9]     Szego, G.G., Dally, B.B. and Nathan, G.J., Scaling of NOx Emissions from a Laboratory-Scale Mild Combustion Furnace, *Combustion and Flame*, Vol. 154(2008), pp. 281-295.

[10]    Dally, B.B., Karpetis, A.N. and Barlow, R.S., Structure of Turbulent Non-Premixed Jet Flames in a Diluted Hot Co-Flow, *Proceeding of Combustion Institute*, Vol. 29(2002), pp. 1147-1154.

[11]    Oldenhof, E., Tummers, M.J., Veen, V., Roekaerts, D.J.E.M., Ignition Kernel Formation and Lift-off behavior of Jet-in-Hot-Co-Flow Flames, *Combustion and Flame*, Vol. 157(2010), pp. 1167-1178.

[12]    Oldenhof, E., Tummers, M.J., Veen, V., Roekaerts, D.J.E.M., Role of Entrainment in the Stabilization of Jet-in-Hot-Co-Flow flames, *Combustion and Flame*, Vol. 158(2011), pp. 1553-1563.

[13]    Weber, R., Orsino, S., Lallemant N. and Verlaan, A., Combustion of Natural Gas with High Temperature Air and Large Quantities of Flue Gas, *Proceeding of Combustion Institute*, Vol. 28(2000), pp.   1315-1321.

[14]    Weber, R., Smart, J.P. and Kamp, W., On the MILD Combustion of Gaseous, Liquid, and

Solid fuels in High Temperature Preheated Air, *Proceeding of Combustion Institute*, Vol. 31(2007), pp. 2779-2785.

[15]   Rottier, C., Lacour, C., Godard, G., Taupin, B., Porcheron, L. and Hauguel, R., On the Effect of Air Temperature on Mild Flameless Combustion Regime of High Temperature Furnace, *Proceedings of European Combustion Meeting*, 2009, Austria.

[16]   Rottier, C., Lacour, C., Godard, G., Taupin, B., Boukhalfa, A.M. and Honore, D., Aerodynamics Way to Reach Mild Combustion Regime in a Laboratory Scale Furnace, *Proceedings of European Combustion Meeting*, 2007, Greece.

[17]   Ayoub, M., Rottier, C., Carpentier, S., Villermaux, C., Boukhalfa, A.M. and Honore, D., An Experimental Study of Mild Flameless Combustion of Methane/Hydrogen Mixture, *International Journal of Hydrogen Energy*, Vol. 37(2012), pp. 6912-6921.

[18]   Kumar, S., Paul, P.J. and Mukunda, H.S., Studies on a New High-Intensity Low-Emission Burner, *Proceedings of Combustion Institute*, Vol. 29(2002), pp. 1131-1137.

[19]   Coats, C.M., Richardson, A.P. and Wang, S., Non-Premixed Combustion in Turbulent Mixing Layers, Part2: Recirculation, Mixing and Flame Stabilization, *Combustion and Flames*, Vol. 122(2000), pp. 271-290.

[20]   Noda, S., Inohae, J. and Saldi, Z.S., NOx Emission Characteristics of Confined Jet Non-Premixed Flames, *Proceedings of Combustion Institute*, Vol. 31(2007), pp. 1625-1632.

[21]   Chen, Y.T., Nie, J.H., Armaly, B.F. and Hsieh, H.T., Turbulent Separated Convection Flow Adjacent to Backward-Facing Step: Effects of Step Height, *International Journal of Heat and Mass Transfer*, Vol. 49(2006), pp. 3670-3680.

[22]   Yanagi, T., *Fundamental and Applications of LDV*, (1980), Nikkan Kogyo, Tokyo.

[23]   Noda, S., Inohae, J., Nakano, K. and Onuma, Y., An Experimental Study of Flame Characteristics of Jet Diffusion Flames in Cylindrical Furnaces, *Journal of Environment and Engineering*, Vol. 2(2007), pp. 505-513.

[24]   Peters, N., *Turbulent Combustion*. (2000), Cambridge University Press.

[25]   Jones, W.P. and Kakhi, M., Mathematical Modeling of Turbulent Flames, *Unsteady-Combustion*, (1996), Kluwer Academic Publishers, pp. 411-491.

[26]   Pope, S.B., PDF Methods for Turbulent Reactive Flows, *Progress in Energy and Combustion Science*, Vol. 11(1985), pp. 119-125.

[27]   Dreeben, T.D. and Pope, S.B., Probability Density Function/Monte Carlo Simulation of near-wall Turbulent Flows, *Journal of Fluid Mechanics*, Vol. 357(1998), pp. 141-166.

[28]   Girimarji, S.S., Assumed Beta-PDF Model for Turbulent Mixing: Validation and

Extension to Multiple Scalar Mixing, *Combustion Science and Technology*, Vol. 78(1991), pp. 177-196.

[29]  Baurle, R.A., Alexopoulos, G.A. and Hassan, H.A., Assumed Probability Density Function approach for Supersonic Turbulent Combustion, *Journal of Propulsion and Power*, Vol. 10 (1994), pp. 473-484.

[30]  Baurle, R.A., Alexopoulos, G.A. and Hassan, H.A., Modeling of Supertsonic Turbulent Combustion using assumed Probability Density Functions, *Journal of Propulsion and Power*, Vol. 10 (1994), pp. 777-786.

[31]  Golovichev, V., Nordin, N., Jamicki, R., and Chomiaki, J., 3D Diesel Spray Simulation using New Detailed Chemistry Turbulent Combustion Model, *SAE Paper*, (2000), 2000-01-1891.

[32]  Westbrook, C.K. and Dryer, F.L., Simplified Reaction Mechanisms for the Oxidation of Hydrocarbon Fuels in Flames, *Combustion Science and Technology*, Vol. 27(1981), pp. 31-43.

[33]  Tarrazo, E.F., Sanchez, A.L., Linan, A. and Williams, F.A., A Simple One-Step Chemistry Model for Partially Premixed Hydrocarbon Combustion, *Combustion and Flame*, Vol. 147(2006), pp. 32-38.

[34]  Djavdan, E., Darabiha, N., Glovangigli, V. and Candel, S.M., Strained Propane-Air Flames with Detailed and Reduced Kinetics Schemes, *Combustion Science and Technology*, Vol. 76 (1991), pp. 287-309.

[35]  Paczko, G., Lefdal, P.M. and Peter, N., Reduced Reaction Schemes for Methane, Methanol and Propane Falmes, *Proceedings of Combustion Institute*, Vol. 21(1986), pp. 739-748.

[36]  Pope, S.B., Computationally Efficient Implementation of Combustion Chemistry using *in-situ* Adaptive Tabulation, *Combustion Theory and Modeling*, Vol. 1(1997), pp. 41-63.

[37]  Contino, F., Jeaqnmart, H., Lucchini, T. and D'Errico, G., Coupling of in-situ Adaptive Tabulation and Dynamics Adaptive Chemistry: an Effective Method for Solving Combustion in Engine Simulation, *Proceedings of Combustion Institute*, Vol. 33(2011), pp. 3057-3064.

[38]  Miller, J.A. and Bowman, C.T., Mechanism and Modeling of Nitrogen Chemistry in Combustion, *Progress in Energy and Combustion Science*, Vol. 15(1989), pp. 287-338.

[39]  Bowman, C.T., Hanson, R.K., Davidson, D.F., Gardiner, W.C., Lissianski, V., Smith, G.P, Golden, D.M. and Frenklach, M., *http://www.me.berkeley.edu/gri_mech/*

[40]  Hewson, J.C. and Bollig, M., Reduced Mechanisms for NOx Emissions from Hydrocarbon Diffusion Flames, *Proceedings of Combustion Institute*, Vol. 26(1996), pp.

2171-2179.

[41] Ju, Y. and Niioka, T., Computation of NOx Emission of a Methane-Air Diffusion Flames in a Two-Dimentional Laminar Jet with Detailed Chemistry, Combustion Theory and Modeling, Vol. 1(1997), pp. 243-258.

[42] Cho, E.S. and Chung, S.H., Numerical Evaluation of NOx Mechanism in Methane-Air Counter-Flow Premixed Flames, Journal of Mechanical Science and Technology, Vol. 23(2009), pp. 659-666.

[43] Bozzelli, J.W. and Dean, A.M., O+NNH: A Possible New Route for NOx Production in Flames, *International Journal of Chemical Kinetics*, Vol. 27(1995), pp. 1097-1110.

[44] Galletti, C., Parente, A., Derudi, M., Rota, R. and Tognotti, Numerical and Experimental Analysis of NO Emissions from a Lab-Scale Burner Fed with Hydrogen-Enriched Fuels and Operating in MILD Combustion, *International Journal of Hydrogen Energy*, Vol 34(2009), pp. 8339-8351.

[45] Kuhnemuth, D., Normann, F., Andersson, K., Johnsson, F. and Leckner, B., Reburning of Nitric Oxide in Oxy-Fuel Firing: The Influence of Combustion Conditions, *Energy and Fuel*, Vol. 25(2011), pp. 624-631.

[46] Cao, R.R. and Pope, S.B., The Influence of Chemical Mechanisms on PDF Calculations of Non-Premixed Piloted Jet Flames, *Combustion and Flame*, Vol. 143(2005), pp. 450-470.

[47] Smith, G.P., Golden, D.M., Frenklah, M., Moriarty, N.W., Eiteneer, B., Goldenberg, M., Bowman, C.T., Hanson, R.K., Song, S., Gardiner, W.C., Lissianski, V.V. and Zhiwei, Q., *http://www.me.berkeley.edu/gri_mech/*.

[48] OpenFOAM: The Open Source CFD Tool, available from *http://www.openfoam.org*

[49] Pope, S.B., An explanation of the turbulent round-jet/plane-jet anomaly, *AIAA Journal*, Vol. 16(1978), pp. 279-281.

[50] Frassoldati, A., Sharma, P., Cuoci, A., Faravelli, T., and Ranzi, E., Kinetic and Fluid Dynamics Modeling of Methane/Hydrogen Jet Flames in Diluted Co-Flow, *Applied Thermal Engineering*, Vol. 30 (2010), pp. 376-383.

[51] Menter, F.R., Two-Equation Eddy-Viscosity Turbulence Models for Engineering Applications, *AIAA Journal*, Vol. 32 (1994), pp. 1598-1605.

[52] Wilcox, D.C., Reassessment of the Scale Determining Equation for Advanced Turbulence Models, AIAA Journal, vol. 26 (1988), pp. 1299-1310.

[53] Bilger, R.W., Starner, S.H. and Kee, R.J., On reduced mechanisms for methane-air combust. in non-premixed flames, *Combust. and Flames*, Vol. 80 (1990), pp. 135-149.

**The augmented reduced chemical kinetics for the propane-air oxidation** [34] in the form of $k_l = AT^\theta \exp(-E/R_0 T)$. Units are moles, cubic centimeters, seconds, Kelvins and calories/mole

|  | A | $\theta$ | E |
|---|---|---|---|
| H+O2<=>OH+O | 2.000e+14 | 0.000 | 16820.00 |
| H2+O<=>OH+H | 5.060e+04 | 2.670 | 6290.00 |
| H2+OH<=>H2O+H | 1.000e+08 | 1.600 | 3300.00 |
| 2OH<=>H2O+O | 1.500e+09 | 1.140 | 100.00 |
| H+O2+M<=>HO2+M | 2.300e+18 | -0.800 | 0.00 |
| C3H8/3.0/ H2O/6.5/ CO/0.75/ CO2/1.5/ O2/0.4/N2/0.4/ | | | |
| HO2+H<=>2OH | 1.500e+14 | 0.000 | 1000.00 |
| HO2+H<=>H2+O2 | 2.500e+13 | 0.000 | 690.00 |
| HO2+H<=>H2O+O | 3.000e+13 | 0.000 | 1720.00 |
| HO2+OH<=>H2O+O2 | 6.000e+13 | 0.000 | 0.00 |
| 2 H+M<=>H2+M | 1.800e+18 | -1.000 | 0.00 |
| C3H8/3.0/ H2O/6.5/ CO/0.75/ CO2/1.5/ O2/0.4/N2/0.4/ | | | |
| H+OH+M<=>H2O+M | 2.200e+22 | -2.000 | 0.00 |
| CH4/6.5/ H2O/6.5/ CO/0.75/ CO2/1.5/ O2/0.4/N2/0.4/ | | | |
| 2O+M<=>O2+M | 2.900e+17 | -1.000 | 0.00 |
| C3H8/3.0/ H2O/6.5/ CO/0.75/ CO2/1.5/ O2/0.4/N2/0.4/ | | | |
| CO+OH<=>CO2+H | 4.400e+06 | 1.500 | -740.00 |
| CO+O+M<=>CO2+M | 7.100e+13 | 0.000 | -4545.00 |
| C3H8/3.0/ H2O/6.5/ CO/0.75/ CO2/1.5/ O2/0.4/N2/0.4/ | | | |
| CO+O2<=>CO2+O | 2.500e+12 | 0.000 | 47850.00 |
| CH4+H<=>CH3+H2 | 2.200e+04 | 3.0 | 8760.00 |
| CH4+OH=>CH3+H2O | 1.600e+06 | 2.10 | 2460.00 |
| CH3+O=>CH2O+H | 7.000e+13 | 0.00 | 0.00 |
| CH3+OH=> CH2O+2H | 9.000e+14 | 0.0 | 15500.00 |
| CH3+OH=>CH2O+H2 | 8.000e+12 | 0.00 | 0.00 |
| CH3+H=>CH4 | 1.900e+36 | -7.000 | 9060.00 |
| CH2O+H=>HCO+H2 | 2.500e+13 | 0.000 | 4000.00 |
| CH2O+OH=>HCO+H2O | 3.000e+13 | 0.000 | 1200.00 |
| HCO+H=>CO+H2 | 2.000e+14 | 0.000 | 0.00 |
| HCO+OH=>CO+H2O | 1.000e+14 | 0.000 | 0.00 |
| HCO+O2=>CO+HO2 | 3.000e+12 | 0.000 | 0.00 |
| HCO(+M)=>CO+H(+M) | 7.100e+14 | 0.000 | 16820.00 |
| C3H8/3.0/ H2O/6.5/ CO/0.75/ CO2/1.5/ O2/0.4/N2/0.4/ | | | |
| 2CH3=>C2H6 | 7.470e+52 | -11.9 | 19190.00 |
| C2H6+H=>C2H5+H2 | 5.400e+02 | 3.500 | 5215.00 |
| C2H6+OH=>C2H5+H2O | 6.300e+06 | 2.000 | 645.00 |
| C2H5=>C2H4+H | 1.300e+19 | -2.000 | 41480.00 |
| C2H5+H=>2CH3 | 3.000e+13 | 0.00 | 0.00 |
| C2H5+O2=>C2H4+HO2 | 2.000e+12 | 0.000 | 5000.00 |
| C2H4+OH=>C2H3+H2O | 3.000e+13 | 0.000 | 3000.00 |
| C2H3<=>C2H2+H | 1.600e+32 | -5.5 | 46290.00 |
| C2H3+O2=>CH2O+HCO | 1.500e+12 | 0.00 | 0.00 |
| C2H3+O=>CH2CO+H | 3.000e+13 | 0.000 | 0.00 |

| | A | θ | E |
|---|---|---|---|
| CH2CO+H=>CH3+CO | 7.000e+12 | 0.000 | 3000.00 |
| CH2CO+OH=>CH2O+HCO | 1.000e+13 | 0.000 | 0.00 |
| C2H2+O=>CH2+CO | 4.100e+08 | 1.500 | 1700.00 |
| C2H2+O=>HCCO+H | 4.300e+14 | 0.00 | 12130.00 |
| C2H2+OH=>C2H+H2O | 1.000e+13 | 0.000 | 7000.00 |
| HCCO+H=>CH2+CO | 3.000e+13 | 0.000 | 0.00 |
| HCCO+O=>2CO+H | 1.000e+14 | 0.000 | 0.00 |
| CH2+O2=>CO+OH+H | 6.500e+12 | 0.000 | 1500.00 |
| CH2+O2=>CO2+H+H | 6.500e+12 | 0.00 | 1500.00 |
| CH2+H<=>CH+H2 | 4.000e+13 | 0.0 | 0.00 |
| CH+O2=>HCO+O | 3.000e+13 | 0.000 | 0.00 |
| C2H+O2=>HCCO+O | 5.000e+13 | 0.000 | 1500.00 |
| C2H+H2=>C2H2+H | 1.100e+13 | 0.00 | 2870.00 |
| CH3+H=>CH2+H2 | 1.800e+14 | 0.000 | 15070.00 |
| CH3+OH=>CH2+H2O | 1.500e+13 | 0.000 | 5000.00 |
| CH2+OH=>CH2O+H | 2.500e+13 | 0.00 | 0.00 |
| CH2+OH=>CH+H2O | 4.500e+13 | 0.00 | 3000.00 |
| CH+OH=>HCO+H | 3.000e+13 | 0.00 | 0.00 |
| C3H8+H=>N*C3H7+H2 | 1.300e+14 | 0.00 | 9710.00 |
| C3H8+OH=>N*C3H7+H2O | 6.300e+06 | 2.00 | 645.00 |
| C3H8+H=>I*C3H7+H2 | 1.000e+14 | 0.00 | 8350.00 |
| C3H8+OH=>I*C3H7+H2O | 1.200e+08 | 1.46 | -190.00 |
| N*C3H7+H=>C3H8 | 2.000e+13 | 0.000 | 0.00 |
| I*C3H7+H=>C3H8 | 2.000e+13 | 0.000 | 0.00 |
| N*C3H7=>C2H4+CH3 | 3.000e+14 | 0.000 | 33250.00 |
| N*C3H7=>C3H6+H | 1.000e+14 | 0.000 | 37340.00 |
| N*C3H7+O2=>C3H6+HO2 | 1.000e+12 | 0.00 | 5000.00 |
| I*C3H7=>C3H6+H | 2.000e+14 | 0.00 | 38730.00 |
| I*C3H7+O2=>C3H6+HO2 | 1.000e+12 | 0.00 | 2990.00 |
| C3H6+OH=>CH3CHO+CH3 | 1.000e+13 | 0.000 | 0.00 |
| CH3CHO+H=>CH3+CO+H2 | 4.000e+13 | 0.00 | 4200.00 |
| CH3CHO+OH=>CH3+CO+H2O | 1.000e+13 | 0.00 | 0.00 |

# APPENDIX - B

**The detailed chemical kinetics for the propane-air oxidation** [34] in the form of $k_l = AT^\theta \exp(-E/R_0 T)$. Units are moles, cubic centimeters, seconds, Kelvins and calories/mole

|  | A | $\theta$ | E |
|---|---|---|---|
| H+O2<=>OH+O | 2.000e+14 | 0.000 | 16820.00 |
| H2+O<=>OH+H | 5.060e+04 | 2.670 | 6290.00 |
| H2+OH<=>H2O+H | 1.000e+08 | 1.600 | 3300.00 |
| 2OH<=>H2O+O | 1.500e+09 | 1.140 | 100.00 |
| 2H+M<=>H2+M | 1.800e+18 | -1.0 | 0.0 |
| C3H8/3.0/ H2O/6.5/ CO/0.75/ CO2/1.5/ O2/0.4/N2/0.4/ | | | |
| H+OH+M<=>H2O+M | 2.200e+22 | -2.0 | 0.0 |
| C3H8/3.0/ H2O/6.5/ CO/0.75/ CO2/1.5/ O2/0.4/N2/0.4/ | | | |
| O+O+M<=>O2+M | 2.900e+17 | -1.0 | 0.0 |
| C3H8/3.0/ H2O/6.5/ CO/0.75/ CO2/1.5/ O2/0.4/N2/0.4/ | | | |
| H+O2+M<=>HO2+M | 2.300e+18 | -0.800 | 0.00 |
| C3H8/3.0/ H2O/6.5/ CO/0.75/ CO2/1.5/ O2/0.4/N2/0.4/ | | | |
| HO2+H<=>2OH | 1.500e+14 | 0.000 | 1000.00 |
| HO2+H<=>H2+O2 | 2.500e+13 | 0.000 | 690.00 |
| HO2+H<=>H2O+O | 3.000e+13 | 0.000 | 1720.00 |
| HO2+O<=>OH+O2 | 1.800e+13 | 0.000 | -400.00 |
| HO2+OH<=>H2O+O2 | 6.000e+13 | 0.000 | 0.00 |
| HO2+HO2=>H2O2+O2 | 2.500e+11 | 0.00 | -1240.00 |
| OH+OH+M<=>H2O2+M | 3.256e+22 | -2.00 | 0.00 |
| C3H8/3.0/ H2O/6.5/ CO/0.75/ CO2/1.5/ O2/0.4/N2/0.4/ | | | |
| H2O2+H<=>H2+HO2 | 1.700E+12 | 0.00 | 3750.00 |
| H2O2+H<=>H2O+OH | 1.000E+13 | 0.0 | 3590.00 |
| H2O2+O<=>OH+HO2 | 2.800E+13 | 0.0 | 6410.00 |
| H2O2+OH<=>H2O+HO2 | 5.400E+12 | 0.0 | 1000.00 |
| CO+OH<=>CO2+H | 4.400e+06 | 1.500 | -740.00 |
| CO+HO2<=>CO2+OH | 1.500e+14 | 0.0 | 23610.00 |
| CO+O+M<=>CO2+M | 7.100e+13 | 0.000 | -4545.00 |
| C3H8/3.0/ H2O/6.5/ CO/0.75/ CO2/1.5/ O2/0.4/N2/0.4/ | | | |
| CO+O2<=>CO2+O | 2.500e+12 | 0.000 | 47850.00 |
| CH+O<=>CO+H | 4.000e+13 | 0.00 | 0.00 |
| CH+O2<=>HCO+O | 3.000e+13 | 0.00 | 0.00 |
| CH+CO2=>HCO+CO | 3.400e+12 | 0.00 | 690.00 |
| HCO+H<=>CO+H2 | 2.000e+14 | 0.00 | 0.00 |
| HCO+O<=>CO+OH | 3.000e+13 | 0.00 | 0.00 |
| HCO+O<=>CO2+H | 3.000e+13 | 0.00 | 0.00 |
| HCO+OH<=>CO+H2O | 1.000e+14 | 0.00 | 0.00 |
| HCO+O2<=>CO+HO2 | 3.000e+12 | 0.00 | 0.00 |
| HCO+M<=>CO+H+M | 7.100e+14 | 0.00 | 16820.00 |
| C3H8/3.0/ H2O/6.5/ CO/0.75/ CO2/1.5/ O2/0.4/N2/0.4/ | | | |
| CH2+H<=>CH+H2 | 4.000e+13 | 0.00 | 0.0 |
| CH2+O=>CO+2H | 8.000e+13 | 0.00 | 0.0 |
| CH2+O2=>CO+OH+H | 6.500e+12 | 0.00 | 1500.0 |
| CH2+O2=>CO2+2H | 6.500e+12 | 0.00 | 1500.0 |

|  | $A$ | $\theta$ | $E$ |
|---|---|---|---|
| CH2O+H<=>HCO+H2 | 2.500e+13 | 0.0 | 4000.0 |
| CH2O+O<=>HCO+OH | 3.500e+13 | 0.0 | 3490.0 |
| CH2O+OH<=>HCO+H2O | 3.000e+13 | 0.0 | 1200.0 |
| CH2O+HO2<=>HCO+H2O2 | 1.000e+12 | 0.0 | 8000.0 |
| CH2O+CH3<=>HCO+CH4 | 1.000e+11 | 0.0 | 6100.0 |
| CH2O+M<=>HCO+H+M | 1.400e+17 | 0.0 | 76550.0 |
| CH3+H<=>CH2+H2 | 1.800e+14 | 0.0 | 15070.0 |
| CH3+O=>CH2O+H | 7.000e+13 | 0.00 | 0.00 |
| CH3+OH=> CH2O+2H | 9.000e+14 | 0.0 | 15500.00 |
| CH3+OH=>CH2O+H2 | 8.000e+12 | 0.00 | 0.00 |
| CH3+O2=>CH2O+H+O | 1.500e+13 | 0.0 | 28710.0 |
| CH3+CH3<=>C2H6 | 7.470e+52 | -11.9 | 19190.0 |
| CH3+M<=>CH2+H+M | 1.000e+16 | 0.0 | 90910.0 |
| CH3+CH3=>C2H4+H2 | 1.000e+16 | 0.0 | 32060.0 |
| CH3+CH2=>C2H4+H | 4.000e+13 | 0.0 | 0.0 |
| CH4+H<=>H2+CH3 | 2.200e+04 | 3.0 | 8760.0 |
| CH4+O<=>OH+CH3 | 1.200e+07 | 2.1 | 7630.0 |
| CH4+OH<=>H2O+CH3 | 1.600e+6 | 2.1 | 2460.0 |
| CH4+HO2<=>H2O2+CH3 | 4.000e+12 | 0.0 | 19425.0 |
| CH4<=>CH3+H | 3.200e+34 | -6.0 | 109450.0 |
| CH4+CH2<=>2CH3 | 1.300e+13 | 0.0 | 9545.0 |
| CH4+CH<=>C2H4+H | 3.000e+13 | 0.0 | -400.0 |
| C2H+O<=>CO+CH | 1.000e+13 | 0.0 | 0.0 |
| C2H+H2<=>C2H2+H | 1.100e+13 | 0.0 | 2870.0 |
| C2H+O2<=>HCCO+O | 5.000e+13 | 0.0 | 1570.0 |
| HCCO+H<=>CH2+CO | 3.000e+13 | 0.0 | 0.0 |
| HCCO+O=>2CO+H | 1.000e+14 | 0.0 | 0.0 |
| C2H2+O<=>CH2+CO | 4.100E+8 | 1.5 | 1700.0 |
| C2H2+O<=>HCCO+H | 4.300e+14 | 0.0 | 12130.0 |
| C2H2+OH<=>H2O+C2H | 1.000e+13 | 0.0 | 7000.0 |
| C2H2+M<=>C2H+H+M | 3.600e+16 | 0.0 | 106700.0 |
| CH2CO+H<=>CH3+CO | 7.000e+12 | 0.0 | 3000.0 |
| CH2CO+O<=>2HCO | 1.800e+12 | 0.0 | 1340.0 |
| CH2CO+OH<=>CH2O+HCO | 1.000e+13 | 0.0 | 0.0 |
| CH2CO+M<=>CH2+CO+M | 1.000e+16 | 0.0 | 59330.0 |
| C3H8/3.0/ H2O/6.5/ CO/0.75/ CO2/1.5/ O2/0.4/N2/0.4/ | | | |
| C2H3+H<=>H2+C2H2 | 2.000e+13 | 0.0 | 0.0 |
| C2H3+O<=>CH2CO+H | 3.000e+13 | 0.0 | 0.0 |
| C2H3+O2=>CH2O+HCO | 1.500e+12 | 0.0 | 0.0 |
| C2H3<=>C2H2+H | 1.600e+32 | -5.5 | 46290.00 |
| CH3CO+H<=>CH2CO+H2 | 2.000e+13 | 0.0 | 0.0 |
| CH3CO+O<=>CH3+CO2 | 2.000e+13 | 0.0 | 0.0 |
| CH3CO+CH3<=>C2H6+CO | 5.000e+13 | 0.0 | 0.0 |

|  | $A$ | $\theta$ | $E$ |
|---|---|---|---|
| C2H4+H<=>C2H3+H2 | 1.500e+14 | 0.0 | 10215.0 |
| C2H4+O=>CH3CO+H | 1.600e+09 | 1.2 | 740.0 |
| C2H4+OH<=>C2H3+H2O | 3.000e+13 | 0.0 | 3000.0 |
| C2H4+CH3<=>C2H3+CH4 | 4.200e+11 | 0.0 | 11120.0 |
| C2H4+M<=>C2H2+H2+M | 2.500e+17 | 0.0 | 76500.0 |
| CH3CHO+H<=>CH3CO+H2 | 4.000e+13 | 0.0 | 4210.0 |
| CH3CHO+O<=>CH3CO+OH | 5.000e+12 | 0.0 | 1790.0 |
| CH3CHO+OH<=>CH3CO+H2O | 8.000e+12 | 0.0 | 0.0 |
| CH3CHO+HO2<=>CH3CO+H2O2 | 1.700e+12 | 0.0 | 10720.0 |
| CH3CHO+CH2<=>CH3CO+CH3 | 2.500e+12 | 0.0 | 3800.0 |
| CH3CHO+CH3<=>CH3CO+CH4 | 8.500e+10 | 0.0 | 6000.0 |
| CH3CHO<=>CH3+HCO | 2.000e+15 | 0.0 | 79190.0 |
| C2H5+H<=>2CH3 | 3.000e+13 | 0.0 | 0.0 |
| C2H5+O<=>CH3CHO+H | 5.000e+13 | 0.0 | 0.0 |
| C2H5+O2<=>HO2+C2H4 | 2.000e+12 | 0.0 | 5000.0 |
| C2H5+CH3<=>C3H8 | 7.000e+12 | 0.0 | 0.0 |
| C2H5+C2H5<=>C2H4+C2H6 | 1.400e+12 | 0.0 | 0.0 |
| C2H5<=>C2H4+H | 1.300e+19 | -2.0 | 41480.0 |
| C2H6+H<=>H2+C2H5 | 5.400e+02 | 3.5 | 5215.0 |
| C2H6+O<=>OH+C2H5 | 3.000e+07 | 2.0 | 5120.0 |
| C2H6+OH<=>H2O+C2H5 | 6.300e+06 | 2.0 | 645.0 |
| C2H6+HO2<=>H2O2+C2H5 | 6.000e+12 | 0.0 | 19420.0 |
| C2H6+CH3<=>C2H5+CH4 | 5.500e-01 | 4.0 | 8300.0 |
| C2H6+CH2<=>CH3+C2H5 | 2.200e+13 | 0.0 | 8680.0 |
| C2H6+CH<=>H+C3H6 | 1.100E+14 | 0.0 | -260.0 |
| C3H8+H<=>N*C3H7+H2 | 1.300e+14 | 0.00 | 9710.00 |
| C3H8+H<=>I*C3H7+H2 | 1.000e+14 | 0.00 | 8350.00 |
| C3H8+O<=>N*C3H7+OH | 3.000e+13 | 0.0 | 5765.00 |
| C3H8+O<=>I*C3H7+OH | 2.600e+13 | 0.0 | 4470.00 |
| C3H8+OH<=>N*C3H7+H2O | 6.300e+06 | 2.00 | 645.00 |
| C3H8+OH=>I*C3H7+H2O | 1.200e+08 | 1.46 | -190.00 |
| C3H8+HO2<=>N*C3H7+H2O2 | 6.000e+12 | 0.0 | 19420.0 |
| C3H8+HO2<=>I*C3H7+H2O2 | 2.000e+12 | 0.0 | 17000.0 |
| C3H8+CH3<=>N*C3H7+CH4 | 7.500e+12 | 0.0 | 14950.0 |
| C3H8+CH3<=>I*C3H7+CH4 | 4.300e+12 | 0.0 | 13280.0 |

# APPENDIX - C

**The NOx chemistry of GRI -2.11** in the form of $k_l = AT^{\theta} \exp(-E/R_o T)$ Units are mole, cubic centimeters, seconds, Kelvins and calories/mole.

| Reaction | A | $\theta$ | E |
|---|---|---|---|
| N+NO<=>N2+O | 3.500E+13 | .000 | 330.00 |
| N+O2<=>NO+O | 2.650E+12 | .000 | 6400.00 |
| N+OH<=>NO+H | 7.333E+13 | .000 | 1120.00 |
| N2O+O<=>N2+O2 | 1.400E+12 | .000 | 10810.00 |
| N2O+O<=>2NO | 2.900E+13 | .000 | 23150.00 |
| N2O+H<=>N2+OH | 4.400E+14 | .000 | 18880.00 |
| N2O+OH<=>N2+HO2 | 2.000E+12 | .000 | 21060.00 |
| N2O(+M)<=>N2+O(+M) | 1.300E+11 | .000 | 59620.00 |
| H2/2.00/ H2O/6.00/ CH4/2.00/ CO/1.50/ CO2/2.00/ C2H6/3.00/ | | | |
| HO2+NO<=>NO2+OH | 2.110E+12 | .000 | -480.00 |
| NO+O+M<=>NO2+M | 1.060E+20 | -1.410 | .00 |
| H2/2.00/ H2O/6.00/ CH4/2.00/ CO/1.50/ CO2/2.00/ C2H6/3.00/ | | | |
| NO2+O<=>NO+O2 | 3.900E+12 | .000 | -240.00 |
| NO2+H<=>NO+OH | 1.320E+14 | .000 | 360.00 |
| NH+O<=>NO+H | 5.000E+13 | .000 | .00 |
| NH+H<=>N+H2 | 3.200E+13 | .000 | 330.00 |
| NH+OH<=>HNO+H | 2.000E+13 | .000 | .00 |
| NH+OH<=>N+H2O | 2.000E+09 | 1.200 | .00 |
| NH+O2<=>HNO+O | 4.610E+05 | 2.000 | 6500.00 |
| NH+O2<=>NO+OH | 1.280E+06 | 1.500 | 100.00 |
| NH+N<=>N2+H | 1.500E+13 | .000 | .00 |
| NH+H2O<=>HNO+H2 | 2.000E+13 | .000 | 13850.00 |
| NH+NO<=>N2+OH | 2.160E+13 | -.230 | .00 |
| NH+NO<=>N2O+H | 4.160E+14 | -.450 | .00 |
| NH2+O<=>OH+NH | 7.000E+12 | .000 | .00 |
| NH2+O<=>H+HNO | 4.600E+13 | .000 | .00 |
| NH2+H<=>NH+H2 | 4.000E+13 | .000 | 3650.00 |
| NH2+OH<=>NH+H2O | 9.000E+07 | 1.500 | -460.00 |
| NNH<=>N2+H | 3.300E+08 | .000 | .00 |
| NNH+M<=>N2+H+M | 1.300E+14 | -.110 | 4980.00 |
| H2/2.00/ H2O/6.00/ CH4/2.00/ CO/1.50/ CO2/2.00/ C2H6/3.00/ | | | |
| NNH+O2<=>HO2+N2 | 5.000E+12 | .000 | .00 |
| NNH+O<=>OH+N2 | 2.500E+13 | .000 | .00 |
| NNH+O<=>NH+NO | 7.000E+13 | .000 | .00 |
| NNH+H<=>H2+N2 | 5.000E+13 | .000 | .00 |
| NNH+OH<=>H2O+N2 | 2.000E+13 | .000 | .00 |
| NNH+CH3<=>CH4+N2 | 2.500E+13 | .000 | .00 |
| H+NO+M<=>HNO+M | 8.950E+19 | -1.320 | 740.00 |
| H2/2.00/ H2O/6.00/ CH4/2.00/ CO/1.50/ CO2/2.00/ C2H6/3.00/ | | | |
| HNO+O<=>NO+OH | 2.500E+13 | .000 | .00 |
| HNO+H<=>H2+NO | 4.500E+11 | .720 | 660.00 |
| HNO+OH<=>NO+H2O | 1.300E+07 | 1.900 | -950.00 |
| HNO+O2<=>HO2+NO | 1.000E+13 | .000 | 13000.00 |

|  | $A$ | $\theta$ | $E$ |
|---|---|---|---|
| CN+O<=>CO+N | 7.700E+13 | .000 | .00 |
| CN+OH<=>NCO+H | 4.000E+13 | .000 | .00 |
| CN+H2O<=>HCN+OH | 8.000E+12 | .000 | 7460.00 |
| CN+O2<=>NCO+O | 6.140E+12 | .000 | -440.00 |
| CN+H2<=>HCN+H | 2.100E+13 | .000 | 4710.00 |
| NCO+O<=>NO+CO | 2.350E+13 | .000 | .00 |
| NCO+H<=>NH+CO | 5.400E+13 | .000 | .00 |
| NCO+OH<=>NO+H+CO | 2.500E+12 | .000 | .00 |
| NCO+N<=>N2+CO | 2.000E+13 | .000 | .00 |
| NCO+O2<=>NO+CO2 | 2.000E+12 | .000 | 20000.00 |
| NCO+M<=>N+CO+M | 8.800E+16 | -.500 | 48000.00 |
| H2/2.00/ H2O/6.00/ CH4/2.00/ CO/1.50/ CO2/2.00/ C2H6/3.00/ | | | |
| NCO+NO<=>N2O+CO | 2.850E+17 | -1.520 | 740.00 |
| NCO+NO<=>N2+CO2 | 5.700E+18 | -2.000 | 800.00 |
| HCN+M<=>H+CN+M | 1.040E+29 | -3.300 | 126600.00 |
| H2/2.00/ H2O/6.00/ CH4/2.00/ CO/1.50/ CO2/2.00/ C2H6/3.00/ | | | |
| HCN+O<=>NCO+H | 1.107E+04 | 2.640 | 4980.00 |
| HCN+O<=>NH+CO | 2.767E+03 | 2.640 | 4980.00 |
| HCN+O<=>CN+OH | 2.134E+09 | 1.580 | 26600.00 |
| HCN+OH<=>HNCO+H | 4.400E+03 | 2.260 | 6400.00 |
| HCN+OH<=>NH2+CO | 1.600E+02 | 2.560 | 9000.00 |
| H+HCN+M<=>H2CN+M | 1.400E+26 | -3.400 | 1900.00 |
| H2/2.00/ H2O/6.00/ CH4/2.00/ CO/1.50/ CO2/2.00/ C2H6/3.00/ | | | |
| H2CN+N<=>N2+CH2 | 6.000E+13 | .000 | 400.00 |
| CH+N2<=>HCN+N | 2.857E+08 | 1.100 | 20400.00 |
| CH2+N2<=>HCN+NH | 1.000E+13 | .000 | 74000.00 |
| CH+NO<=>HCN+O | 5.000E+13 | .000 | .00 |
| CH+NO<=>H+NCO | 2.000E+13 | .000 | .00 |
| CH+NO<=>N+HCO | 3.000E+13 | .000 | .00 |
| CH2+NO<=>H+HNCO | 3.100E+17 | -1.380 | 1270.00 |
| CH2+NO<=>OH+HCN | 2.900E+14 | -.690 | 760.00 |
| CH2+NO<=>H+HCNO | 3.800E+13 | -.360 | 580.00 |
| CH3+NO<=>HCN+H2O | 9.600E+13 | .000 | 28800.00 |
| CH3+NO<=>H2CN+OH | 1.000E+12 | .000 | 21750.00 |
| HNCO+O<=>NH+CO2 | 9.800E+07 | 1.410 | 8500.00 |
| HNCO+O<=>HNO+CO | 1.500E+08 | 1.570 | 44000.00 |
| HNCO+O<=>NCO+OH | 2.200E+06 | 2.110 | 11400.00 |
| HNCO+H<=>NH2+CO | 2.250E+07 | 1.700 | 3800.00 |
| HNCO+H<=>H2+NCO | 1.050E+05 | 2.500 | 13300.00 |
| HNCO+OH<=>NCO+H2O | 4.650E+12 | .000 | 6850.00 |
| HNCO+OH<=>NH2+CO2 | 1.550E+12 | .000 | 6850.00 |
| HNCO+M<=>NH+CO+M | 1.180E+16 | .000 | 84720.00 |
| H2/2.00/ H2O/6.00/ CH4/2.00/ CO/1.50/ CO2/2.00/ C2H6/3.00/ | | | |

| | $A$ | $\theta$ | $E$ |
|---|---|---|---|
| HCNO+H<=>H+HNCO | 2.100E+15 | -.690 | 2850.00 |
| HCNO+H<=>OH+HCN | 2.700E+11 | .180 | 2120.00 |
| HCNO+H<=>NH2+CO | 1.700E+14 | -.750 | 2890.00 |
| HCCO+NO<=>HCNO+CO | 2.350E+13 | .000 | .00 |
| CH3+N<=>H2CN+H | 6.100E+14 | -.310 | 290.00 |
| CH3+N<=>HCN+H2 | 3.700E+12 | .150 | -90.00 |
| NH3+H<=>NH2+H2 | 5.400E+05 | 2.400 | 9915.00 |
| NH3+OH<=>NH2+H2O | 5.000E+07 | 1.600 | 955.00 |
| NH3+O<=>NH2+OH | 9.400E+06 | 1.940 | 6460.00 |